

**Copyright**

**by**

**Zhong Shi**

**2004**

**The Dissertation Committee for Zhong Shi  
Certifies that this is the approved version of the following dissertation:**

**Optical-Controlled True-Time Delay Devices and Their  
Application in Phased Array Antenna System**

**Committee:**

---

Ray T. Chen, Supervisor

---

Jack Lee

---

Dennis G. Deppe

---

Hao Ling

---

Leonard F. Register

---

Paul Ho

**Optical-Controlled True-Time Delay Devices and Their  
Application in Phased Array Antenna System**

by

**Zhong Shi, B.S., M.S.**

**Dissertation**

Presented to the Faculty of the Graduate School of  
the University of Texas at Austin  
in Partial Fulfillment  
of the Requirements  
for the Degree of

**Doctor of Philosophy**

The University of Texas at Austin

December 2004

**To My Beautiful Wife: Kaiyi Li**

## **Acknowledgements**

I would like to take this opportunity to thank Dr. Ray Chen for his continuous support during these four years. I want to thank all the group members for the helps they gave to me during this period of time, especially to Xiaonan Chen with whom I enjoyed a busy and pleasant summer. I should also thank all my committee members: Dr. Ray Chen, Dr. Jack Lee, Dr. Dennis Deppe, Dr. Hao Ling, Dr. Leonard Register, and Dr. Paul Ho, for their willing to serve on this committee. I would like to express my special and deepest gratitude to my beautiful wife: Kaiyi, for her love and patience during these years. Finally, I should thank my parents-in-law, and my parents. Without their encouragement, support, and patience, I will not be able to finish this work and get the degree.

Zhong Shi

Austin, TX

# **Optical-Controlled True-Time Delay Devices and Their Application in Phased Array Antenna System**

Publication No. \_\_\_\_\_

Zhong Shi, Ph.D.

The University of Texas at Austin, 2004

Supervisor: Ray T. Chen

Military and civilian wireless communication systems require compact phased array antenna systems with high performance. Conventional phase-shifter based techniques suffer from beam squint effect which causes undesirable changing of beam steering angle when the microwave frequency changes in phased array antenna system. Optical true-time delay techniques open the possibility of ultra-wide bandwidth antenna systems, while at the same time meeting the stringent weight and size requirements. Continuously tunable true-time delay techniques can provide continuous beam-steering ability without mechanical movement for the phased array antenna systems. With advanced optoelectronic techniques, fast wavelength tuning speed ( $\sim$ ns) is possible. This may provide viable solutions to the high-speed phased array antenna systems. This dissertation describes holographic-gratings based optical continuous-tunable true-time delay devices and their application in a X-band phased array antenna system. The design,

development and measurements of the true-time delay devices and the X-band phased array antenna system are explained in this dissertation.

# Table of Contents

List of Figures .....	xi
List of Tables .....	xv
Chapter 1 – Outline .....	1
Chapter 2 –Introduction .....	3
2.1 Overview.....	3
2.2 Continuous-tunable true-time delay formation.....	5
2.2.1 Dispersive fiber based true-time delay formation.....	5
2.2.2 Photonic crystal fiber based true-time delay formation.....	6
2.2.3 Chirped fiber gratings based true-time delay formation .....	8
2.3 Summary .....	8
2.4 Reference .....	9
Chapter 3 – Proposed true-time delay formation approach and phased array antenna PAA system.....	13
3.1 Proposed true-time delay formation approach and phased array antenna system .....	13
3.2 Wavelength conversion in semiconductor optical amplifier .....	15
3.3 General issues of phased array antenna system .....	17
3.2.1 Grating lobes.....	17
3.2.2 Beam width and bandwidth .....	19
3.4 Figure-of-merits of microwave photonics system .....	20
3.5 Summery .....	23
3.6 Reference .....	24
Chapter 4 – Volume-holographic gratings based true-time delay devices: design, fabrication and characterization .....	25
4.1 Design .....	25

4.2	Fabrication .....	35
4.3	Experimental results.....	42
4.4	Summary .....	46
4.5	Reference .....	46
Chapter 5 – Semiconductor optical amplifier: simulation and measurement .....		48
5.1	Introduction.....	48
5.2	Static model for SOA.....	55
5.3	Simulation results.....	58
5.4	Experimental results.....	62
5.4	Summary .....	65
5.5	Reference .....	65
Chapter 6 – Microwave photonics system analysis with wavelength conversion .....		68
6.1	Introduction.....	68
6.2	Analytic solutions of rate equation .....	70
6.3	Experimental setup for wavelength conversion.....	74
6.4	Frequency response and link gain analysis.....	75
6.5	Distortion analysis .....	77
6.6	Noise figure analysis.....	85
6.7	Summary .....	89
6.8	Reference .....	90
Chapter 7– Developed phased array antenna system.....		92
7.1	1D X-band Phased array antenna system.....	92
7.2	2D X-band Phased array antenna system.....	102
7.2	Summary .....	104
Chapter 8– Summary .....		105
References .....		106

Vita .....	116
------------	-----

## List of Figures

Fig. 2.1	Dispersive fiber prism for true-time delay formation.....	6
Fig. 3.1	Schematic illustration of time delay formation.....	14
Fig. 3.2	2-dimension phased array antenna system structure.....	15
Fig. 3.3(a)	Wavelength conversion structure.....	16
Fig. 3.3(b)	Principle of wavelength conversion.....	17
Fig. 3.4	Illustration of time delay transfer by wavelength conversion.....	17
Fig. 3.5	Plot of radiation pattern for a 4x4 element phased array antenna.....	18
Fig. 3.6	Plot of radiation pattern for a 4x4 element phased array antenna ....	19
Fig. 3.7	Distribution of the fundamental and distortion frequencies .....	22
Fig. 3.8	Illustration of spurious free dynamic range .....	23
Fig. 4.1(a)	Configuration for non surface normal incident case.....	26
Fig. 4.1(b)	Configuration for surface normal incident case.....	26
Fig. 4.2	Dispersion ability vs. diffraction angle.....	28
Fig. 4.3	3-dB bandwidth vs. diffraction angle.....	30
Fig. 4.4	Time delay generation within a 3-dB optical bandwidth.....	31
Fig. 4.5	Peak diffraction efficiency vs. index modulation depth .....	32
Fig. 4.6	Illustration of polarization dependent phenomenon .....	33
Fig. 4.7	Interface reflection between air and polymer .....	33
Fig. 4.8	Diffraction efficiency vs. diffraction angle for P-polarization .....	34
Fig. 4.9	Schematic illustration of time delay formation.....	34
Fig. 4.10	Time delay vs. wavelength tuning and thickness difference .....	35
Fig. 4.11	Structure of the holographic grating laminated on a glass waveguide .....	36
Fig. 4.12	Schematic diagram of hologram recording setup .....	38
Fig. 4.13	Holographic grating recording structure with prism.....	40

Fig. 4.14	Schematic diagram for holographic grating recording with right angle prism.....	40
Fig. 4.15	Schematic diagram for recording parameters calculation.....	41
Fig. 4.16	Schematic diagram for recording parameters calculation.....	42
Fig. 4.17	Transmissivity for different incident angle.....	42
Fig. 4.18	Holographic recording optimization results.....	43
Fig. 4.19	Insertion loss measurement results .....	44
Fig. 4.20	Illustration of dispersion measurement.....	44
Fig. 4.21	Dispersion measurement results .....	45
Fig. 4.22	Time delay measurement results.....	45
Fig. 5.1	Illustration of difference between F-P SOA and TW SOA .....	51
Fig. 5.2	Schematic diagram of SOA .....	52
Fig. 5.3	Schematic diagram of amplification process in SOA .....	52
Fig. 5.4	Carrier distribution along the longitudinal direction of SOA cavity .....	59
Fig. 5.5	Gain in each small section along SOA cavity.....	60
Fig. 5.6	Total gain along SOA cavity.....	61
Fig. 5.7	Gain vs. Input optical power .....	62
Fig. 5.8	ASE spectrum from SOA.....	63
Fig. 5.9	Gain vs. Injection current.....	63
Fig. 5.10(a)	Gain vs. optical input power .....	64
Fig. 5.10(b)	Gain vs. optical input power .....	64
Fig. 6.1(a)	Cross-gain-modulation based wavelength conversion structure.....	70
Fig. 6.1(b)	Cross-phase-modulation based wavelength conversion structure ....	70
Fig. 6.2	Schematic diagram for wavelength conversion .....	74
Fig. 6.3	Experiment setup for wavelength conversion.....	74
Fig. 6.4	Frequency response measurement .....	76

Fig. 6.5	Transfer function of wavelength conversion .....	76
Fig. 6.6	Modulator operating point optimization .....	78
Fig. 6.7	2HD simulation and measurement results .....	81
Fig. 6.8(a)	2 <sup>nd</sup> harmonic distortion free dynamic range measurements.....	81
Fig. 6.8(b)	2 <sup>nd</sup> harmonic distortion free dynamic range measurements.....	82
Fig. 6.9(a)	2 <sup>nd</sup> harmonic distortion FDR vs. input average optical power.....	82
Fig. 6.9(b)	2 <sup>nd</sup> harmonic distortion FDR vs. input average optical power.....	83
Fig. 6.10(a)	Response measurement of optical modulator for the fundamental frequency.....	83
Fig. 6.10(b)	Response measurement of optical modulator for the second harmonic frequency.....	84
Fig. 6.10(c)	Power difference between the fundamental frequency and the corresponding second harmonic frequency .....	84
Fig. 6.11	NF vs. bias current .....	88
Fig. 6.12	NF vs. input pump power .....	89
Fig. 7.1	Schematic of the system experiment setup .....	93
Fig. 7.2	Linear 4-element phased array antenna system photo .....	94
Fig. 7.3	Picture of patch antenna array and the receiving horn.....	95
Fig. 7.4(a)	Measured reflection coefficient $S_{11}$ of four antenna elements .....	95
Fig. 7.4(b)	Measured SWR of four antenna elements .....	96
Fig. 7.5(a)	Structure of the receiving standard gain horn.....	96
Fig. 7.5(b)	Measured gain of standard gain horn.....	97
Fig. 7.6	Insertion loss measurement.....	99
Fig. 7.7	Measured $S_{12}$ after photo detectors .....	99
Fig. 7.8	Measured phase difference vs. frequency.....	100
Fig. 7.9(a)	Measured 4-element linear array radiation pattern .....	101
Fig. 7.9(b)	Measured 4-element linear array radiation pattern .....	101

Fig. 7.10	Time delay measurement before and after wavelength .....	102
Fig. 7.11(a)	4x4 2D system radiation pattern in the horizontal direction .....	103
Fig. 7.11(b)	4x4 2D system radiation pattern in the vertical direction .....	103
Fig. 7.12	Photo of the developed 2D 4x4 phased array antenna system.....	105

## List of Tables

Table 5.1	Comparison among different types of optical amplifiers .....	50
Table 5.2	Parameters used for the simulation .....	58
Table 7.1	Size parameters for the receiving gain horn .....	97

# Chapter 1

## Outline

In the past few years, considerable R&D efforts have been made in the microwave optical devices and systems. The main reason that the optical technology can potentially replace the microwave technology in some applications is that cost/performance gap between the optical technology and the microwave technology is not as large as before. The microwave phased array antennas have very important applications in military and civilian radars and communications technology. The conventional phase-shifter based microwave phase array antennas suffer from the so-called beam squint effect. To solve this problem, many researchers have proposed and developed various optical true-time delay devices to replace the position of the phase-shifters in the phased array antennas. Most of the proposed optical true-time delay schemes can only provide discrete true-time delay. This work is aimed to investigate the holographic-gratings based continuously tunable true-time delay devices and their application in an X-band phased-array antenna system.

This dissertation is organized as follows: Chapter 2 gives an overview of the current state-of-art optical continuous-tunable true-time delay techniques. Chapter 3 is an introduction of the proposed holographic-gratings based true-time delay devices and the system structure of an X-band phased array antenna. Some general issues concerning a phased array antenna are also discussed in this chapter. Chapter 4 presents the holographic-gratings based continuously tunable true-time delay devices, including design, fabrication and measurements. Chapter 5 contains theoretical model for

characterizing static performance of semiconductor optical amplifiers (SOA). SOA is used for wavelength conversion purpose in the phased array antenna system. The corresponding measurement results of semiconductor optical amplifiers are also presented. Chapter 6 introduces analog performance of wavelength conversion using cross-gain-modulation (XGM) in semiconductor optical amplifiers. We particularly focus on the analysis of frequency response, link gain optimization, distortion and noise figure performance. Chapter 7 introduces the developed X-band linear 4-element phased array antenna system and 2-dimension 4x4 phased array antenna system. Chapter 8 is a short summary for this research work.

## **Chapter 2**

### **Introduction**

#### 2.1 Overview

The applications of optical true-time delay techniques provide unique performance to the phased array antennas. The optical devices that can be used in phased array antenna systems includes: lasers, modulators, fibers, waveguides, amplifiers, switches, and photo detectors. With optical technology, the microwave frequency is modulated to the optical carrier frequency and then transmitted over the standard single-mode fiber. The optical signal is converted back to the electrical signal at the receiver end. The converted electrical signal is radiated coherently to the outside through the antenna heads. The optical true-time delay technique provides time delay among optical signals. After optical-to-electrical conversion, the time delay among the optical signals can be converted to the phase difference among the electrical signals. The optical true-time delay techniques intend to replace the traditional microwave phase-shifters in phased array antennas and they offer some unique advantages over the microwave phase-shifter techniques. The first advantage is that the beam squint effect is greatly reduced. The beam steering angle will change in the conventional phase shifter based phased array antennas when the microwave frequency is changed, which is undesirable in the real application. With optical true-time delay formation, the beam steering angle is only determined by the time delay between the antenna elements, having nothing to do with the microwave frequency. Of course this is only true under the assumption that the microwave frequency (Several GHz to tens of GHz) is much lower than the optical

frequency (~hundreds THz). So the beam steering direction is not sensitive to the microwave frequency in optical true-time-delay based phased array antennas. The second advantage is that electromagnetic interference (EMI) from the outside or inside the phased array system is reduced greatly. It can avoid potential outside electromagnetic pulse attacks and improve the security performance of the systems. Of course EMI in the radiating ends for the optical technology based phased array antennas still exist. However, they can be reduced to a negligible level with appropriate design of distribution structure of antenna elements.

Since the first demonstration of an optical true-time delay steered phased array antenna [1], many approaches for implementing optical true-time delay have been proposed and demonstrated. These research efforts can be broadly divided into two directions: discrete time delay based and continuous time delay based, and most of the proposed and developed true time delay formation structures are discrete time delay based. Discrete time delay based phased array antennas can steer beam at certain pre-determined discrete angles. So they cannot provide a full coverage within a certain beam steering angle scope. The continuous time delay based phased array antennas can steer beam continuously within a certain angle scope and no mechanical movement is involved in the beam steering process, which is a great improvement compared with discrete time delay based approaches. As this research work is particular interested in investigating the continuous true-time delay technology, we will only give an overview of research and development status of continuous tunable optical true-time delay schemes. The discrete true-time delay formation schemes can be found from the following listed references, bulk optics true-time delay lines [2-6], optical non-dispersive fiber true-time delay lines

[7], wavelength-division-multiplexer [8-13], holographic-gratings based schemes [14-15], wavelength-selective waveguide approach [16], acoustic-optic based approaches [17-20]. In the following sections, we will introduce continuous true-time delay formation schemes that were proposed and developed in the recent years.

## 2.2 Continuous-tunable true-time delay formation schemes

### 2.2.1 Dispersive fiber based true-time delay formation

The optical dispersion-based true-time delay formation scheme is based on the wavelength-dependent group velocity in the fibers. The dispersion in the fibers attributes to both the material dispersion and the waveguide dispersion. The material dispersion cannot be tailored much compared with the waveguide dispersion of the fibers. Intrinsically all the fiber-based schemes have to deal with how to tailor the index of the core and the cladding of the fibers, thus tailoring the waveguide dispersion of fibers. The dispersive-fiber based approach can provide continuously tunable true-time delay and it is made feasible by the widely tunable laser and the dispersive nature of the fibers. Soref first proposed to use the standard SMF dispersion (18ps/nm/Km) for continuous true-time delay formation for microwave phased-array antennas [21]. Johns et al. then reported the first experimental implementation of this idea with high dispersion fiber (-98ps/nm/Km) [22]. Esman et al. then demonstrated an optical true-time delay based phased-array antenna system which utilized a tunable laser with a 50-nm tuning range and the dispersive fibers in a standard externally modulated link configuration [23]. The true-time delay was formed by splitting the modulated laser source into a fiber-optic prism comprising several optical fiber links, each having the same nominal group delay, but

with slightly different net dispersion, as shown in Figure 2.1. The fiber-optic prism was made by connecting varying amounts of high-dispersion and non-dispersion fiber. Therefore, a change in the optical wavelength will result in different amounts of total delay change in each fiber link. At the center wavelength  $\lambda_0$ , all the time delays were matched by trimming the fibers, and the main antenna beam will be directed broadside. At longer wavelength than  $\lambda_0$ , each of the prism fibers adds (subtracts) a time delay proportional to its dispersion, resulting in different time delay formation and element phasing formation.

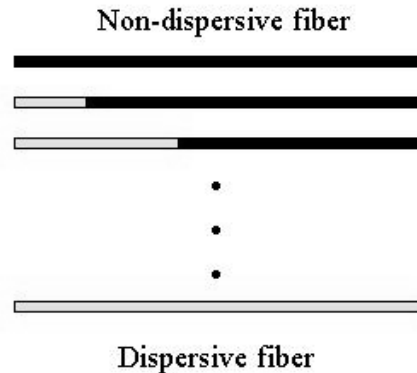


Figure 2.1 Fiber prism for true-time delay formation

The drawback of this fiber-optic prism approach based on dispersive fibers is that the length of fiber is usually more than one hundred meters or even up to one kilometer depending on the dispersion ability of the fibers.

### 2.2.2 Photonics crystal fiber based true-time delay formation

The dispersion of the fibers used for true-time delay formation was increased from 18ps/nm/Km for the standard SMF to more than -100ps/nm/Km for the high dispersion

fibers. The motivation of increasing the dispersion of the fibers is that the length of the fibers can be reduced to achieve the same amount number of time delay. Due to the small index variation over the transverse cross section, modal characteristics of conventional fibers including the high dispersion fibers cannot be changed significantly, thus resulting a limited dispersion ability. Photonics crystal fibers have the potential to overcome this shortcoming. Photonics crystal fibers are a new class of optical waveguides [23]. Their dispersion ability can be tailored greatly by appropriate designing the fiber structures. The importance of such high-dispersion photonics crystal fibers was first accepted for dispersion compensation [25]. Then it soon be realized they are also very useful for generating true-time delay for microwave phased array antennas [26]. There are two basic guiding mechanism in photonics crystal fibers: modified total internal reflection (MTIR) and photonic bandgap (PBG) guiding [27]. The core region of the photonics crystal fibers based on MTIR is still the glass material with doping materials. There are lots of air holes surrounding the core region for this type of photonics crystal fibers. The physical guiding mechanism of this type of fiber is similar with conventional fibers except their cladding index has been greatly reduced. For the PBG guiding mechanism based photonic crystal fibers, their physical guiding mechanism cannot be simply explained using TIR phenomenon. A so-called photonic bandgap concept is used to explain the huge dispersion ability of such fibers. According to this theory, the wavelength near the photonic bandgap has very large dispersion ability (several-thousand ps/nm/Km or even higher). With such huge dispersion ability, the length of the fibers used for microwave phased array antennas can be reduced greatly. Although photonic crystal fibers provide such great performance, the research and development efforts in

this area are still needed to overcome such as loss and manufacturing issues before they can be deployed in a real phased array antenna system.

### 2.2.3 Chirped fiber grating based true-time delay formation

Cruz et al. proposed the use of chirped fiber grating to generate continuous true-time delay for microwave phased array antennas [28]. They demonstrated a chirped grating which can produce continuously tunable time delay by continuously tuning the wavelength of the optical carrier. A chirped fiber grating is a highly dispersive reflector whose time delay  $\tau$  depends strongly on the optical wavelength  $\lambda$ . If an optical carrier is modulated by a microwave signal of frequency  $f_{RF}$ , the microwave signal will get a phase delay given by  $2\pi f_{RF} \tau$ . Hence, the fiber grating produces a linear phase shift in the modulating signal whose slope can be continuously varied by changing the wavelength of the optical carrier. Corral et al. develop a true-time delay formation system employing four tunable lasers and a chirped fiber grating [29]. The advantage of this approach is that only one chirped fiber grating is needed in the system. On the other hand, this approach will need a separate tunable laser for each antenna element. It will be impossible considering the thousands of antenna elements in a real phased array antenna system.

## 2.3 Summary

A short overview of continuous-tunable true-time delay schemes is made in this chapter. There are three basic approaches to implement continuous-tunable TTD devices: dispersive fibers, photonic crystal fibers, and fiber gratings. In the next chapter we will present the proposed volume-holographic-gratings based true-time delay devices.

## 2.4 Reference

- 1: W. Ng, A. A. Walston, G. L. Tangonan, J. J. Lee, I. L. Newberg, and N. Bernstein, The first demonstration of an optically steered microwave phased array antenna using true-time-delay, *IEEE Journal of Lightwave Technology*, 9, 1124, 1991.
- 2: D. Dolfi, J. P. Huignard, and M. Baril, Optically controlled true-time delays for phased array antenna, *SPIE*, 1102, 152, 1989.
- 3: D. Dolfi, F. Michel-Gabriel, S. Bann, and J. P. Huignard, Two-dimensional optical architecture for time-delay beam forming in a phased-array antenna, *Optics Letters*, 16, 255, 1991.
- 4: D. Dolfi, P. Joffre, J. Antoine, J.-P. Huignard, D. Philippet, and P. Granger, Experimental demonstration of a phased-array antenna optically controlled with phased and time delays, *Applied Optics*, 35, 5293, 1996.
- 5: N. A. Riza, Transmit/receive time-delay beam-forming optical architecture for phased-array antennas, *Applied Optics*, 30, 4594, 1991.
- 6: N. A. Riza, Liquid crystal-based optical time delay control system for wideband phased arrays, *SPIE*, 1790, 171, 1992.
- 7: A. M. Levine, Use of fiber optic frequency and phase determining element in radar, *Proceedings of the 33<sup>rd</sup> Annual Symposium on Frequency Control*, IEEE, 436, 1979.
- 8: P. M. Freitag and S. R. Forrest, A coherent optically controlled phased array antenna system, *IEEE Microwave and Guide Wave Letters*, 3, 292, 1993.

- 9:L. Xu, R. Taylor, and S. R. Forrest, True-time delay phased array antenna feed system based on optical heterodyne techniques, *IEEE Photonics Technology Letters*, 8, 160, 1996.
- 10:D. K. T. Tong and M. C. Wu, A novel multiwavelength optically controlled phased array antenna with a programmable dispersion matrix, *IEEE Photonics Technology Letters*, 8, 812, 1996.
- 11:P. Goutzoulis and D. K. Davies, Hardware-compressive 2-D fiber-optic delay line architecture for time steering of phased-array antennas, *Applied Optics*, 29, 5353, 1990.
- 12:P. Goutzoulis and D. K. Davies, All-optical hardware-compressive wavelength multiplexed fiber optic architecture for true-time delay steering of 2-D phased array antenna, *SPIE*, 1703, 604, 1992.
- 13:P. Goutzoulis, D. K. Davies, J. Zomp, P. Hrycak, and A. Johnson, Development and field demonstration of a hardware-compressive fiber-optic true-time delay steering system for phased array antennas, *Applied Optics*, 33, 8173, 1994.
- 14:Z. Fu and R. T. Chen, High packing density optical true-time delay lines for phased array antenna applications, *Recent Research Developments Series*, 1, Dec. 1998.
- 15:Y. H. Chen, R. T. Chen, A fully packaged true time delay modules for a K-band phased array antenna demonstration, *IEEE Photonics Technology Letter*, 14, 1175, 2002.
- 16:S. Yegnanarayanan, P. D. Trinh, and B. Jalali, Recirculating photonic filter: a wavelength-selective time delay for phased array antennas and wavelength code division multiple access, *Optics Letter*, 21, 10, 1996.
- 17:W. D. Jemison and P. R. Herczfeld, Acousto-optically controlled true-time delay, *IEEE Microwave and Guided Wave Letters*, 3, 72, 1993.

- 18:L. H. Gesell, R. E. Feinleib, J. L. Lafuse, and T. M. Turpin, Acousto-optic control of time delays for array beam steering, SPIE, 2155, 194, 1994.
- 19:E. N. Toughlian and H. Zmuda, A photonic variable RF delay line for phased array antennas, Journal of Lightwave Technology, 8, 1824, 1990.
- 20:E. H. Monsay, K. C. Baldwin, and M. J. Caucuitto, Photonic true time delay for high-frequency phased array systems, IEEE Photonics Technology Letters, 6, 118, 1994.
- 21:R. A. Soref, Optical dispersion technique for time-delay beam steering, Applied Optics, 31, 7395, 1992.
- 22:S. T. Johns, D. A. Norton, C. W. Keefer, R. Erdmann, and R. A. Soref, Variable time delay of microwave signals using high dispersion fibre, Electronics Letters, 29, 555, 1993.
- 23:R. D. Esman, M. Y. Frankel, J. L. Dexter, L. Goldberg, M. G. Parent, D. Stilwell, and D. G. Cooper, Fiber-optic prism true time-delay antenna feed, IEEE Photonics Technology Letters, 5, 1347, 1993.
- 24:J. Broeng, D. Mogilevstev, S. E. Barkou, and A. Bjarklev, Photonic crystal fibers: a new class of optical waveguides, Opt. Fiber Technol., 5, 305, 1999.
- 25:T. A. Birks, D. Mogilevtsev, J. C. Knight, and P. S. J. Russell, Dispersion compensation using single material fibers, IEEE Photonics Technology Letter, 11, 674, 1999.
- 26:T. D. Engeness, M. Ibanescu, S. G. Johnson, O. Weisberg, M. Skorobogatiy, S. Jacobs, and Y. Fink, "Dispersion tailoring and compensation by modal interactions in OmniGuide fibers," Opt. Express 11 (10), 1175-1198, 2003.

27:J. D. Joannopoulos, R. D. Meade, and J. N. Winn, Photonic crystal: modeling the flow of light, Princeton, NJ: Princeton Univ. Press, 1995.

28:J. L. Cruz, B. Ortega, M. V. Andres, B. Gimeno, D. Pastor, J. Capmany, and L. Dong, Chirped fiber gratings for phased array antenna, Electronics Letters, 33, 545, 1997.

29:J. L. Corral, J. Marti, S. Regidor, J. M. Fuster, R. Laming, and M. J. Cole, Continuously variable true time-delay optical feeder for phased-array antenna employing chirped fiber gratings, IEEE Trans. Microwave and Tech., 45, 1531, 1997.

## Chapter 3

### Proposed true-time delay formation approach and phased array antenna system

We will briefly describe the proposed true-time delay formation scheme and the structure of phased array antenna system. A general description of phased array antenna is also given. Figure-of-merits for microwave photonics system is also explained in this chapter.

#### 3.1 Proposed delay formation scheme and phased array antenna system

Holographic-gratings based glass waveguides have been researched for a number of applications: such as inter-boards optical interconnection and discrete true-time delay for K-band phased array antenna [1,2]. Pseudoanalog TTD devices were also explored in our group with this technology [3]. Due to the limited dispersion ability of TTD in [3], the dispersion-enhanced time delay devices were proposed and developed in this work. With this approach, continuous-tunable true-time delay can be generated within the devices. Furthermore, a 1-dimension linear phased array antenna system and a 2-dimension phased array antenna with the fabricated devices were developed and demonstrated. The true-time delay formation scheme is shown in Figure 3.1 in which holographic-gratings based glass waveguides have a thickness of  $h$ ,  $h + \Delta h$ , ...,  $h + n\Delta h$ , respectively. The thickness difference between the adjacent devices is constant:  $\Delta h$ . The holographic-gratings are fabricated on top of each strip and the grating structures of all of the strips are exactly the same. For the surface normal incident beams, they have the same diffraction angles within the strips. There is a time delay  $\Delta T$  between the adjacent

outputs beams since they travel different optical path within the glass waveguides. For the outputs having only one bounce within the glass strips,  $\Delta T$  is determined to be

$$\Delta T = \frac{2n\Delta h}{c \cos(\theta)} \quad (3.1)$$

where  $n$  is refractive index of the glass,  $\Delta h$  is the thickness difference between the adjacent strips,  $c$  is light speed in vacuum and  $\theta$  is the diffraction angle of the incident beam  $\lambda$  within the glass strips. The overall time delay is determined by the abovementioned parameters. The diffraction angle  $\theta$  is a function of incident wavelength  $\lambda$  and their relationship is determined by the dispersion equation which will be shown in chapter 4. By tuning the incident wavelength  $\lambda$ , the diffraction angle  $\theta$  can be changed continuously, thereby making the true-time-delay continuously tunable.

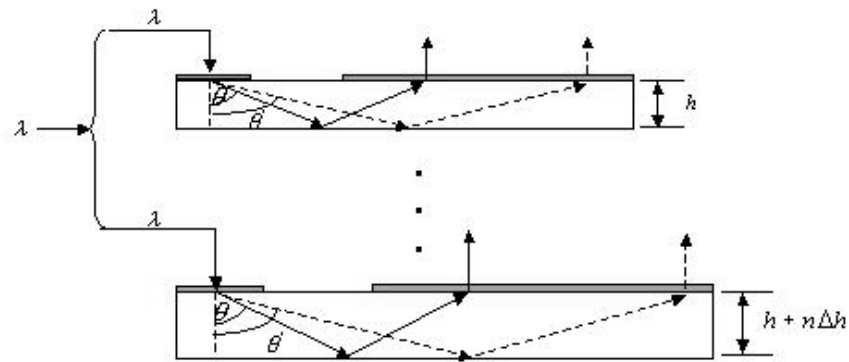


Figure 3.1 Schematic illustration of time delay formation

The proposed 2-dimension phased array antenna system structure is shown in Figure 3.2. Wavelength conversion (WC) within semiconductor optical amplifiers is used to realize a 2D beam steering function. This system structure idea was first proposed in

[4] for the discrete true-time delay based phased array antenna. In this work, we extend this idea to continuous-tunable TTD based phased array antenna. One of the advantages of the designed system is that only one laser is used to control all of the four devices, which is a great improvement compared with previous approaches [3,5]. Compared with [5] of multiple-wavelength schemes requiring stringent synchronization among lasers, the complexity and the cost of this new system can be greatly reduced.

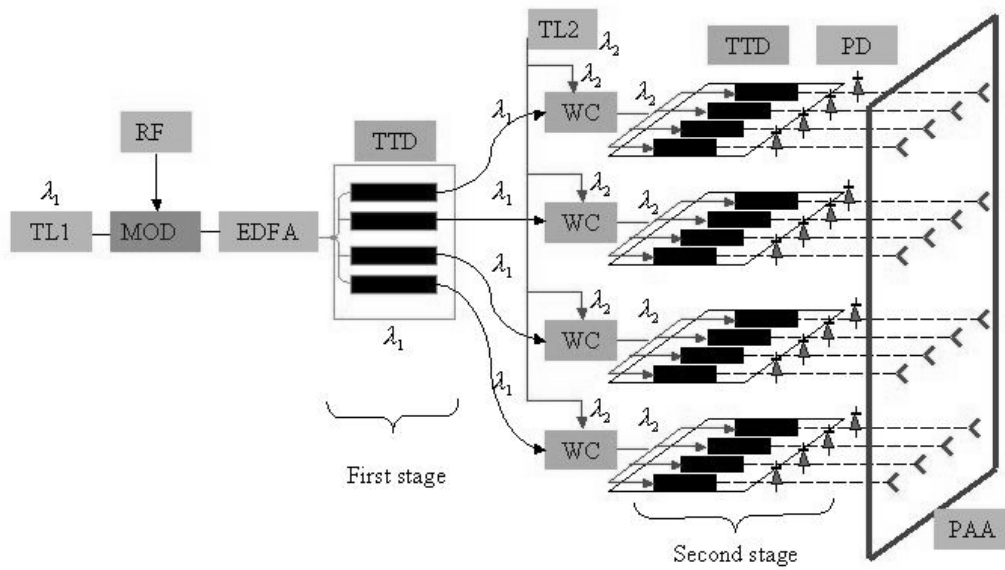


Figure 3.2 2-dimension phased array antenna system structure

TL: tunable laser, MOD: modulator, EDFA: erbium-doped fiber amplifier, TTD: true-time delay, PD: photo detector, PAA: phased array antenna.

### 3.2 Wavelength conversion in semiconductor optical amplifier (SOA)

Wavelength conversion in semiconductor optical amplifiers is used in this work to help develop an 2-dimension phased array antenna system. The fundamental working mechanism used for this work is cross-gain modulation which comes from the gain

saturation of semiconductor optical amplifiers. Here we give a brief explanation why it can be used to transfer time delay information within our system. Figure 3.3(a) and (b) are the illustration of the structure and principle of wavelength conversion based on cross-gain modulation. Semiconductor optical amplifier will saturate gradually with increasing input optical power. So the incoming modulated optical signal  $\lambda_1$  will modulate the gain of semiconductor optical amplifier. This modulated gain characteristics will modulate the incoming CW optical beam at  $\lambda_2$ . The optical beam  $\lambda_2$  will have the same signal characteristics with  $\lambda_1$  at the output of semiconductor optical amplifier except a phase inversion. There are four wavelength conversion subsystems in the proposed phased array antenna systems. They all will have a phase-inversion after wavelength conversion. So the relative time delay among them will not change. Figure 3.4 shows how time delay is transferred after wavelength conversion among the four devices.

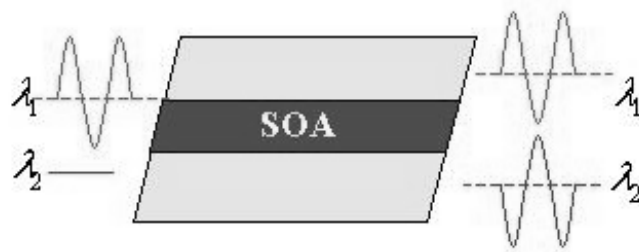


Figure 3.3 (a) Wavelength conversion structure

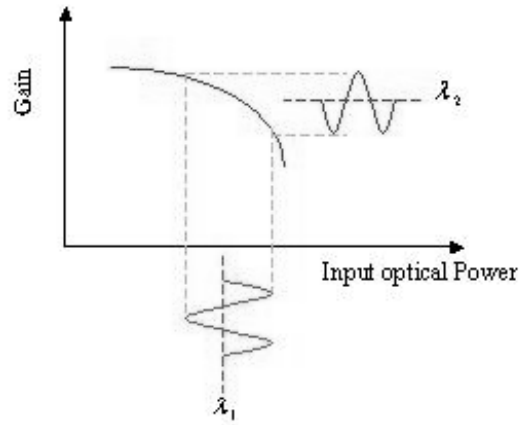


Figure 3.3 (b) Principle of cross-gain modulation based wavelength conversion

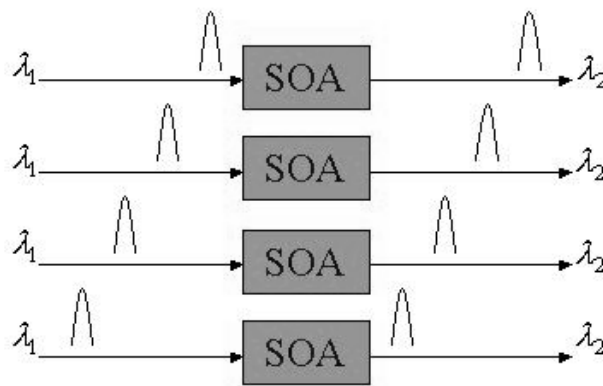


Figure 3.4 Illustration of time delay transfer by wavelength conversion

### 3.3 General issues of phased array antenna system

#### 3.3.1 Grating lobes

For the phased array antenna system, one design issue is to avoid the grating lobes.

For a maximum beam steering angle of  $\theta_M$ ,  $d/\lambda$  has to satisfy the following requirement

to avoid the grating lobes [5]

$$\frac{d}{\lambda} \leq \frac{1}{1 + |\sin \theta_M|} \quad (3.2)$$

where  $d$  is the element spacing and  $\lambda$  is the microwave wavelength. For a general equal-element-spacing planar phased array antenna distribution, its electrical field can be written as

$$E(\theta, \phi) = \sum_{m=1}^{N_x} \sum_{n=1}^{N_y} I_{mn} \exp\{i\phi_{mn} + ik[(m-1)d_x \cos \phi + (n-1)d_y \sin \phi]\sin \theta\} \quad (3.3)$$

Assuming the  $d/\lambda = 0.5$  and without considering the element factor ( $I_{mn} = 1$ ), the equation (3.3) can be plot as in Figure 3.5 for a 4x4 planar array. If  $d/\lambda > 0.5$ , the grating lobes will appear as in Figure 3.6. In plotting the Figure 3.6, we set  $d/\lambda = 2$ . The Figure 3.5 and the Figure 3.6 also show the corresponding contour plots from which the radiation pattern spatial distribution in a 2-dimension plane can be clearly seen.

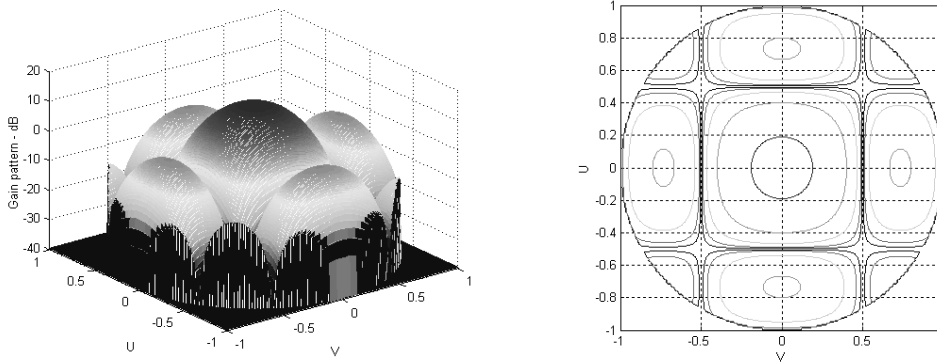


Figure 3.5 Plot of radiation pattern for a 4x4 element phased array antenna

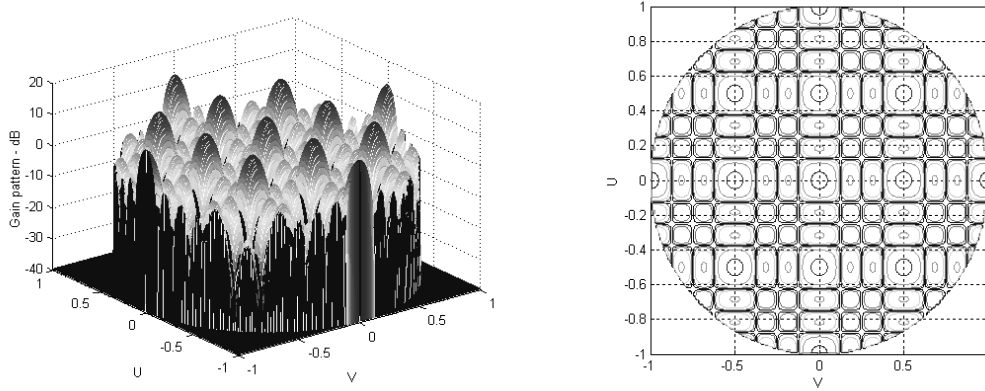


Figure 3.6 Plot of radiation pattern for a 4x4 element phased array antenna

### 3.3.2 Beamwidth and bandwidth

The half-power points on a uniform array pattern can be found by using

$$E(\theta_0 + \theta_{3dB} / 2) = \frac{\sin\{N\pi d[\sin(\theta_0 + \theta_{3dB} / 2) - \sin \theta_0]\lambda\}}{N \sin\{\pi d[\sin(\theta_0 + \theta_{3dB} / 2) - \sin \theta_0]\lambda\}} = \sqrt{\frac{1}{2}}, \quad (3.4)$$

where  $\theta_{3dB}$  is the 3 dB beamwidth. The 3dB beamwidth for a beam scanned at angle  $\theta_0$  is given approximately by

$$\theta_{3dB} = \sin^{-1}\left(\sin \theta_0 + 0.4429 \frac{\lambda}{Nd}\right) - \sin^{-1}\left(\sin \theta_0 - 0.4429 \frac{\lambda}{Nd}\right). \quad (3.5)$$

For large arrays, this half-power point can be simplified to

$$\theta_{3dB} = \frac{0.8858\lambda}{Nd \cos \theta_0} \quad (3.6)$$

Note that the half power beamwidth is inversely proportional to the array length and the cosine of the scanning angle.

There are several factors that affect the bandwidth of an array, including changes of element input impedance with frequency, changes of array spacing in wavelengths that may allow grating lobes, changes in element beamwidth, etc. For arrays controlled by phase shift, the beam direction will also change with the frequency. This direction change with the working frequency can be given by

$$\frac{\sin \theta}{\sin \theta_0} = \frac{f_0}{f} \quad (3.7)$$

Suppose the main beam has moved from  $\theta_0$  to 3 dB directions  $\theta_1$  and  $\theta_2$  for the upper and lower frequencies; the fractional bandwidth is then given by

$$BW = \frac{f_2 - f_1}{f_0} = \frac{(\sin \theta_1 - \sin \theta_2) \sin \theta_0}{\sin \theta_1 \sin \theta_2} \quad (3.8)$$

For a large array, the above equation can be written as

$$BW \approx \frac{\theta_{3dB}}{\sin \theta_0}. \quad (3.9)$$

For a uniformly distributed and uniformly excited array, this fractional bandwidth is thus

$$BW \approx \frac{\theta_{3dB}}{\sin \theta_0} \approx \frac{0.886\lambda}{L \cos \theta_0 \sin \theta_0} = \frac{1.772\lambda}{L \sin 2\theta_0}. \quad (3.10)$$

For true-time delay scanned array, there is no bandwidth limit in the first order because there is no beam squint.

### 3.4 Figure-of-merits of microwave photonics system

The developed optical-controlled phased array antenna system belongs to the microwave photonic system. Figure-of-merits of a microwave photonics system are frequency response, link gain, distortion performance, and noise figure.

Frequency response is the system response to the different modulation frequency. It is directly related to the bandwidth of the system. 3-dB bandwidth is usually defined as the frequency at which the system response drops 3dB compared with the peak response value. Link gain is defined as the difference between the output electrical power and the input electrical power. This parameter can give the total signal gain (or loss) of the system. Distortion analysis is more complex than the above two. In a microwave photonics system, the outputs of the electrical signals include both the signals at the fundamental frequencies and the distortions at the harmonic and inter-modulation (IM) frequencies. The existence of the distortion frequencies is due to the nonlinear transfer function of the microwave photonics system. More specifically, it is because of the nonlinear transfer function of the optical and electrical components, such as lasers, modulators, semiconductor optical amplifiers, photo detectors. When a sinusoidal modulated optical signal passes through these nonlinear-transfer-function components, the sinusoidal modulated signal will be distorted and the harmonic distortions will be generated at the output of the system. Figure 3.7 shows a distribution of the fundamental frequencies  $\omega_1$ ,  $\omega_2$  and the distortion frequencies as the results of the second order and the third order harmonic mixing as well as IM frequencies. The distortion is detrimental in the microwave photonics systems as it will decrease signal-noise-ratio (SNR) and degrade noise figure (NF) of the system. If the microwave input power at the fundamental frequency increases, the output distortion at distortion frequencies will increase also and they increase faster than the desired signal at the fundamental frequency. Eventually the power at distortion frequencies will exceed the signal power at the fundamental frequency. The reason for this could be found from some general

references such as in [6]. To design a link to work in the distortion-free region, the power of the distortion frequencies should be lower than the noise level of the system. Dynamic range is defined as the maximum signal-to-noise ratio before the distortion frequency is higher than the noise level. Figure 3.8 is used to illustrate the definition the dynamic range for different harmonic frequencies. Among these different orders of distortion, the third order intermodulation (IM) distortions at  $2\omega_1 - \omega_2$  and  $2\omega_2 - \omega_1$  are the closest to the fundamental frequencies and most likely will lie within the detection bandwidth. The distortion at frequency  $2\omega_1 - \omega_2$  or  $2\omega_2 - \omega_1$  is usually called spurious-free dynamic range (SFDR).

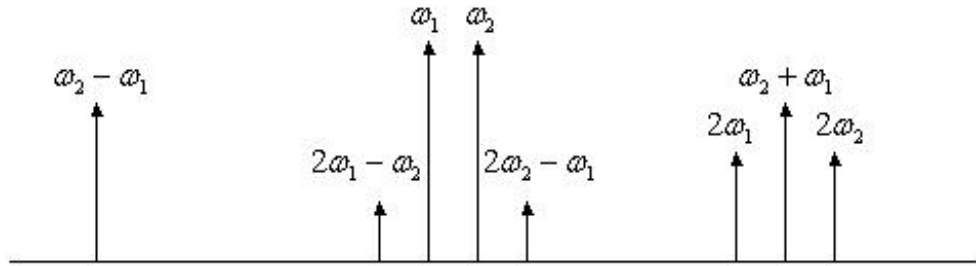


Figure 3.7 Distribution of the fundamental and distortion frequencies

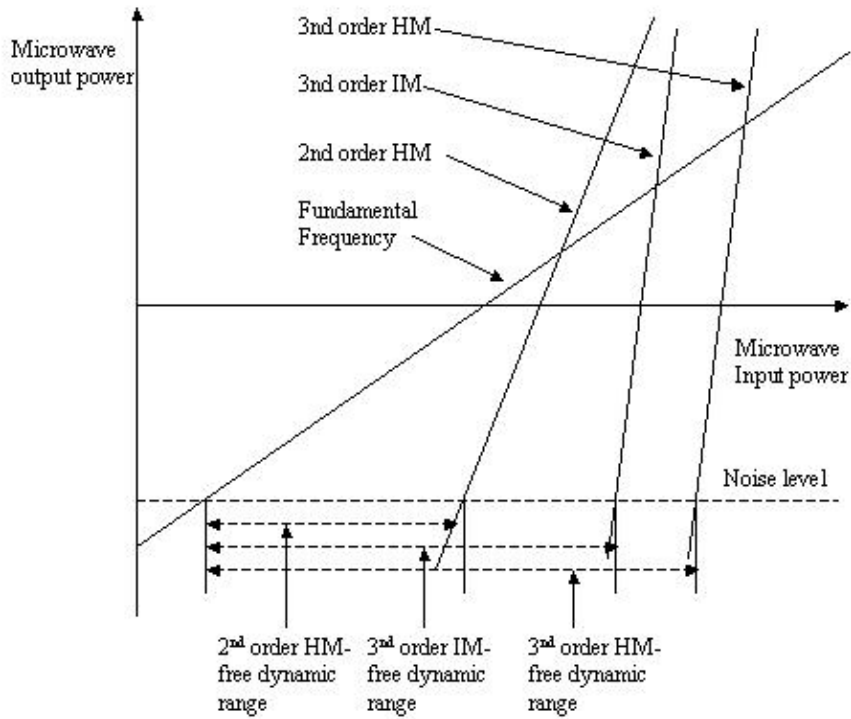


Figure 3.8 Illustration of definition of distortion free dynamic ranges

Noise plays important roles in determining the minimum magnitude of the signal that can be transmitted by the optical system. It is also important in determining the maximum SFDR (spurious free dynamic range) for microwave photonics system. Noise figure is a very useful figure-of-merit of microwave photonics system and it is defined as the ratio between the amplifier input and output electrically equivalent SNR,

$$NF = \frac{(SNR)_{in}}{(SNR)_{out}} \quad (3.11)$$

We will examine these parameters in chapter 6.

### 3.5 Summary

We give an overview of continuous-tunable true-time delay formation schemes in this chapter. In the next chapter we will present the volume-holographic-gratings based true-time delay devices including design, fabrication and characterization.

### 3.6 Reference

- 1:G. Kim, X. Han, R. Chen, A method for rebroadcasting signals in an optical backplane bus system, *IEEE Journal of Lightwave Technology*, 19, 959, 2001.
- 2:Y. Chen and R. Chen, A fully packaged true time delay module for a K-band phased array antenna system demonstration, *IEEE Photonics Technology Letter*, 14, 1175, 2002.
- 3:Z. Fu, C. Zhou, R. Chen, Waveguide-hologram-based wavelength-multiplexed pseudoanalog true-time-delay module for wideband phased-array antenna, *Applied Optics*, 38, 3053, 1999.
- 4:Z. Shi, Y. Jiang, H. Brie, F. Zhao, Y. Chen, R. Chen, Continuously delay-time tunable-waveguide hologram module for X-band phased array antenna, *IEEE Photonics Technology Letter*, 15, 972, 2003.
- 5:Brookner, *Practical phased array antenna systems*, Artech House, Boston, 1991.
- 6: W. S. C. Chang, *RF photonic technology in optical fiber links*, Cambridge University Press, 2002.

## Chapter 4

### Holographic-gratings based continuous tunable true-time delay devices

In this chapter we will describe the volume-holographic-gratings based true-time delay (TTD) devices including simulation, design, fabrication and characterization.

#### 4.1 Design

The two most important issues need to be considered in designing the volume-holographic-gratings based true-time delay devices are:

- (1) Dispersion ability of the volume holographic gratings based TTD devices
- (2) Diffraction efficiency across a given wavelength tuning range

To accomplish the first purpose, the dispersion equation of the holographic grating should be derived first. If the phase-matching (or Bragg) condition is perfectly satisfied, it is easy to use graphic method to solve this problem [1,2]. Figure 4.1 (a) shows a general case of arbitrary incident angle  $\theta$  defined as the angle between the incident beam and the surface normal direction and (b) shows our interested case of  $\theta = 0^\circ$ , the surface normal incident case that would be helpful for the packaging purpose. If the phase matching condition is met, the wave vector  $k$  of the incident beam, the wave vector  $k'$  of the diffracted beam, and the grating vector  $K$  form a closed triangle. Here  $k = 2\pi n/\lambda$ ,  $k' = 2\pi n'/\lambda$ ,  $\lambda$  is the wavelength in free space,  $n$  is the average refractive index of the medium.  $\alpha$  is the diffraction angle defined as the angle between the diffraction beam and

the surface normal direction.  $K$  is grating vector and it is defined as  $2\pi/\Lambda$ ,  $\Lambda$  is the grating period. It should be pointed out the wave vectors  $k$ ,  $k'$ , the incident angle  $\theta$  and the diffraction angle  $\alpha$  are all measured in the diffractive medium.

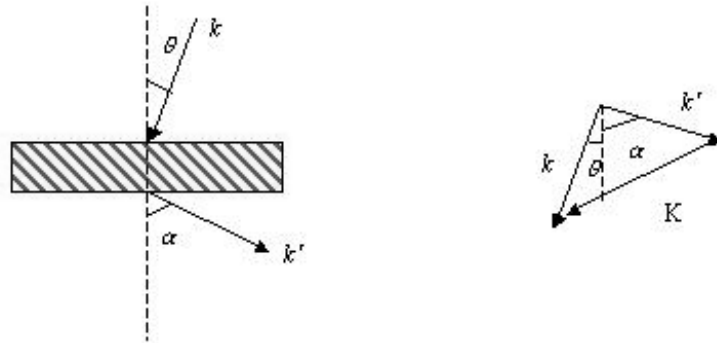


Figure 4.1(a) Configuration for non surface normal incident case

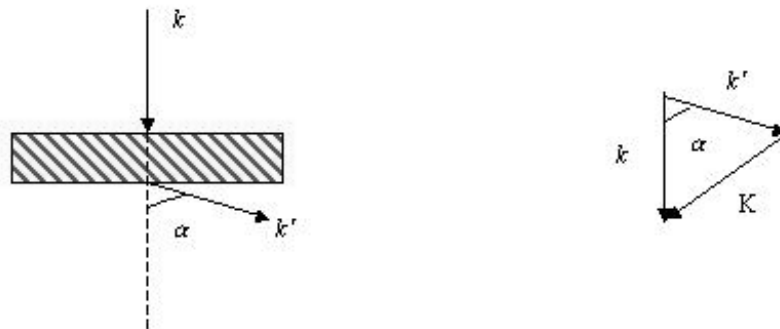


Figure 4.1(b) Configuration for surface normal incident case

The Bragg condition for volume holographic gratings can be written as following in the vector form,

$$k' = k - K, \tag{4.1}$$

or expressed in the scalar form,

$$\frac{\Lambda}{\sin \varphi} (\sin \theta + \sin \alpha) = \frac{\lambda}{n}, \quad (4.2)$$

Here  $\varphi$  is the angle between the grating vector and the surface normal direction, and called slant angle. Equations (4.2) can be used to derive the dispersion equation of the holographic grating.

For the case of  $\theta = 0^\circ$ , equation (4.2) can be written as:

$$\frac{\Lambda}{\sin \varphi} \sin \alpha = \frac{\lambda}{n} \quad (4.3)$$

Take the derivative of the (4.3) at the both sides and substitute (4.3) back to the derivative form, the dispersion equation is finally written as:

$$\frac{d\theta}{d\lambda} = \frac{\tan \theta}{\lambda} \quad (4.4)$$

From the equation (4.4), it is easy to see, for the surface normal incident case, dispersion ability of the holographic grating is directly proportional to the  $\tan \theta$  and inversely proportional to the wavelength  $\lambda$ . Fig. 4.2 shows the dispersion  $\frac{d\theta}{d\lambda}$  vs. diffraction angle

$\theta$ . It can be seen that the dispersion ability of the holographic gratings is not a linear function of the diffraction angle. When the diffraction angle is less than about  $70^\circ$ , the slope of the dispersion curve is relatively flat. The slope of the dispersion curve will increase considerably when the diffraction angle is increased beyond a certain angle which is at about  $70^\circ$ . To make a device having considerable dispersion ability, we have to choose a diffraction angle of at least larger than  $70^\circ$ . On the other hand, the 3-dB bandwidth will decrease with the increasing diffraction angle. This is because of the

faster deviation from the phase-matching condition for the bigger diffraction angle. So the overall design would be a tradeoff among the diffraction angle, 3-dB bandwidth and device size. Now let's first calculate the diffraction efficiency of the holographic grating for a given wavelength tuning range, and then find the 3-dB bandwidth from the diffraction efficiency calculation results.

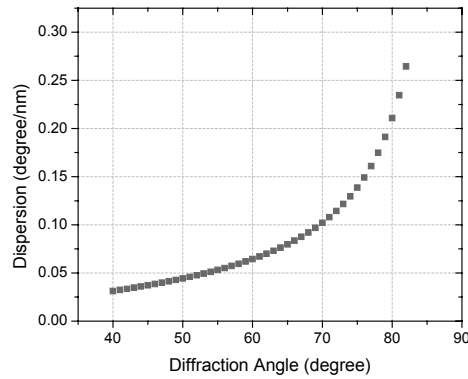


Figure 4.2 Dispersion ability vs. diffraction angle

There are several well-developed theories for analyzing volume holographic gratings. For volume holographic grating with a grating period less than the working wavelength, vigorous diffraction theories, such as the integral method, the differential method, the coupled-wave method, the modal method, the finite-elements method, and the boundary element method, are needed for the analysis [2,3,4,5,7,8,9]. For our analysis, the coupled wave method is used which is originally developed by [2]. As a general analysis, we consider a beam is incident on the transmission volume hologram with an incident angle of  $\theta$  with respect to the surface-normal direction, which is shown in Figure 4.1(a). For an S-polarized optical beam (the reason why to analyze S-polarized component here will become clear in the following analysis), the diffraction efficiency is

$$\eta_s = \frac{[\sin(\nu^2 + \xi^2)^{1/2}]^2}{1 + (\xi^2/\nu^2)}, \quad (4.5)$$

where

$$\nu = \frac{\kappa_s d}{\sqrt{C_R C_S}} \quad (4.6)$$

$$\xi = -\Delta\lambda k^2 d / 8\pi n C_S = \Delta\theta k d \sin(\varphi - \theta) / 2C_S \quad (4.7)$$

$$C_R = \cos\theta, C_S = \cos\theta - K \cos\varphi / k, \quad (4.8)$$

$$\kappa_s = \pi\Delta n / \lambda. \quad (4.9)$$

In Equations (4.5)-(4.9),  $\Delta n$  is the amplitude of the refractive index modulation,  $\theta$  is the incident Bragg angle measured in the hologram medium,  $\Delta\theta$  is the deviation of the incident angle from the Bragg angle,  $d$  is the thickness of the holographic grating layer,  $\lambda$  is the free-space wavelength of incident light,  $n$  is the average refractive index of the grating medium, and  $\varphi$  is the slanted angle of the grating with respect to the medium boundaries,  $K$  is the grating vector, and  $k$  is the propagation constant of the light inside the medium.

For a P-polarized input optical signal, all the equations are the same except that the  $\kappa_s$  is replaced by  $\kappa_p$ ,

$$\kappa_p = -\kappa_s \cos 2(\theta - \varphi). \quad (4.10)$$

From the equations (4.5)-(4.9), the 3-dB bandwidth can be calculated and the results are shown in Figure 4.3. For a diffraction angle of  $45^\circ$ , its 3-dB bandwidth exceeds 100nm to about 120nm. As for the diffraction angle at  $80^\circ$ , its 3-dB bandwidth shrinks to about 13nm. From the dispersion shown in Figure 4.2 and the 3-dB bandwidth

shown in Figure 4.3, the time delay for a 3-dB bandwidth wavelength tuning range corresponding to the different diffraction angles can be calculated. The calculation result is shown in Figure 4.4. From this curve it is easy to see a large diffraction angle will increase the time delay within the 3-dB optical bandwidth. So from the design point of view, increasing diffraction angle will be help to generate more time delay within a 3-dB optical bandwidth. On the other hand, a diffraction angle close to  $90^\circ$  degree is unacceptable as the longitudinal length of the time delay devices will be too long. Considering these factors, we finally choose a diffraction angle at  $80^\circ$ . The reconstruction wavelength for the phase-matching condition can be varied in the design. Three angles were marked in Figure 4.2 and they are  $45^\circ$ ,  $60^\circ$  and  $80^\circ$ . The waveguide-holograms with the diffraction angles of  $45^\circ$  or  $60^\circ$  were previously fabricated in our lab for other applications [9, 10,11]. It can be seen that the dispersion ability at the diffraction angle of  $80^\circ$  can be increased by 3.27 times compared with that of  $60^\circ$  and by 5.67 times compared with that of  $45^\circ$ . In the calculation, wavelength is shifted by 10nm from 1537nm to 1547nm and the 1537nm is chosen as reference zero point.

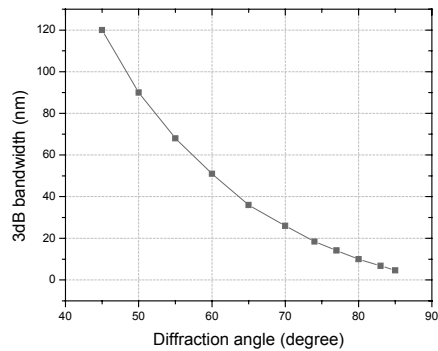


Figure 4.3 3-dB bandwidth vs. diffraction angle

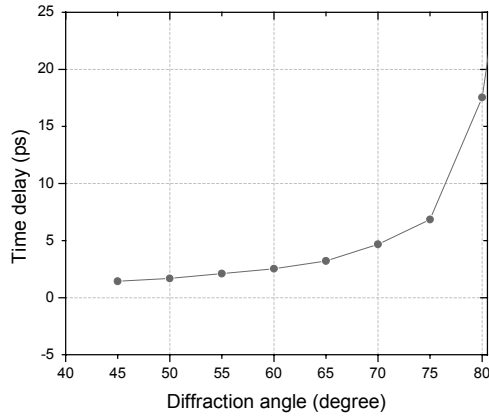


Figure 4.4 Time delay generation within a 3-dB optical bandwidth

Now let's take a look at the diffraction efficiency calculation for the different cases. If the perfect phase-matching condition is met,

$$\Delta\lambda = 0, \text{ and } \Delta\theta = 0 \quad (4.11)$$

Substitute (4.11) back to (4.5)-(4.9), we can get the diffraction efficiency vs. index modulation depth curves for different diffraction angles from the resulting equation.

Figure 4.5 shows the calculation results for three different diffraction angles:  $45^\circ$ ,  $60^\circ$  and  $80^\circ$ , corresponding to green lines, red lines and blue lines, respectively. For each angle, the S-polarization component and P-polarization component are shown separately.

We notice that the diffraction efficiency of the S-polarization component of the incident beam is increased considerably when the diffraction angle is increased from  $45^\circ$  to  $80^\circ$ .

The P-polarization component has the opposite tendency, but doesn't change as much as the S-pol. The good point is that if only the S-polarization component is used within the optical system (linear polarized optical input), the peak diffraction efficiency can be improved considerably (the insertion loss will be reduced correspondingly). On the other

hand, the drawback is that if a random polarized beam is used, this device has strong polarization sensitivity which is not acceptable for the system design. Fortunately we only use P-polarization component in our experiment.

The reason for the increased polarization dependent with the increasing diffraction angle can be intuitively explained as following. When the diffraction angle within the hologram grating is increased, the orientation between the incident beam and grating fringe approaches the optics Brewster angle closer and closer. The polarization dependent phenomenon will become more and more obvious, which can be clearly seen from Figure 4.6. From a simple optics course, the interface property can be drawn in Figure 4.7. For the  $80^\circ$  diffraction angle, the angle between the incident beam and grating fringe is  $40^\circ$ . It is not surprising to see that the device is strongly polarization dependent at this diffraction angle. Both S-polarization and P-polarization beams are drawn in the Figure 4.7 for reference.

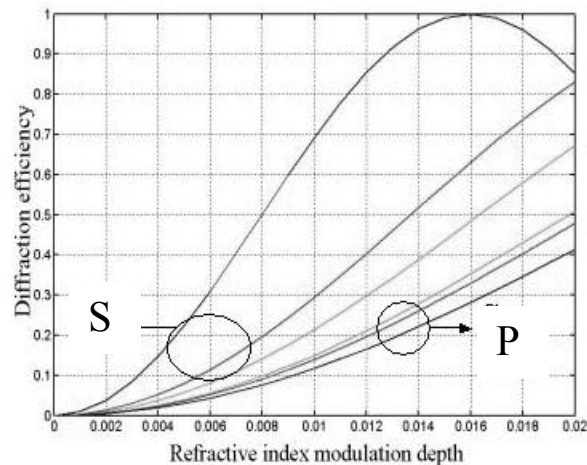


Figure 4.5 Peak diffraction efficiency vs. index modulation depth

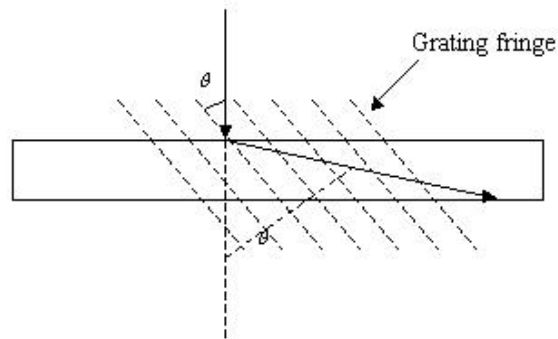


Figure 4.6 Illustration of polarization dependent phenomenon

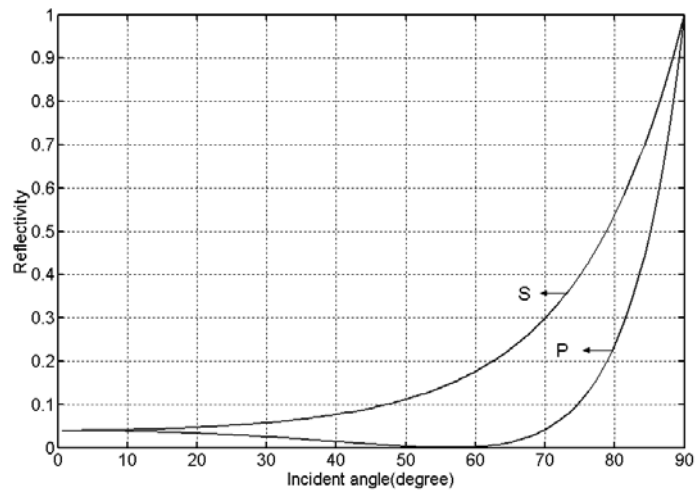


Figure 4.7 Interface reflection between air and polymer

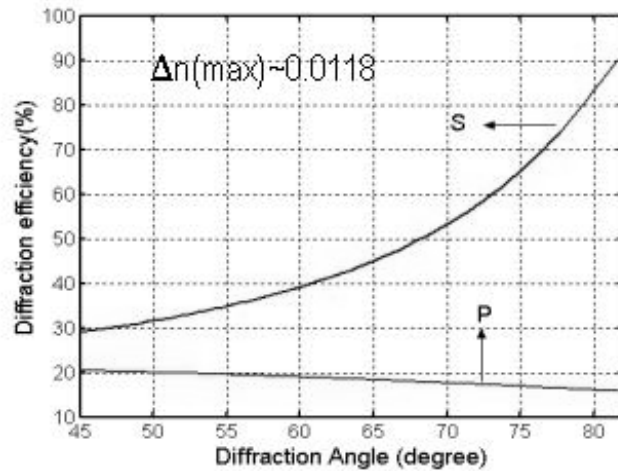


Figure 4.8 Diffraction efficiency vs. diffraction angle for S- and P- polarization

Figure 4.8 is given to show how the diffraction efficiency is enhanced for the S-polarization component with increasing diffraction angle. The true-time delay formation scheme is already shown in chapter 3 and the delay formation structure is again shown in Figure 4.9. Figure 4.10 shows the time delay as a function of both wavelength tuning range and thickness difference for a diffraction angle of  $80^\circ$ .

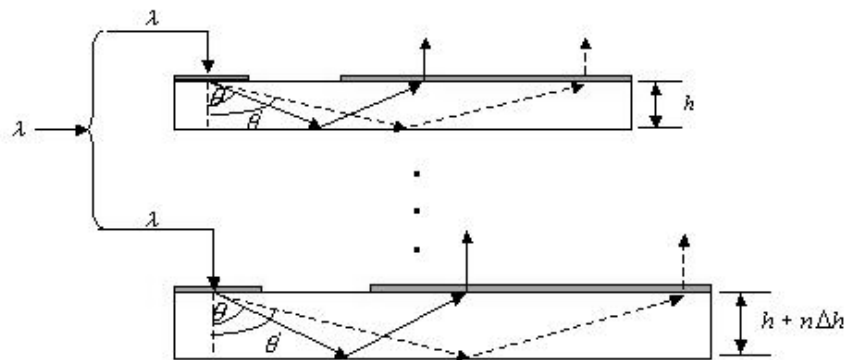


Figure 4.9 Schematic illustration of time delay formation

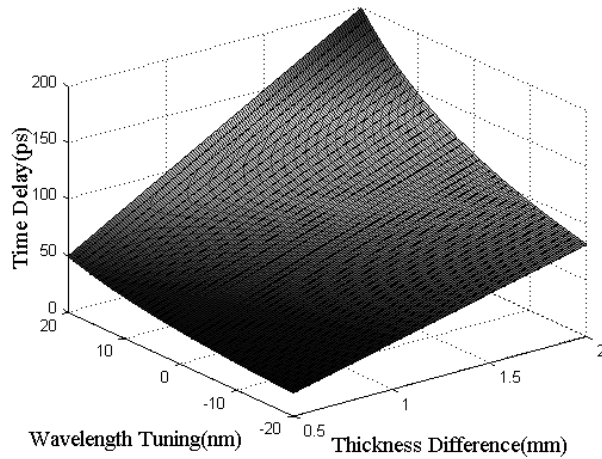


Figure 4.10 Time delay vs. wavelength tuning and thickness difference

## 4.2 Fabrication

DuPont photopolymer systems for holographic recording offer significant advantages over other media. The composition of DuPont photopolymer films typically consists of polymeric binders, acrylic monomers, and plasticizers, along with initiating systems, including initiators, chain transfer agents, and photosensitizing dyes [13]. The binder acts as the support matrix containing the other film components. The monomers serve as refractive index "carriers." The choice of monomer and binder affects the physical properties of the film and the magnitude of index modulation recorded on the film. The sensitizing dyes absorb light and interact with the initiators to begin photopolymerization of monomers. The proper choice of components allows tailoring of material and holographic properties to specific applications. The holographic photopolymer is usually coated from solvent onto a clear support, typically 50  $\mu\text{m}$  Mylar polyester film. A removable cover sheet of 25  $\mu\text{m}$  Mylar or 60  $\mu\text{m}$  polyvinylchloride

(PVC) film is used to protect the slightly tacky photopolymer. The film can be imaged with the base and coversheet intact by coupling to a master or glass plate with index matching fluid or vacuum frame. It can also be imaged by removal of the cover sheet and lamination of the film onto a glass plate, as shown in Figure 4.11. The PVC cover sheet is preferred for imaging with the cover sheet intact because of its low birefringence. In both cases the Mylar base should be oriented with its optical axis parallel to the recording laser polarization in order to minimize the rotation of laser polarization due to the birefringence of the Mylar.

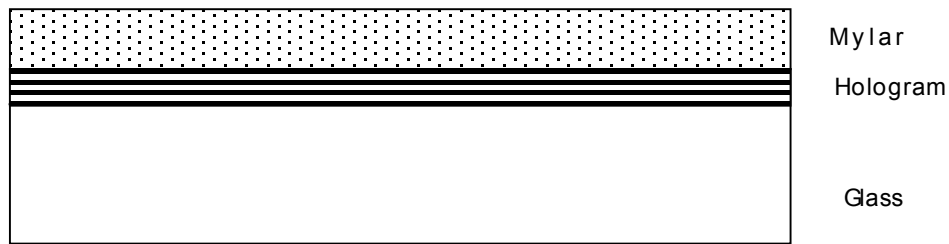


Figure 4.11 Structure of the holographic grating laminated on a glass waveguide

The process of producing holograms with DuPont materials involves three steps. First, an initial exposure records the interference pattern, which causes the initial polymerization and diffusion of the monomer molecules to bright fringes. As the conversion of monomer to photopolymer occurs, fresh monomer diffuses in from neighboring dark regions, thus setting up concentration and density gradients that result in refractive index modulation. As exposure and polymerization proceed, the initial highly viscous composition gels and hardens, diffusion is suppressed, and further hologram recording stops. A higher concentration of polymerization means a higher refractive index. Second, a uniform UV light is required for dye bleaching, completing

polymerization, and permanently fixing the images. The photopolymer materials that were used in this experiment are thick or volume hologram which records information in three dimensions. A generally accepted the criteria for Bragg regime and volume hologram is

$$Q \gg 1 \quad (5.13)$$

The  $Q$  factor is written as following according to [9]

$$Q = \frac{2\pi\lambda d}{n\Lambda^2} \quad (5.14)$$

where  $n$  is the average refractive index of the film,  $\Lambda$  is the spatial period of the formed grating structure. For the device we designed,  $d=20\text{um}$ ,  $n=1.5$ ,  $\lambda=1.5\text{um}$ ,  $\Lambda=0.778\text{um}$  (for  $80^\circ$ ),  $Q=58.77$ . In our experiments, volume phase holograms are formed in the photopolymer material through optical recording, which produces a spatial variation in the refractive index.

The hologram recording setup is shown in Figure 4.12. A Verdi laser with a wavelength of 532nm is used in the experiment. The single polarization beam is power splitted by a beam splitter first, then forming two parallel beams. The intensity of one beam can be adjusted to achieve the equal beam intensity for the two recording beams. The micro objective lenses are used to expand the laser beams, followed by spatial filters in their focal points. The expanded laser beams from the filters are collimated into the plane waves using two collimating objective lenses. For best results, the hole of the spatial filters must be placed at the focal point of the collimating lenses; the focal lengths of the collimation lens will determine the diameters of the plane waves, and therefore determine the recording area. The dark glass holder is mounted on a 3-D translation/rotation stage. The two reflection mirrors are adjustable, so that the two

recording angles  $\theta_1$  and  $\theta_2$  can be set by tuning the relative positions and angles of the dark glass holder and the two reflection mirrors.

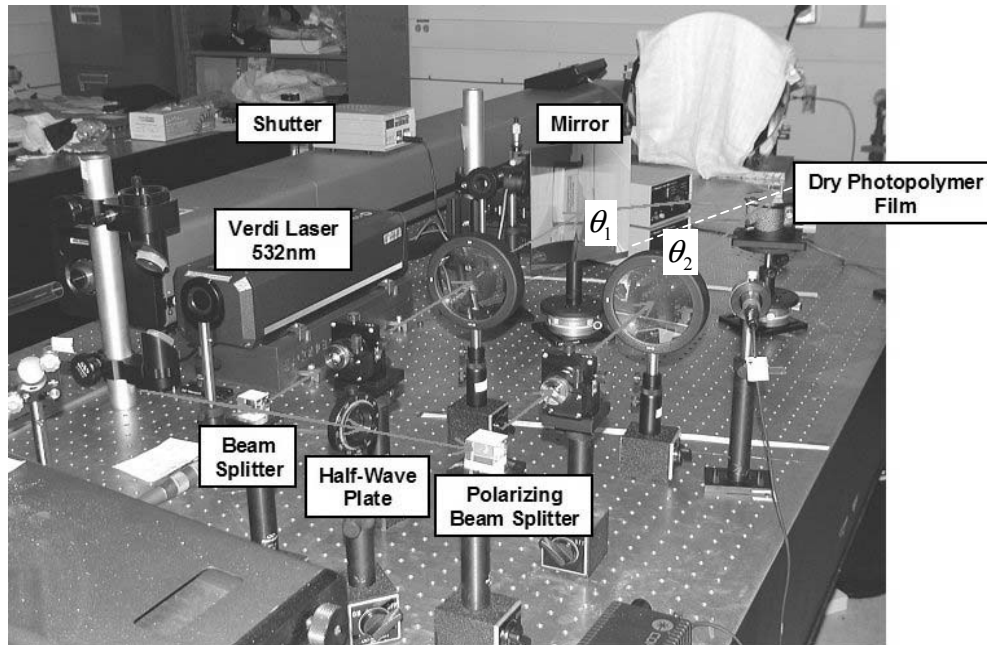


Figure 4.12 Schematic diagram of hologram recording setup

For hologram recording, the protection cover of the photopolymer film is removed, the film is laminated onto the substrate (BK-7 or quartz), and then the recording plate is put in position against the absorption dark glass plate. Between the absorption plate and the hologram substrate, an index-matching fluid is applied to eliminate the interface reflection. The absorption plate is painted dark to reduce the noise of back reflection. DuPont photopolymer HRF 600X001-20 (20  $\mu\text{m}$ ) is used in the experiment.

Various transmission holograms can be constructed by using this setup. The reconstruction wavelengths can be designed in a wide range from 500 nm to 1500 nm,

which are different from the recording wavelength. If the wavelength of the recording beam is  $\lambda$ , the grating period will be given by [2]

$$\Lambda = \frac{\lambda}{2n_r \sin\left(\frac{\theta_1 - \theta_2}{2}\right)}, \quad (5.15)$$

where  $n_r$  is the refractive index of the medium on top of the holographic emulsion ( $n_r=1$  for our case, i.e., air). To form a slanted grating coupler which converts a vertical incident wave into a total internal reflection substrate-guided mode with diffraction angle  $\theta$ , the two incident angles of the recording beams  $\theta_1$  and  $\theta_2$  are as following [15]

$$\theta_1 = \sin^{-1} \left\{ \frac{n}{n_r} \sin \left[ \frac{\theta}{2} + \sin^{-1} \left( \frac{\lambda_b}{\lambda_r} \sin \frac{\theta}{2} \right) \right] \right\} \quad (5.16)$$

$$\theta_2 = \sin^{-1} \left\{ \frac{n}{n_r} \sin \left[ \frac{\theta}{2} - \sin^{-1} \left( \frac{\lambda_b}{\lambda_r} \sin \frac{\theta}{2} \right) \right] \right\} \quad (5.17)$$

where  $n$  is the refractive index of the hologram, and  $\lambda_b$  and  $\lambda_r$  represent the wavelengths of the recording and the reconstruction waves, respectively.

To record a diffraction angle of  $80^\circ$ , a right-angle prism is needed to be placed on top of the recording medium as shown in Figure 4.13. This is because the maximum diffractive index that can be achieved is about  $60^\circ$  at the interface between the air and the photo polymer material. The maximum achievable diffraction angle in the hologram is limited by the index difference between air and hologram. The parameters for recording holographic grating can be calculated following the Figure 4.15 and Figure 4.16. In Figure 4.15, only two angles  $\theta_1$  and  $\theta_2$  are unknown, the rest parameters such as diffraction angle  $\theta$ , the incident beam wave vector  $k$ , the diffraction beam wave vector  $k'$ , the grating vector  $K$  and the recording beam wave vectors  $K'$ ,  $K''$  are known. The

recording beam wave vectors  $K'$ ,  $K''$  and the grating vector also form a closed triangle. We can calculate  $\theta_1$  and  $\theta_2$  by simple geometric relationship from the two closed triangles. After it is done, we need to use Figure 4.16 to find the beam incident angles in the free space. The  $\theta'_1$  and  $\theta'_2$  can be calculated from  $\theta_1$  and  $\theta_2$  by the refraction equation.

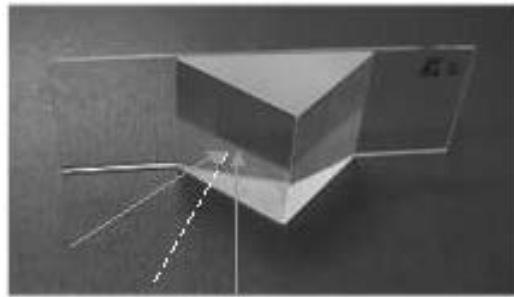


Figure 4.13 Holographic grating recording structure with prism

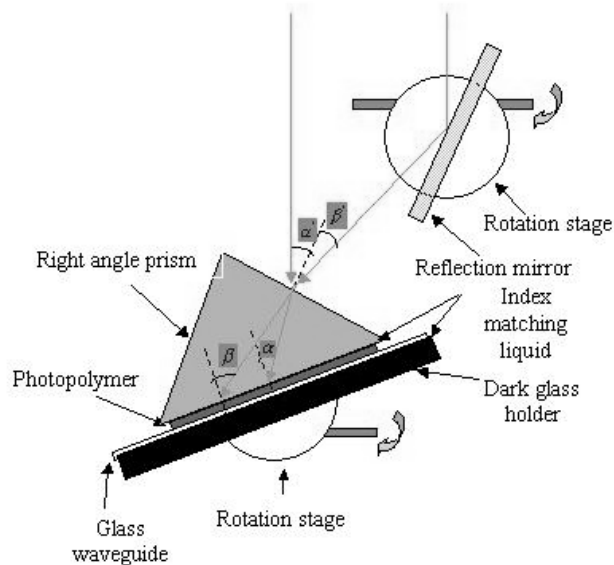


Figure 4.14 Schematic diagram for holographic grating recording with right angle prism

To design a  $80^\circ$  diffraction angle with a recording wavelength of 532nm and a reconstruction wavelength of 1550nm, the calculated results are  $\theta'_1 = 10^\circ 31'$  and  $\theta'_2 = 27^\circ 59'$ . The next problem is to adjust the intensity of the two recording beams to make them having the same intensity, thus having the maximum modulation depth. For the  $\theta'_1 = 10^\circ 31'$  and  $\theta'_2 = 27^\circ 59'$ , they have different transmissivity at the surface of the prism. It can be calculated according to the Maxwell equations.

$$R = \frac{\sin(i_1 - i'_1)}{\sin(i_1 + i'_1)} \quad (5.18)$$

Here  $i_1$  is the incident angle, and  $i'_1$  is the refraction angle. For this problem,  $i_1$  is  $\theta_1$  or  $\theta_2$ , and  $i'_1$  is the refraction angle of  $\theta_1$  or  $\theta_2$ . The calculation result is shown in Figure 4.17. There is a 3% difference in their surface transmissivity.

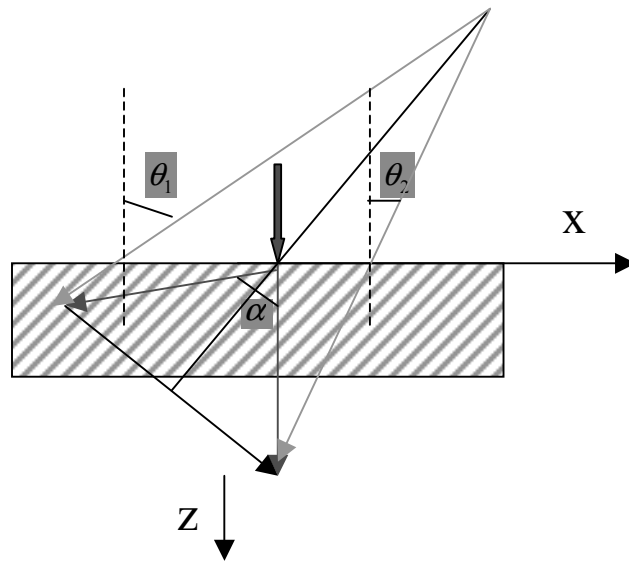


Figure 4.15 Schematic diagram for recording parameters calculation

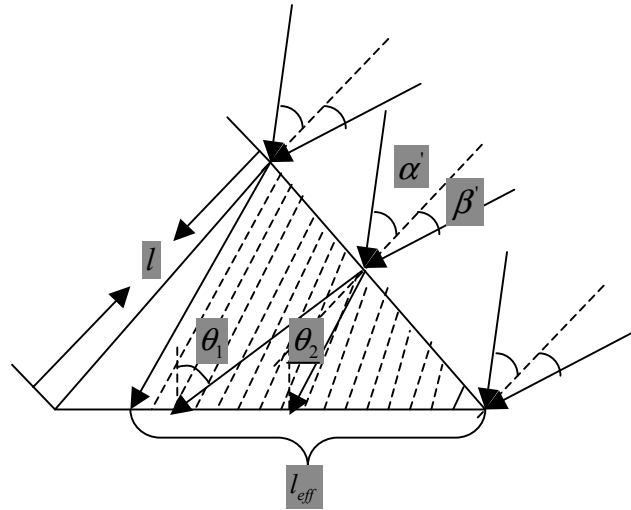


Figure 4.16 Schematic diagram for recording parameters calculation

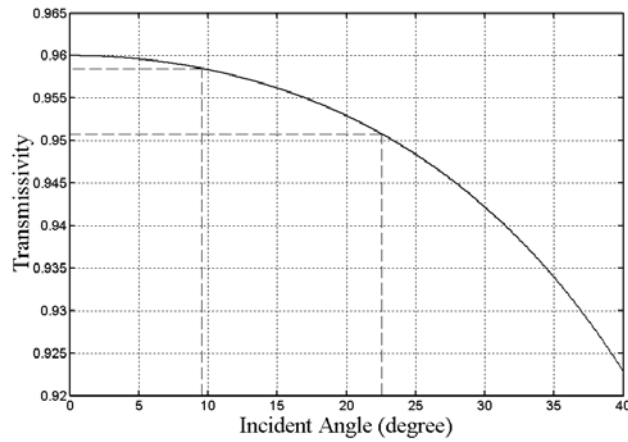


Figure 4.17 Transmissivity for different incident angle

### 4.3 Experiment results

The recording parameters need to be optimized first for recording the holographic gratings. The two most important parameters governing the recording process are the intensity of the recording beams and the exposure time. In the experiment, the exposure time is fixed at 20s and the intensity of the recording beams is varied. The maximum

output power from Verdi laser is 5W. The following power levels from the Verdi laser were used in the optimization process: 0.3W, 0.4W, 0.6W, 0.8W, 1W, 1.2W, 1.4W, 1.6W, and 2W. The power was measured at the recording area using a photo detector and the corresponding measurement results are 4.2mW, 5.85mW, 8.8mW, 11.92mW, 14.98mW, 18.21mW, 21.9mW, 25.7mW, and 33.4mW. The diameter of the photo detector is 1cm. So the calculated energy flux results are 5.35 mW/cm<sup>2</sup>, 7.45 mW/cm<sup>2</sup>, 11.21 mW/cm<sup>2</sup>, 15.19 mW/cm<sup>2</sup>, 19.08 mW/cm<sup>2</sup>, 23.2 mW/cm<sup>2</sup>, 27.9 mW/cm<sup>2</sup>, 32.9 mW/cm<sup>2</sup>, 42.55 mW/cm<sup>2</sup>. The Figure 4.18 shows the experimental results of optimization process. It is easy to see the maximum diffraction efficiency of ~83% is achieved at the energy flux of 19.08mW/cm<sup>2</sup>, after which the diffraction efficiency reaches a saturation-like point. This optimized energy flux is used in the subsequent holographic gratings recording.

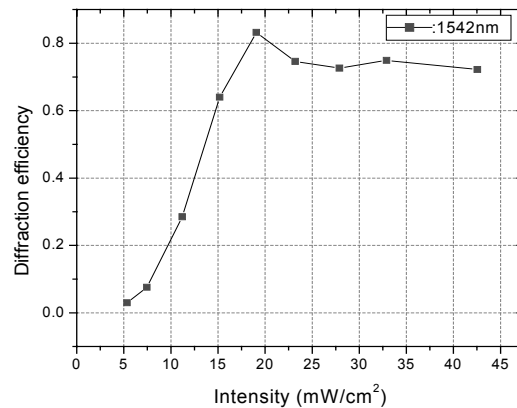


Figure 4.18 Holographic recording optimization results

The measured diffraction loss at different incident wavelength across a 10nm tuning range is shown in Figure 4.19.

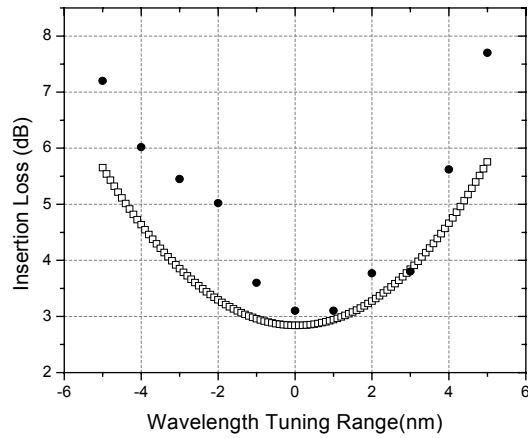


Figure 4.19 Insertion loss measurement results

To verify the dispersion ability of the fabricated devices, we made the following measurements to verify the dispersion of the devices. As shown in Figure 4.20, the distance between the input beam spot and the output beam spot is determined by

$$l = 2h \tan(\theta) \quad (4.19)$$

This distance is continuously measured with varied wavelength of the incident beam. The measurement results are shown in Figure 4.21 for the four different devices. The thinnest device has a thickness of 1.3mm and the thickness difference is about 1.4mm.

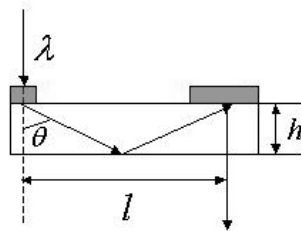


Figure 4.20 Illustration of dispersion measurement

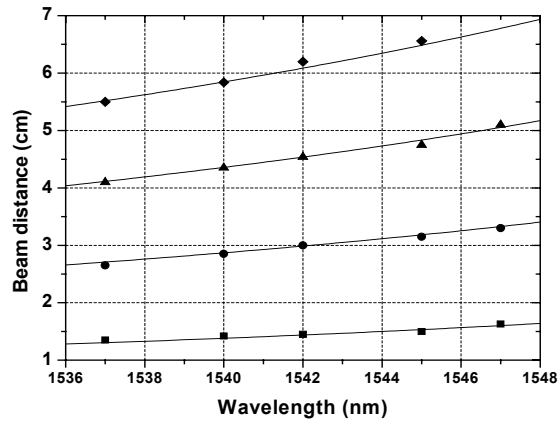


Figure 4.21 Dispersion measurement results

To accurately measure the time delay between devices, network analyzer is used to measure the phase vs. frequency relationship. Here phase refers to the phase difference between two devices. The measurement results are shown in Figure 4.22. The slope of the curve is the time delay between the devices. The 1537nm is chosen as reference zero point. The time delays corresponding to 1542nm and 1547nm are about 8ps and 17ps, respectively.

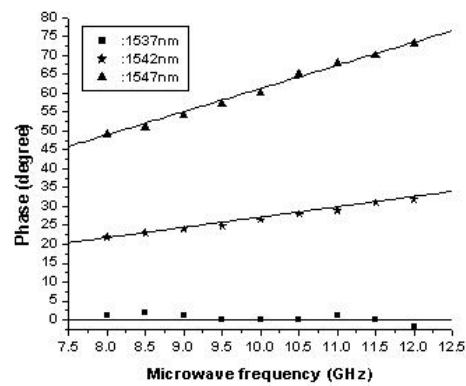


Figure 4.22 Time delay measurement results

## 4.4 Summary

In this chapter we presented volume-holographic-gratings based true-time delay devices including design, fabrication and design. We used right-angle prism aided structure to record large angle diffraction angle holographic gratings. The fabricated devices' dispersion and time delay formation ability is experimentally verified.

## 4.5 Reference

- 1:M. G. Moharam and T. K. Gaylord, Rigorous coupled-wave analysis of planar-grating diffraction, *Journal of the Optical Society of America*, 71, 811, 1981.
- 2:H. Kogelnik, Coupled wave theory for thick hologram gratings, *Bell Syst. Tech. J.*, 48, 2909, 1969.
- 3:Yevick and L. Thlen, Analysis of gratings by the beam-propagation method, *Journal of the Optical Society of America*, 72, 1084, 1982.
- 4:R. Petit, ed., *Electromagnetic theory of gratings*, Springer-Verlag, Berlin, 1980.
- 5:M. G. Moharam and T. K. Gaylord, Diffraction analysis of dielectric surface-relief gratings, *Journal of the Optical Society of America*, 72, 1385, 1982.
- 6:T. Tamir, H. C. Wang, and A. A. Oliner, Wave propagation in sinusoidally stratified dielectric media, *IEEE Transactions on Microwave Theory and Techniques*, 12, 323, 1964.
- 7:B. Lichtenberg and N. C. Gallagher, Numerical modeling of diffractive devices using the finite element method, *Optical Engineering*, 33, 3518, 1994.

- 8:M. G. Moharam and T. K. Gaylord, Rigorous coupled-wave analysis of grating diffraction E-mode polarization and losses, *Journal of the Optical Society of America*, 73, 451, 1983.
- 9:J. Goodman, *Introduction of Fourier Optics*, Second Edition, McGraw-Hill, Inc., New York, NY (1996).
- 10:J. Liu, Z. Fu, and R. T. Chen, Polarization sensitivity of photopolymer-based volume holograms for one-to-many surface normal optical interconnects, *Optical Engineering*, 37, 660, 1998.
- 11:C. Zhou, Z. Fu, M. Dobinovsky, J. I and R. T. Chen, Dispersion enhanced wavelength division multiplexing, *SPIE*, 3005, 144, 1997.
- 12:Gicherl Kim, Xuliang Han, and Ray T. Chen, "A method for rebroadcasting signals in an optical backplane bus system," *IEEE Journal of Lightwave Technology*, vol. 19, no. 7, pp. 959-965, July 2001.
- 13:A. M. Weber, W. K. Smothers, T. J. Trout, and D. J. Mickish, Hologram recording in DuPont's new photopolymer materials, *SPIE*, 1212, 14, 1990.
- 14:W. J. Gambogi, W. A. Gerstadt, S. R. Mackara, and A. M. Weber, Holographic transmission elements using improved photopolymer films, *SPIE*, 1555, 256, 1991.
- 15:R. T. Chen, S. Tang, M. M. Li, D. Gerald, and S. Natarajan, 1-to-12 surface normal three-dimensional optical interconnects, *Applied Physics Letters*, 63, 1883, 1993.

## **Chapter 5**

### **Semiconductor Optical Amplifier: Simulation and Measurement**

The ultra short carrier lifetime ( $\sim$ ps) makes the semiconductor optical amplifiers the suitable candidate for optical signal processing applications that include optical packet-switching nodes targeting optical routers, all-optical wavelength conversion, all-optical regeneration, mid-span spectral inversion [1,2,3,4,5,6,7]. A 2-dimension phased array antenna system was proposed and developed in combination of wavelength conversion using semiconductor optical amplifiers in this research project. This chapter will discuss the fundamental physical mechanism of the semiconductor optical amplifiers. The static and the dynamic models for semiconductor optical amplifiers are both presented. The simulation and measurement results will be shown in this chapter.

#### **5.1 Introduction**

Optical amplifiers have played a critical role in the telecommunications revolution starting in the early 1990s. Before the appearing of optical amplifiers, the optical communication links have to use electrical regeneration after 40~50Km' transmission. The electrical regeneration is complex and high cost. Everything has been changed since the appearing of optical amplifiers. For the first time, optical communication systems using inline amplifiers could operate over multiple fiber spans without expensive and complex electronic regeneration. "All optical network" (AON) is also made feasible with the appearance of the optical amplifiers. There are several

different optical amplifiers existing in the commercial telecommunication markets, such as Erbium-doped fiber amplifiers (EDFAs), Erbium-doped waveguide amplifiers (EDWAs), Raman amplifiers, and semiconductor optical amplifiers (SOAs). EDFAs have already been deployed in the commercial telecommunication systems for a number of few years. They have exhibited excellent performance in term of gain and noise figure in the ITU wavelength C-band (1530nm~1560nm). The basic structure of this type of amplifiers contains Erbium-doped fiber and high-power diode pump laser. EDFA operates via a three-energy level system. The population inversion within Erbium ions is formed when the Erbium-doped fiber is pumped by the pump laser at 980nm or 1480nm. The incoming weak signal is amplified by stimulated emission process when it travels through the Erbium-doped fiber. If the amplification bandwidth is beyond C-band, the conventional C-band EDFA could not provide sufficient gain or even attenuate the incoming signal. At this time other types of amplifier need to be used or other rare-earth ions need to be doped to extend the amplification bandwidth of the conventional C-band EDFA. An alternative choice is the Raman amplifiers. The Raman amplifiers have a pretty wide gain bandwidth (>40THz~300nm) which can cover amplification bandwidth from 1300nm to short wavelength S-band (1500-1530nm). The physical mechanism of this type of amplifiers is different from EDFA. No population inversion is formed within the Raman amplifiers. Raman gain arises from the energy transfer from one optical beam to another that is downshifted in frequency by the energy of an optical phonon. Raman amplifiers have a number of advantages. First, Raman gain exists in every fiber, which provides a cost-effective means of upgrading from the terminal ends. Second, the gain is non-resonant, which means that gain is available over the entire transparency region of

the fiber ranging from  $\sim 0.3 \mu\text{m}$  to  $2 \mu\text{m}$ . Third advantage is that the gain spectrum can be tailored by adjusting the pump wavelengths. Another advantage of Raman amplification is that the gain is relatively flat over a wide wavelength range. EDWA is a newly emerged type of amplifiers. Its working mechanism is the same as that of EDFA. Compared with EDFA, EDWA is fabricated based on integrated waveguide structures and not in a fiber form. So EDWA potentially can be integrated within the other optical active and passive components. EDWA has potential applications in the metropolitan area. SOAs have the longest research history among these types of amplifiers. But they are least ones to be mature enough to be deployed for the commercial applications. SOAs can be simply treated as a conventional semiconductor laser except the negligible reflectivity at the both end surfaces. A brief comparison between the four types of amplifiers is given in Table 5.1 [8,9].

	EDFA	EDWA	SOA	Raman	Units
Saturation output power	>15	>12	>13	NA	dBm
Gain	>24	>20	>25	20	dB
Bandwidth	30	30	50	300	nm
Carriers/populations lifetime	~ms	~ms	~ps	~fs	NA
NF	<6	<6	<8	4.2	dB
Gain flatness	<0.75	<0.75	<0.1	0.1	dB/nm
PDG	<0.3	<0.5	<0.5	Sensitive	dB p-p
Size	45x70x12	70x18x12	30x12.5x12.5	NA	mm
Power consumption	<1	<1	<5	NA	W
Other	Fully isolated with input and output detectors	Fully isolated with input and output detectors	Fully isolated packages available	Distributed structure	/

Table 5.1 Comparison among different types of amplifiers

There are two types of SOAs according to their behavior: F-P SOAs and traveling-wave (TW) SOAs. F-P SOAs can be typically viewed as the conventional laser diodes in which the incident optical signals are amplified while bouncing back and forth between the two end mirrors. F-P SOAs have higher gain than TW SOAs. But their drawback is that they only be able to amplify the certain discrete resonance wavelengths of the F-P cavities. TW SOAs have negligible surface reflectivity and thus any wavelength within the gain bandwidth can be amplified. The Figure 5.1 gives explicitly the main difference between the two types of SOAs. As only TW SOAs are used in our research work, all SOAs in the following paragraphs are referred to TW SOAs for simplification purpose.

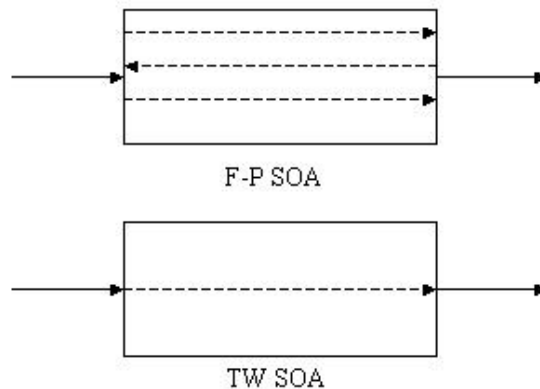


Figure 5.1 Illustration of difference between F-P SOA and TW SOA

The basic structure of SOAs is depicted in Figure 5.2. An embedded waveguide is used to confine the propagating signal within the gain medium and an external electrical current provides the energy source for the gain medium. Anti-reflection coatings at the

both end facets suppress the resonance effect of the cavity. The incoming optical signal will get single-pass amplification within the SOA cavity.

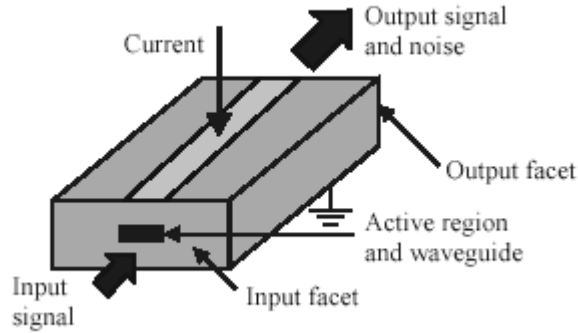


Figure 5.2 Schematic diagram of SOA

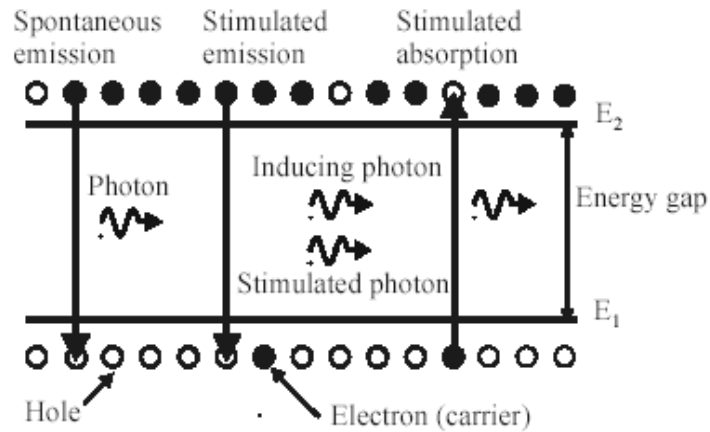


Figure 5.3 Schematic diagram of amplification process in SOA

An illustration of amplification process in SOA is shown in Figure 5.3. The externally injected carriers occupy energy states of the conduction band and valence band. When the sufficient carriers are injected into the active region, so-called carriers “inversion” will be formed. Once the carriers “inversion” is formed within energy band of SOA, it can

provide positive gain to the incident optical signal through stimulated emission process. Spontaneous emission is an added noise term to the amplified signal.

There are several parameters to judge the quality of a SOA. Some of them are already listed in Table 5.1.

#### (1) Bandwidth (3-dB)

The typical 3-dB gain bandwidth for a SOA is about 50nm at 1550nm region and about 30nm at 1330nm region. So the gain bandwidth of SOA is much broader than that of EDFAs in 1550nm region. The achievements have been made recently to extend the 3-dB gain bandwidth to more than 100nm using the advanced quantum dot structures [10,11]. With such wide bandwidth, SOAs can potentially cover all of S+C+L band.

#### (2) Current dependence of gain

For any wavelength within the gain bandwidth, the maximum gain that an optical signal can get is directly dependent on the injection current. This feature can be used for dynamic gain equalization purposes.

#### (3) Gain ripple

Due to the residual reflectivities of the SOA's both end facets, some dependence of the gain on small variation of the wavelength is always present. This is a detrimental effect as it makes the gain non-uniform when tuning the wavelength. Beside using anti-reflection coatings at the both end facets to suppress the gain ripple, the waveguide structure can be tilted to further suppress the reflections within SOA cavity. For the commercial products, the gain ripple can be made as small as 0.5dB [12].

#### (4) Polarization dependent gain (PDG)

The dependence of the gain on the polarization state of the input signal is in general an undesirable characteristic for any optical amplifiers. This dependence comes from the non-circular nature of the optical waveguide structure of SOA. For bulk SOAs, the square cross-section active waveguide or the ridge-waveguide structure can be used to reduce the PDG. For quantum well structures, the waveguide structure is usually very asymmetrical. But with appropriate strained tensile barriers, tensile strained quantum wells, and strain-balanced superlattices, this polarization dependence can be reduced to as low as 0.3dB [13,14,15].

#### (5) Small signal gain

Small signal gain of SOA is usually measured at very low input level ( $\sim 30$ dBm). At such low input power level, the gain saturation can be negligible and the input signal can experience a good linear amplification. For the input signal with a high power level, the gain saturation will be obvious within SOA. The input signal will get nonlinear amplification when propagating along SOA.

#### (6) 3-dB saturation output power

3-dB saturation output power is defined as the optical output power when the gain of SOA is 3-dB below the small signal gain. It is an important parameter to determine the optical power budget design as this power will be directly transmitted over the optical system.

#### (7) Noise figure (NF)

Noise figure is defined as ratio between the signal-to-noise ratio (SNR) at the input and at the output of the amplifier. The amplified spontaneous emission (ASE) process is

unavoidable in SOA. NF is a measure of how much ASE noise is added to the original signal by the amplification process.

We will examine these parameters in this chapter and the next chapter.

## 5.2: Static model for SOA

Some static models have been proposed for analyzing the performance of SOA [16,17,18,19,20]. Here we present a simplified numerical method and treat SOA as a distributed element, not a lumped one. The lumped model assumes an average carrier density along the cavity, thus eliminating the longitudinal-direction dependence of  $n$  and  $p$  in the rate equation. This is a good approximation when the input optical power is low since gain saturation is not severe along the longitudinal direction. But when the optical input power is large enough to cause significant gain saturation, the distributed model needs to be used to account for the inhomogeneous carrier density along the cavity. The presented model can be applied to both small signal and large signal cases. As indicated in Figure 3.4, the cavity of SOA has a length of  $L$  and it is divided into  $N$  sections.

Each section has a length of  $l = \frac{L}{N}$ . We assume that carrier density is a constant within

each section. The following rate equation is hold for each section,

$$\frac{dn_i}{dt} = j - R_i(n_i) - S_{ase,i} - S_{signal,i} \quad i = 1, 2, \dots, N \quad (5.1)$$

where  $n_i$  is the carrier density in  $i^{th}$  section,  $j$  is the current density injected into the active region,  $R(n_i)$  is the total recombination rate in  $i^{th}$  section,  $S_{ase,i}$  is the stimulation

rate due to the amplified spontaneous emission in  $i^{th}$  section,  $S_{signal,i}$  is the stimulation rate due to the amplified signal in  $i^{th}$  section.

$$j = \frac{I}{dwLe} \quad (5.2)$$

where  $I$  is the injection current,  $d$ ,  $w$ ,  $L$  are the thickness, width, and length of the active region, respectively,  $e$  is unit charge.

$$R_i(n_i) = an_i + bn_i^2 + cn_i^3 \quad (5.3)$$

where  $a$ ,  $b$ ,  $c$  are constants, and the corresponding linear, quadratic, and cubic terms account for nonradiative recombination by the material defects or surface effects, radiative recombination induced by spontaneous emission, and nonradiative Auger recombination, respectively.

$$S_{ase,i} = \frac{\beta \Gamma g_{m,i} R_i(n_i)}{g_i} \left\{ \frac{(e^{g_i l} - 1) [(1 - R_2)(1 + R_1 e^{g_i l}) + (1 - R_1)(1 + R_2 e^{g_i l})]}{g_i l (1 - R_1 R_2 e^{2g_i l})} - 2 \right\} \quad (5.4)$$

where  $\beta$  is spontaneous emission coupling coefficient (percentage of spontaneous emission coupled to the stimulated emission),  $\Gamma$  is confinement factor,  $R_1$  and  $R_2$  are the reflectivity at the input and output end facets. (3.4) is based on the derivation of [20].

$$g_{m,i}(n_i) = a_1(n_i - n_0) \quad (5.5)$$

where  $a_1$  is material gain constant,  $g_{m,i}$  is the material gain per unit length in  $i^{th}$  section.

$$g_i = \Gamma g_{m,i} - \alpha \quad (5.6)$$

where  $\alpha$  is total loss including in active and cladding region,  $g_i$  is the net gain per unit length in  $i^{th}$  section.

$$S_{signal,i} = \frac{g_{m,i}(n_i) I_{av,i}(n_i)}{h\nu} \quad (5.7)$$

where  $I_{av,i}$  is the average input signal intensity in  $i^{th}$  section.

$$I_{av,i} = I_{out,i-1} \frac{(1 + R_2 e^{g_i l})(e^{g_i l} - 1)(1 - R_1)}{g_i l (1 - \sqrt{R_1 R_2} e^{g_i l})^2} \quad (5.8)$$

where  $I_{out,i-1}$  is the optical signal intensity at the left end of  $i^{th}$  section. It is computed by the equation:

$$I_{out,j-1} = I_{in,j-1} e^{g_{j-1} l} \quad (5.9)$$

$I_{in,j-1}$  is the optical signal intensity at the left end of  $(i-1)^{th}$  section, we assume the optical signal intensity at the right end of  $(i-1)^{th}$  section is equal to the optical signal intensity at the left end of  $i^{th}$  section:  $I_{out,j-1} = I_{in,j}$ . Equation (5.8) is also based on the derivation of [20]. In this model, we neglect the wavelength dependent effect as we only care about 10~20nm bandwidth. This neglection is reasonable for our application.

For steady-state operation,  $\frac{dn_i}{dt} = 0$  (for  $i=1,2,\dots, N$ ). The computation steps are as following:

- (1) Calculate the carrier density  $n_1$  for a given optical input intensity
- (2) Calculate the gain for the first section
- (3) Calculate the optical input intensity for the second section
- (4) Calculate the carrier density  $n_2$  for the second section
- (5) Repeat the calculations until finishing the whole amplifier
- (6) Plot performance of amplifier

The typical parameters used for the simulation are listed in Table 5.2

### 5.3: Simulation results

#### 5.3.1 Carrier density distribution along the longitudinal direction of the cavity

Parameter	Description	Value	Unit
$d$	Active layer thickness	0.15	$\mu m$
$w$	Active layer width	1.2	$\mu m$
$L$	Active layer length	500	$\mu m$
$a$	Nonradiative recombination coefficient	$10^8$	$s^{-1}$
$b$	Bimolecular recombination coefficient	25	$\mu m^3 s^{-1}$
$c$	Auger recombination coefficient	$9.4 \times 10^{-5}$	$\mu m^6 s^{-1}$
$R_1$	Reflectivity at the left end facet	$5 \times 10^{-4}$	
$R_2$	Reflectivity at the right end facet	$5 \times 10^{-4}$	
$a_1$	Material gain coefficient	$2.5 \times 10^{-8}$	$\mu m^2$
$\Gamma$	Mode confinement coefficient	0.275	
$\alpha$	Loss coefficient	$2.5 \times 10^{-3}$	$\mu m^{-1}$
$\beta$	Spontaneous emission coupling factor	$10^{-4}$	
$n_0$	carrier density at threshold	$1.1 \times 10^6$	$\mu m^{-3}$
$e$	Unit charge	$1.6 \times 10^{-19}$	$c$

Table 5.2 Parameters used for the simulation

As the optical signal propagates along the SOA cavity, its intensity becomes larger and larger. At the same time, the optical signal will deplete more and more

“inverted” carriers. So the carrier density along the cavity will decrease along the cavity. The inhomogeneous carrier distribution along the cavity is needed to be considered especially when the high frequency signal is amplified. The Figure 5.4 gives the calculated carrier distribution along the longitudinal direction of SOA cavity. The solid curves are for an external injected current of 150mA and the dashed curves are for an external injected current of 250mA. We assume a 10% current injection efficiency.

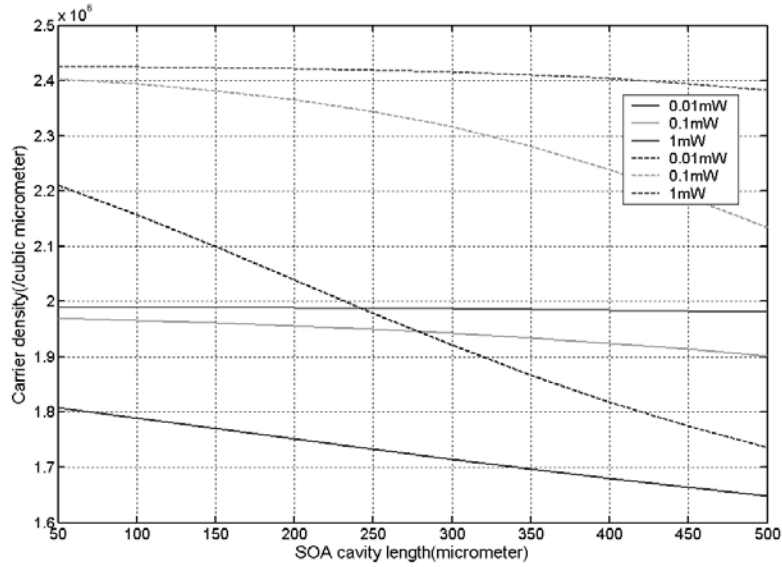


Figure 5.4 Carrier distribution along the longitudinal direction of SOA cavity

### 5.3.2 Gain for each divided section along the cavity

From the above calculated carrier density distribution along the cavity, the gain for each small section can be calculated according the gain equation:

$$G_i = e^{\Gamma[a_1(n_i - n_0) - \alpha]l / N} \quad (5.10)$$

Figure 5.5 illustrated the calculated gain in each small section along the cavity. As in the Figure 5.4, the solid curves are for an external injected current of 15mA and the dashed curves are for an external injected current of 30mA.

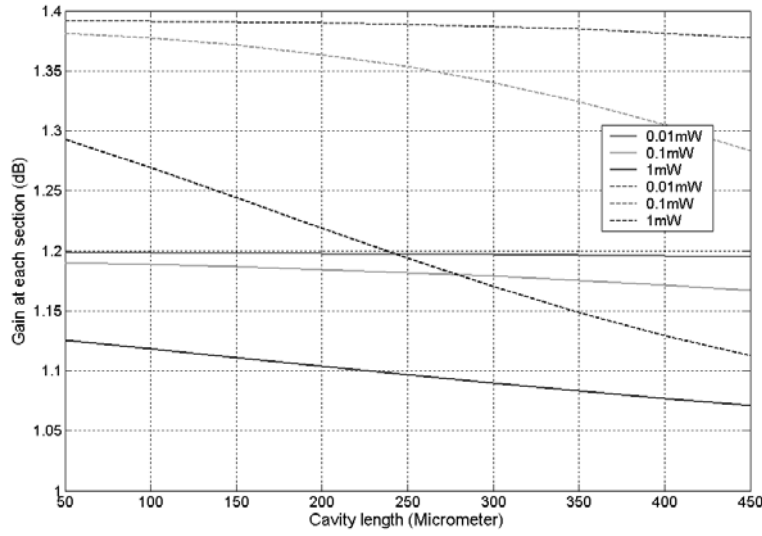


Figure 5.5 Gain in each small section along SOA cavity

### 5.3.3 Gain along cavity length

The gain along cavity length is of interested to us. For the total gain up to the  $i^{th}$  section, we need to multiply all the sections from  $1^{th}$  to  $i^{th}$  and the calculated results is shown in Figure 5.6. The solid curves are for an external injected current of 15mA and the dashed curves are for an external injected current of 30mA.

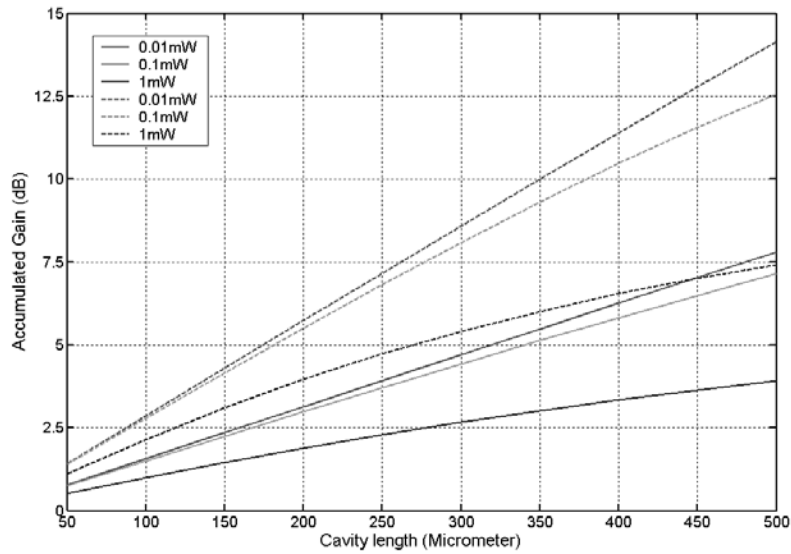


Figure 5.6 Total gain along SOA cavity

### 5.3.4 Gain vs. input (output) optical power

Due to the gain saturation, gain will decrease with the increasing input optical power. It is of particular interest to us as gain saturation will be used for wavelength conversion in the next chapter. Figure 5.6 shows the calculation results. The 3-dB saturation input and output power can be derived from the curves.

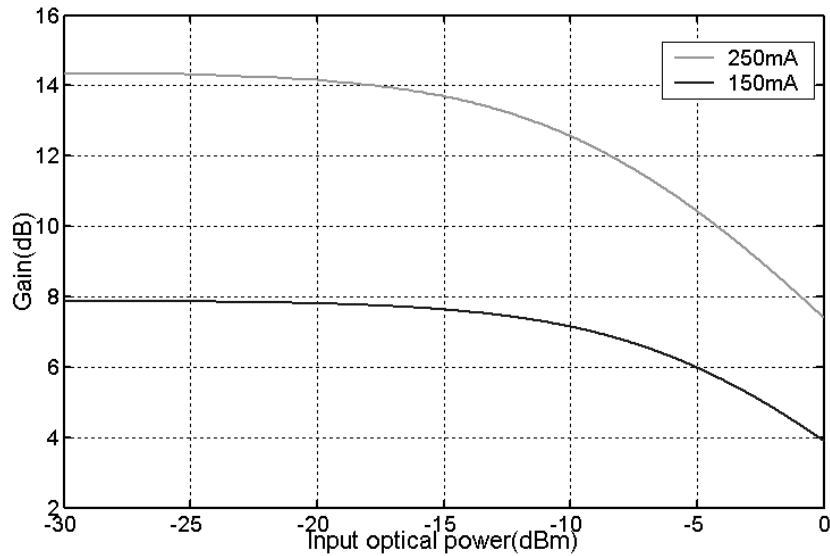


Figure 5.7 Gain vs. Input optical power

#### 5.4: Experimental results

Figure 5.8 is the measured ASE spectrum from SOA at a current of 150mA. The gain peak is at about 1530nm at this injection current. This gain peak will shift for the different injection current which is directly related to the band edge shrinkage effect. The heavier the injection current is, the shorter wavelength the gain peak will be.

The gain at different injection current for several wavelengths is measured as shown in Figure 5.9. As these wavelengths are closely spaced within the gain bandwidth of SOA, their gain difference is not obvious. The gain saturation appears in Figure 3.9 when the injection current is increased beyond a certain level which is due to the decreasing of quantum efficiency. The measured gain vs. input optical power curve is shown in Figure 5.10(a) and (b). Figure 5.10(a) is measured at 150mA and (b) is measured at 250mA.

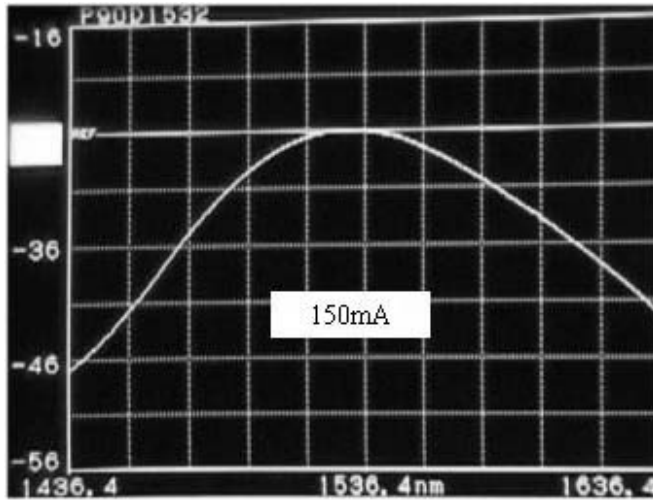


Figure 5.8 ASE spectrum from SOA

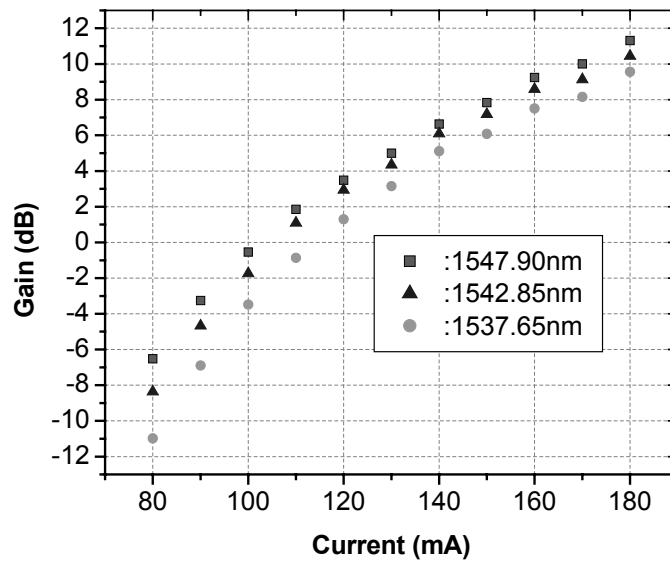


Figure 5.9 Gain vs. Injection current

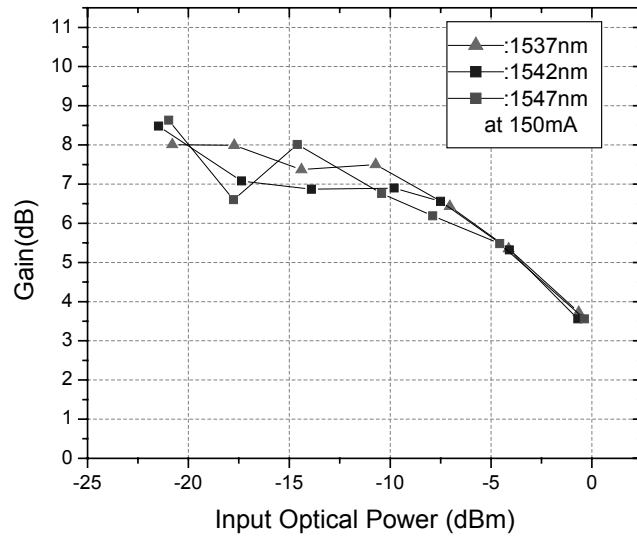


Figure 5.10(a) Gain vs. optical input power

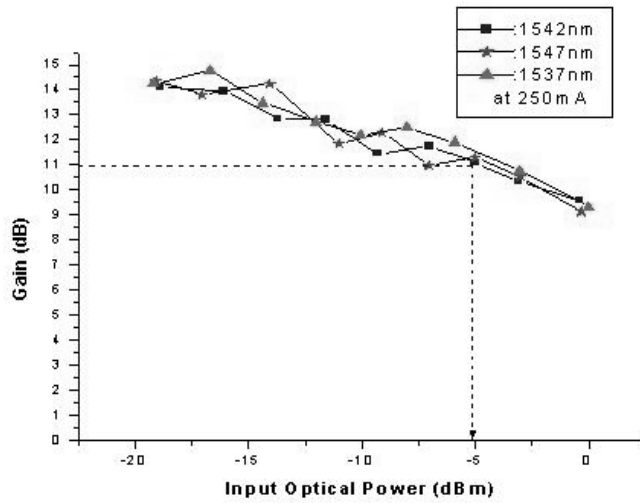


Figure 5.10(b) Gain vs. optical input power

## 5.5 Summary

In this chapter we give a simplified static model for SOA. The simulation is made according to this model and the calculation results are shown. We also showed the measurement results for SOA operating in static mode.

## 5.6 Reference

1:T. Durhuus, B. Mikkelsen, C. Joergensen, S. Lykke Danielsen and K. E. Stubkjaer, All optical wavelength conversion by semiconductor optical amplifiers, *J. Lightwave Technol.*, 14, 942, 1996.

2:S. Diez, C. Schmidt, R. Ludwig, H. G. Weber, K. Obermann, S. Kindt, I. Koltchanov, and K. Pertermann, Four-wave mixing in semiconductor optical amplifiers for frequency conversion and fast optical switching, *IEEE J. Sel. Topics in Quantum Electron.*, 3, 1131, 1997.

3:F. Kalman, L. G. Kazovsky and J. W. Goodman, Space division switches based on semiconductor optical amplifiers, *IEEE Photon. Technol. Lett.*, 4, 1048, 1992.

4:A. Ehrhardt, M. Eiselt, G. Grossopf, L. Kuller, R. Ludwig, W. Pieper, R. Schnabel, and H. G. Weber, Semiconductor optical amplifiers as optical switching gate, *J. Lightwave Technol.*, 11, 1287, 1993.

5:K. Vahala, R. Paiella and G. Hunziker, Ultrafast WDM logic, *IEEE J. Sel. Top. In Quantum Electron.*, 3, 698, 1997.

6:M. Gustavsson, A. Karlsson and L. Thylen, Travelling wave semiconductor laser amplifier detectors, *J. Lightwave Technol.*, 8, 610, 1990.

- 7:D. Zhou, K. Kang, I. Glesk, and P. R. Prucnal, An analysis of signal-to-noise ratio and design parameters of a terahertz optical asymmetric demultiplexer, *J. Lightwave Technol.*, 17, 298, 1999.
- 8:D. R. Zimmerman, L. H. Spiekman, Amplifiers for the masses: EDFA, EDWA, and SOA amplest for metro and access, *J. Lightwave Technol.*, 22, 63, 2004
- 9:M. N. Islam, Raman amplifiers for telecommunications, *IEEE J. Sel. Topics in Quantum Electron.*, 8, 548, 2002
- 10:E. U. Rafailov, P. Loza-Alvarez, W. Sibbett, G. S. Sokolovskii, D. A. Livshits, A. E. Zhukov, and V. M. Ustinov, Amplification of femtosecond pulses over by 18dB in a quantum-dot semiconductor optical amplifier, *IEEE Photonics Technol. Lett.*, 15, 1023, 2003.
- 11:P. Borri, S. Schneider, W. Langbein, U. Woggon, A. E. Zhukov, V. M. Ustinov, N. N. Ledentsov, Z. I. Alferov, D. Ouyang, and D. Bimber, Ultrafast carrier dynamics and dephasing in InAs quantum-dot amplifiers emitting near 1.3-micro-wavelength at room temperature, *Appl. Phys. Lett.*, 79, 2633, 2001.
- 12:From the JDSU SOA catalog which can be downloaded from [www.jdsu.com](http://www.jdsu.com)
- 13:M. Magari, M. Okamoto, and Y. Noguchi, 1.55micro polarization-insensitive high-gain tensile-strained-barrier MQW optical amplifier, *IEEE Photonic Technol. Lett.*, 3, 998, 1991.
- 14:M. Joma, H. Horikawa, C. Q. Xu, K. Yamada, Y. Katoh, and T. Kamijoh, Polarization insensitive semiconductor optical amplifiers with tensile strained InGaAsP/InGaAsP multiple quantum well structure, *Appl. Phys. Lett.*, 62, 121, 1993.

- 15:A. Godefroy, Al Le Corre, F. Clerot, S. Salaun, S. Loualiche, J. C. Simon, L. Henry, C. Vaudry, J. c. Keromnes, G. Joulie, and P. Lamouler, 1.55micro polarization-insensitive optical amplifier with strain-balanced superlattice active layer, IEEE photonic Technol. Lett., 7, 473, 1995.
- 16:L. Gillner, E. Goobar, L. Thylen, and M. Gustavsson, Semiconductor laser amplifier optimization: an analytical and experimental study, IEEE J. of Quantum Electron., 25, 1822, 1989.
- 17:M. J. Connelly, Wideband semiconductor optical amplifier steady-state numerical model, IEEE J. of Quantum Electron., 37, 439, 2001.
- 18:I. D. Henning, M. J. Adams, and J. V. Collins, Performance predictions from a new optical amplifier model, IEEE J. of Quantum Electron., 21, 609, 1985.
- 19:J. Wang, H. Olesen, and K. E. Stubkjaer, Recombination, gain and bandwidth characteristics of 1.3micro semiconductor laser amplifiers, J. of lightwave Technol., 5, 184, 1987.
- 20:M. J. Adams, J. V. Collins, and I. D. Henning, Analysis of semiconductor laser optical amplifiers, IEE Proceedings, 132, 58, 1985.

## Chapter 6

# Microwave Photonics System Analysis with Wavelength Conversion

This chapter discusses the performance of microwave photonics system in combination of wavelength conversion based on cross-gain-modulation in SOA. Frequency response, link gain, signal distortion and noise figure are the most important parameters to be considered in a microwave photonics system. We will start from the beam propagation equation and the rate equation to derive analytic formulas for above-mentioned parameters. The measurement results will also be shown in this chapter.

### 6.1 Introduction

Wavelength converters are important functional components in the future broadband all-optical networks. They are used to avoid wavelength blocking in optical cross connects (OXC) in WDM networks [1,2]. Wavelength converters will also increase the flexibility and capacity of a network using a fixed set of wavelengths [3,4]. They help to centralize network management and allow easier protection switching [5,6]. Several different schemes for wavelength conversion have been proposed and researched during the past few years. They can be broadly divided into categories: SOAs based approaches [7,8,9], and fibers based approaches [10]. There are three physical mechanisms for the SOAs based approaches: cross-gain-modulation (XGM), cross-phase-modulation (XPM), and four-wave-mixing (FWM). The fibers based approaches will not be touched here.

Interested readers can find more details from the above references. A simplified explanation is given to the XGM and XPM based schemes in the following paragraph.

The material gain spectrum of an SOA is homogeneously broadened which means that carrier density changes in the amplifier will affect all of the input signals. This carrier density changes can give rise to undesirable inter-channel crosstalk in multi-wavelength amplification. On the other hand, this crosstalk can be used to impose the information from one wavelength to other wavelengths. When the carrier density changes, the refractive index also changes. Two different wavelength conversion structures have been developed from the changes of the carrier density and the associated refractive index changes: cross-gain-modulation and cross-phase-modulation. Figure 6.1(a) illustrates the basic principle of cross-gain-modulation. A strong pump beam carrying data information modulates the carrier density and gain of an SOA due to the gain saturation. The modulated gain will modulate a CW probe beam at the same time. Thus the information on the pump beam can be converted to the CW probe beam. The Figure 6.1(b) illustrates the cross-phase-modulation based wavelength conversion. Two SOAs are placed in an interferometric configuration. The input pump signal  $\lambda_1$  enters only one arm of the structure, causing the changes of the refractive index in this arm. The CW beam  $\lambda_2$  is power splitted into two SOAs. One beam experiences the changes of refractive index and its phase gets modulated. The other beam passes SOA without phase modulation. Then the two beams at  $\lambda_2$  interfere with each other forming the converted output when they come out from the right end of SOAs. As a result, the converted output at  $\lambda_2$  will contain the information of the input signal  $\lambda_1$ .

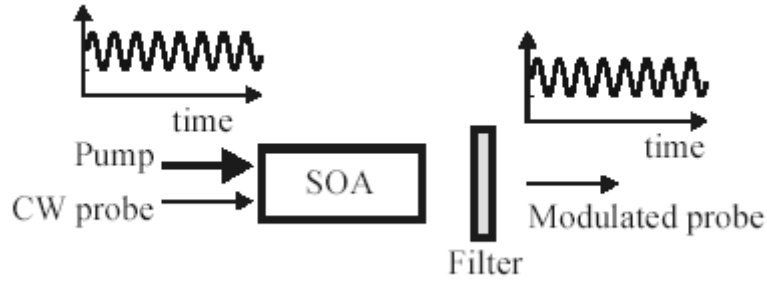


Figure 6.1(a) Cross-gain-modulation based wavelength conversion structure

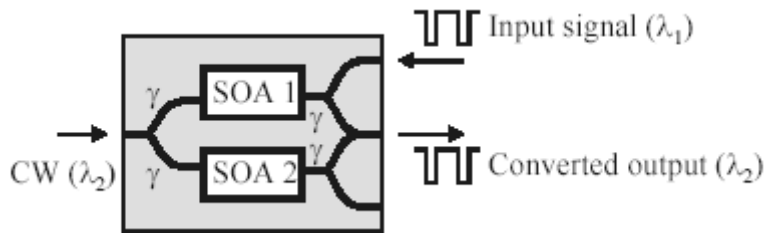


Figure 6.1(b) Cross-phase-modulation based wavelength conversion structure

In this work, we use cross-gain-modulation based wavelength conversion shown in Figure 6.1(a). This is because, from experiment point of view, the system structure is easier to implement compared with cross-phase-modulation based structure. We will focus on the cross-gain-modulation based wavelength conversion in the following analysis.

## 6.2 Analytic solutions of rate equation

The cross-gain-modulation in SOA is based on the mutual coupling between the carrier density and the incident beams. So the starting point for the analysis is still the two equations: beam propagation equation within SOA and the rate equation that are shown in (3.21) and (3.22). To analyze the distortion performance, we neglect the

spontaneous emission noise in the rate equation for simplification purpose. The wave guide loss is also neglected in the analysis. We have two input beams here: one is RF frequency modulated at  $\lambda_1$ , the other one is CW having no modulation at  $\lambda_2$ . The propagation equation and the rate equation can be written as [13]:

$$\frac{dP_i}{dz} = \Gamma a_1 (n - n_0) P_i \quad i = 1, 2 \quad (6.1)$$

$$\frac{dn}{dt} = \frac{I}{eV} - \frac{n}{\tau_s} - a_1 (n - n_0) \frac{P_1}{h\omega_0 A_{eff}} - a_1 (n - n_0) \frac{P_2}{h\omega_0 A_{eff}} \quad (6.2)$$

where  $\Gamma$  is the confinement factor,  $a_1$  is the material gain coefficient,  $n_0$  is the transparency carrier density,  $I$  is the injection current,  $V$  is the active region volume,  $\tau_s$  is the carrier lifetime,  $A_{eff}$  is the effective area of the waveguide and  $A_{eff} = \frac{P_{sat} \tau_{eff} a}{h\omega}$ .

The solution of (6.1) at the output end of SOA ( $z = l$ ) is

$$P_i(t, l) = P_i(t, 0) G = P_i(t, 0) \exp[\Gamma a_1 (N - n_0) l] \quad (6.3)$$

$$N = \int_0^l n(t, z') dz' \quad (6.4)$$

Take integration over  $l$  at both sides of (6.2) and using the equation (6.4), The following equation can be got

$$\frac{dN}{dt} = -\left(\frac{N - N_0}{\tau_{eff}}\right) - \frac{1}{\Gamma h\omega_0 A_{eff}} [P_1(t, 0) + P_2(t, 0)] \{G \exp[\Gamma a_1 (N - n_0) l] - 1\} \quad (6.5)$$

where  $N_0 = \frac{\tau_{eff} I l}{eV}$ ,  $P_1(t, 0) = \overline{P_{10}}(t, 0) + \Delta P_{10}(t, 0)$ ,  $P_2(t, 0) = \overline{P_{20}}(t, 0) + \Delta P_{20}(t, 0)$ . We assume a two-tone input  $\Delta P_{10}(t, 0) = \text{Re}(\Delta P_{10}(\omega_1) e^{j\omega_1 t}) + \text{Re}(\Delta P_{10}(\omega_2) e^{j\omega_2 t})$  at  $\lambda_1$ , and  $\Delta P_{20}(t, 0) = 0$  at  $\lambda_2$ . To solve the equation (6.5), a perturbation approach up to the third

order for solving the spatially integrated carrier density is used as in [12,13,14]. For two-tone input at  $\omega_1$  and  $\omega_2$  ( $\omega_1 < \omega_2$ ), the second order distortion frequencies will be at  $2\omega_1$ ,  $2\omega_2$ ,  $\omega_1 + \omega_2$ , and  $\omega_2 - \omega_1$ . The third order distortion frequencies will be at  $3\omega_1$ ,  $3\omega_2$ ,  $2\omega_1 + \omega_2$ ,  $2\omega_1 - \omega_2$ ,  $2\omega_2 + \omega_1$ ,  $2\omega_2 - \omega_1$ , among which we are only interested in the distortions at the frequencies of  $2\omega_1 - \omega_2$  and  $2\omega_2 - \omega_1$  because they are closest to the fundamental frequencies  $\omega_1$  and  $\omega_2$  and most probably they will lie in the bandwidth of the system. The other distortion frequencies lie well beyond the bandwidth of the systems and generally will not affect the performance of the systems.

We assume the following equations at the end of the output end of SOA:

$$N = \overline{N_0} + \sigma N_1 + \sigma N_2 + \sigma N_3 \quad (6.6)$$

$$\sigma N_1 = \text{Re}(\sigma N_1(\omega_1)e^{-j\omega_1 t}) + \text{Re}(\sigma N_1(\omega_2)e^{-j\omega_2 t}) \quad (6.7)$$

$$\begin{aligned} \sigma N_2 = & \text{Re}(\sigma N_2(2\omega_1)e^{-j2\omega_1 t}) + \text{Re}(\sigma N_2(2\omega_2)e^{-j2\omega_2 t}) + \text{Re}(\sigma N_2(\omega_1 + \omega_2)e^{-j(\omega_1 + \omega_2)t}) \\ & + \text{Re}(\sigma N_2(\omega_2 - \omega_1)e^{-j(\omega_2 - \omega_1)t}) \end{aligned} \quad (6.8)$$

$$\sigma N_3 = \text{Re}(\sigma N_3(2\omega_1 - \omega_2)e^{-j(2\omega_1 - \omega_2)t}) + \text{Re}(\sigma N_3(2\omega_2 - \omega_1)e^{-j(2\omega_2 - \omega_1)t}) \quad (6.9)$$

We can get the following results after some algebraic calculations,

$$0 = -(\overline{N_0} - N_0) - \frac{\overline{P_{10}}(t,0)}{\Gamma a_1 P_{sat}} [e^{\Gamma a_1 (\overline{N_0} - n_0 t)} - 1] - \frac{\overline{P_{20}}(t,0)}{\Gamma a_1 P_{sat}} [e^{\Gamma a_1 (\overline{N_0} - n_0 t)} - 1] \quad (6.10)$$

$$\sigma N_1(\omega_{1,2}) = -\frac{1}{\Gamma h \omega A_{eff}} \frac{(G-1)\Delta P_{10}(\omega_{1,2})}{-j\omega_{1,2} + \frac{1}{\tau_{eff}} + \frac{\overline{P_{10}}G}{P_{sat}\tau_{eff}} + \frac{\overline{P_{20}}G}{P_{sat}\tau_{eff}}} \quad (6.11)$$

$$\sigma N_2(2\omega_{1,2}) = -\frac{1}{\Gamma h \omega A_{eff}} \left[ \frac{-G \Gamma a_1 \Delta P_{10}(\omega_{1,2}) \sigma N_1(\omega_{1,2})}{-j\omega_{1,2} + \frac{1}{\tau_{eff}} + \frac{P_{10}G}{P_{sat} \tau_{eff}} + \frac{P_{20}G}{P_{sat} \tau_{eff}}} + \right. \\ \left. \frac{-\Gamma^2 a_1^2 G \sigma N_1^2(\omega_{a,2}) (\overline{P_{10}}(t,0) + \overline{P_{20}}(t,0))}{-j\omega_{1,2} + \frac{1}{\tau_{eff}} + \frac{P_{10}G}{P_{sat} \tau_{eff}} + \frac{P_{20}G}{P_{sat} \tau_{eff}}} \right] \quad (6.12)$$

$$\sigma N_2(\omega_2 \mp \omega_1) = -\frac{1}{\Gamma h \omega A_{eff}} \left[ \frac{-G \Gamma a_1 (\Delta P_{10}(\omega_2) \sigma N_1(\mp \omega_1) + \Delta P_{10}(\mp \omega_1) \sigma N_1(\omega_2))}{-j(\omega_2 \mp \omega_1) + \frac{1}{\tau_{eff}} + \frac{P_{10}G}{P_{sat} \tau_{eff}} + \frac{P_{20}G}{P_{sat} \tau_{eff}}} + \right. \\ \left. \frac{-2\Gamma^2 a_1^2 G (\overline{P_{10}}(t,0) + \overline{P_{20}}(t,0)) \sigma N(\omega_2) \sigma N(\mp \omega_1)}{-j(\omega_2 \mp \omega_1) + \frac{1}{\tau_{eff}} + \frac{P_{10}G}{P_{sat} \tau_{eff}} + \frac{P_{20}G}{P_{sat} \tau_{eff}}} \right] \quad (6.13)$$

$$\sigma N_3(2\omega_1 - \omega_2) = -\frac{1}{\Gamma h \omega A_{eff}} \left\{ \frac{G \Gamma a_1 [\Delta P_{10}(\omega_1) \sigma N_2(\omega_1 - \omega_2) + \Delta P_{10}(-\omega_2) \sigma N_2(2\omega_1)]}{-j(2\omega_1 - \omega_2) + \frac{1}{\tau_{eff}} + \frac{P_{10}G}{P_{sat} \tau_{eff}} + \frac{P_{20}G}{P_{sat} \tau_{eff}}} + \right. \\ \frac{\Gamma^2 a_1^2 G}{2} \frac{2\sigma N_1(\omega_1) \sigma N_1(-\omega_2) \Delta P_{10}(\omega_1) + \sigma N_1^2(2\omega_1) \Delta P_{10}(-\omega_2)}{-j(2\omega_1 - \omega_2) + \frac{1}{\tau_{eff}} + \frac{P_{10}G}{P_{sat} \tau_{eff}} + \frac{P_{20}G}{P_{sat} \tau_{eff}}} + \\ \frac{\Gamma^2 a_1^2}{2} G (\overline{P_{10}}(t,0) + \overline{P_{20}}(t,0)) \frac{2\sigma N_1(\omega_1) \sigma N_2(\omega_1 - \omega_2) + 2\sigma N_1(-\omega_2) \sigma N_2(2\omega_1)}{-j(2\omega_1 - \omega_2) + \frac{1}{\tau_{eff}} + \frac{P_{10}G}{P_{sat} \tau_{eff}} + \frac{P_{20}G}{P_{sat} \tau_{eff}}} + \\ \left. \frac{\Gamma^3 a_1^3}{2} G (\overline{P_{10}}(t,0) + \overline{P_{20}}(t,0)) \frac{\sigma N_1^2(\omega_1) \sigma N_1(-\omega_2)}{-j(2\omega_1 - \omega_2) + \frac{1}{\tau_{eff}} + \frac{P_{10}G}{P_{sat} \tau_{eff}} + \frac{P_{20}G}{P_{sat} \tau_{eff}}} \right\} \quad (6.14)$$

The equation for  $2\omega_2 - \omega_1$  can be readily derived from equation (6.14) by exchanging the positions of  $\omega_1$  and  $\omega_2$ . Equations from (6.10) to (6.14) are the basic results used to analyze the analog performance of a cross-gain-modulation based wavelength converter. Equation (6.10) is an expression for the steady state operation of SOA.

### 6.3 Experiment setup for wavelength conversion

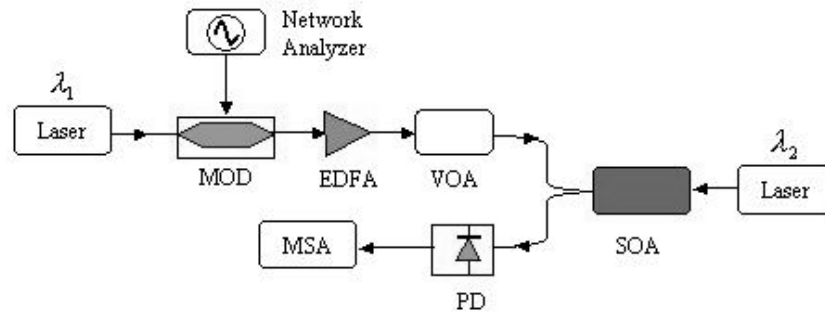


Figure 6.2 Schematic diagram for wavelength conversion

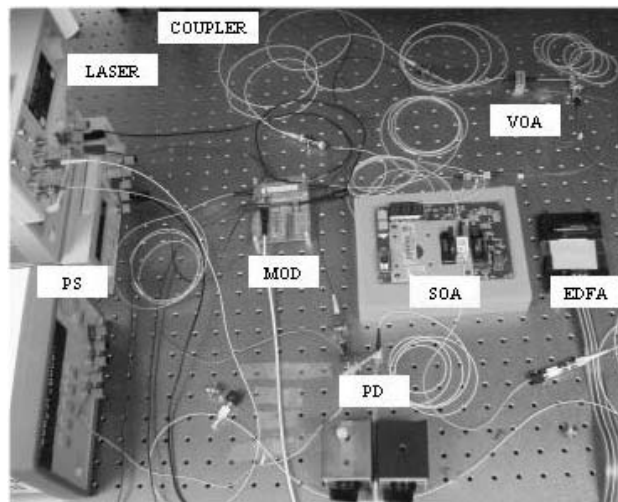


Figure 6.3 Experiment setup for wavelength conversion

Figure 6.2 is a schematic diagram of experiment setup for wavelength conversion. In the experiment counter-propagation scheme is used which will be free of using a tunable optical filter. Since the wavelength of the modulation signal ( $\sim 3\text{cm}$ ) is much larger than the SOA length ( $\sim 0.5\text{mm}$ ), co-propagation and counter-propagation have similar performance. So the analysis made here for the co-propagation scheme is

also hold for the counter-propagation scheme. If the wavelength of the modulation signal is comparable with the cavity length of SOA, the above analysis is not valid for analyzing counter-propagation scheme. The carrier dynamics across the whole cavity needs to be considered at this time. Figure 6.3 is a picture of the wavelength conversion subsystem.

#### 6.4 Frequency response and link gain analysis

From equations (6.10) and (6.11), the AC power value carried by the wavelength  $\lambda_2$  at the output end of SOA can be found to be

$$\Delta P_2(\omega_2) = - \frac{G(G-1)\Delta P_{10}(\omega_{1,2})\overline{P_{20}}}{-j\omega_{1,2} + \frac{1}{\tau_{eff}} + \frac{P_{10}G}{P_{sat}\tau_{eff}} + \frac{P_{20}G}{P_{sat}\tau_{eff}}} \frac{1}{P_{sat}\tau_{eff}} \quad (6.15)$$

The relationship between the AC output and the modulation frequency is usually called frequency response. The equation (6.15) can be defined as the normalized frequency response of the system once it is normalized by its maximum value. Figure 6.4 is the calculation and measurement results of the fundamental frequency response. We notice that measured curve has a peak response at around 1GHz and the simulation curve doesn't have it which is due to the neglecting of waveguide loss in the simulation. There is ~3dB response drops across X-band. The link gain is defined as the power difference between the output microwave electrical signal and the input microwave electrical signal. The link gain measurement is very important considering system optimization. Since the power of the input microwave signal to the modulator is fixed in the experiment, we only need to optimize the power of the output microwave signal. Figure 6.5 is the measured electrical signal power of the beam  $\lambda_2$  at the output end of SOA. This transfer function of

wavelength conversion shows the nonlinear characteristics with respect to the input pump power. This could be intuitively explained by the gain saturation phenomenon of SOA. As the gain is suppressed with the increasing pump power, the electrical signal carried by  $\lambda_2$  will increase first and then begin to decrease at certain input pump power. So the input pump power needs to be chosen carefully to optimize the output electrical power.

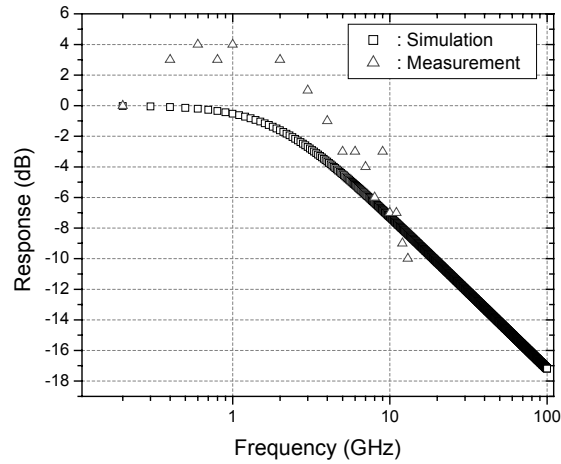


Figure 6.4 Frequency response measurement

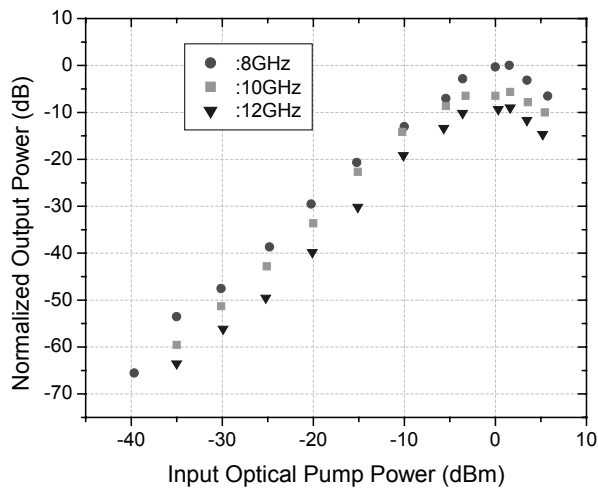


Figure 6.5 Transfer function of wavelength conversion

## 6.5 Distortion analysis

From equation (6.3) and considering the results (6.7), (6.8), and (6.9), we can get the following equations:

$$HD = \left| \frac{\Delta P_2(2\omega_i)}{\Delta P_2(\omega_i)} \right|^2 = \left| \frac{\sigma N_2(2\omega_i)}{\sigma N_1(\omega_i)} + \frac{\Gamma a_1^2}{2} \sigma N_1(\omega_i) \right| \quad (6.16)$$

$$IM_2 = \left| \frac{\Delta P_2(\omega_2 \mp \omega_1)}{\Delta P_2(\omega_2)} \right| = \left| \frac{\sigma N_2(\omega_2 \mp \omega_1)}{\sigma N_1(\omega_2)} + \Gamma a_1^2 \sigma N_1(\mp \omega_1) \right| \quad (6.17)$$

$$\begin{aligned} IM_3 &= \left| \frac{\Delta P_2(2\omega_i - \omega_j)}{\Delta P_2(\omega_i)} \right| \\ &= \left| \frac{\sigma N_3(2\omega_i - \omega_j)}{\sigma N_1(\omega_i)} + \frac{\Gamma a_1^2}{2} \sigma N(\omega_i) \sigma N_1(-\omega_j) + \Gamma a_2 \left[ \frac{\sigma N(2\omega_i) \sigma N_1(-\omega_j)}{\sigma N_1(\omega_i)} + \sigma N_2(\omega_i - \omega_j) \right] \right| \end{aligned} \quad (6.18)$$

In the experiment, the bias of the modulator should be optimized first to minimize the distortion before the optical signal enters into SOA. The modulator optimization results are shown in Figure 6.6. The transfer curve of the modulator is not linear, so the nonlinear transfer function will generate harmonic distortions to the optical signal. It is easy to see that the 2<sup>nd</sup> order harmonic distortion is huge at a bias of ~3.3V which corresponding the valley region of the modulation transfer function. The best bias is at ~4.3V which corresponding a -34dBc 2<sup>nd</sup> harmonic distortion. The asymmetry of the 2<sup>nd</sup> order distortion curve is due to the DC drifting of the modulator and the non-flat response of photodetector.

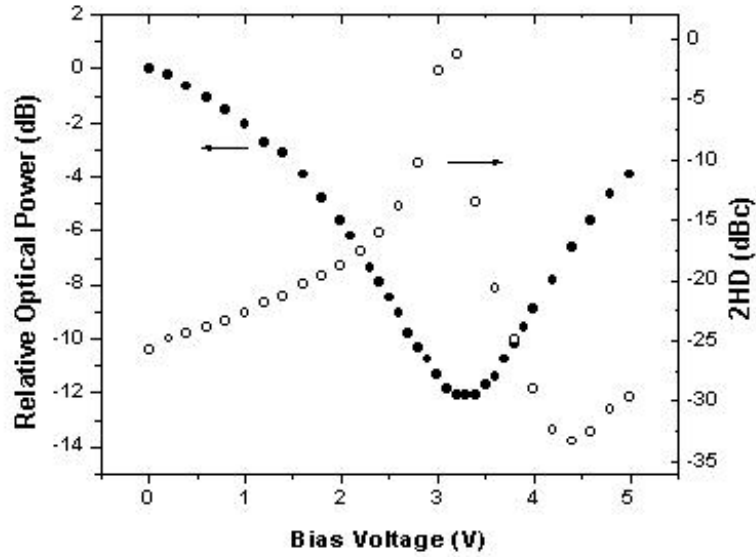


Figure 6.6 Modulator operating point optimization

Figure 6.7 is the simulated and measured results for the distortion at the 2<sup>nd</sup> harmonic frequency. The simulation is made according to equation (6.16).  $\overline{P}_{10} = 2mW$ ,  $\overline{P}_{20} = 3mW$ , and  $\tau_{eff} = 500ps$  are used for the simulation. We also measured the 2<sup>nd</sup> harmonic distortion free dynamic range at different input optical pump power for 8GHz and 12GHz, respectively. The measurement results at 8GHz and 12GHz are shown in fig 6.8(a) and (b), respectively. In fig. 6.8(a) and (b) the noise floor is about  $-130dBm$ . The linear curves are extrapolated to intersect the noise floor. Then the second harmonic distortion free dynamic range can be derived from the power difference at the two intersection points between the fundamental frequency and the second harmonic frequency. The corresponding 2<sup>nd</sup> harmonic distortion free dynamic range at 8GHz and 12GHz are shown in fig. 6.9(a) and (b), respectively. In the experiment we first measured the second harmonic distortion free dynamic range before wavelength conversion. This is

actually a measurement of optical modulator itself. The measured result is about 50.6dB-Hz<sup>1/2</sup> at 8GHz and this value is not sensitive to the input optical power. Then the second harmonic distortion free dynamic range was measured after wavelength conversion. The measurement was made at different input optical pump power: -5.88dBm, -1.93dBm and 0.43dBm. The corresponding second harmonic distortion free dynamic range was 45.6dB-Hz<sup>1/2</sup>, 48.7dB-Hz<sup>1/2</sup>, and 53.7dB-Hz<sup>1/2</sup>. From this measurement it's easy to see that increasing the input pump optical power helps to increase the second harmonic distortion free dynamic range, which is actually due to the increase of the wavelength conversion efficiency that is observed already in fig. 6.5. We expect 2<sup>nd</sup> harmonic distortion free dynamic range will decrease once the input optical pump power exceed the 2dBm which will cause the gain over-saturation of SOA and decrease of wavelength conversion efficiency. To further verify the above results, we make the same measurements but using a different microwave frequency: 12GHz. We measured the second harmonic distortion free dynamic range for modulator at 12GHz first and it was determined to be 56.75dB-Hz<sup>1/2</sup>. The corresponding results after wavelength conversion are 48.75dB-Hz<sup>1/2</sup> and 52.5dB-Hz<sup>1/2</sup>, respectively, for the input optical pump power at -1.93dBm and 0.43dBm. The second harmonic distortion free dynamic range will increase when increasing input optical pump power as shown in fig. 6.9(b), which agrees with the measurement results at 8GHz. One interesting thing needs to be pointed out is that the second harmonic distortion free dynamic range for the optical modulator at 12GHz is about 56.75dB-Hz<sup>1/2</sup> which is higher than that measured at 8GHz. This result seems not reasonable. Actually this is not surprising as it can be explained from the frequency response measurement of the optical modulator. The frequency response of the modulator

is shown in figs. 6.10(a), 6.10(b) and 6.10(c). Fig. 6.10(a) is made for the fundamental frequency and fig. 10(b) is for the second harmonic frequency. Fig. 6.10(c) shows the power difference between the fundamental frequency and the corresponding second harmonic frequency when the fundamental frequency was swept from 200MHz to 12GHz. The frequency response difference at 12GHz is about 42dB which is larger than that with a 36dB at 8GHz. This larger frequency response difference at high frequency makes the distance between the two intersection points at the noise level in Fig. 6.10(a) is larger than that in Fig. 6.10(b) for the modulator measurement. However, for the second harmonic distortion free dynamic range measurement after wavelength conversion, we didn't find an obvious difference between 8GHz and 12GHz since the response dropping across the X-band after wavelength conversion is not as large as that before wavelength conversion. To keep the designed system operating with a high second harmonic distortion free dynamic range, we have to keep the input optical pump power in 0~1dBm. However, as stated above, any further increase of this input optical pump power may decrease the second harmonic distortion free dynamic range due to the decrease of the output electrical power from the photodetector due to the gain over-saturation of SOA. Beside the measurements on 2<sup>nd</sup> FDR, we also tried to measurement SFDR of the system. We found the electrical powers at  $2\omega_1 - \omega_2$  and  $2\omega_2 - \omega_1$  are close to the noise limit of the instrument. So the further measurements were not being done.

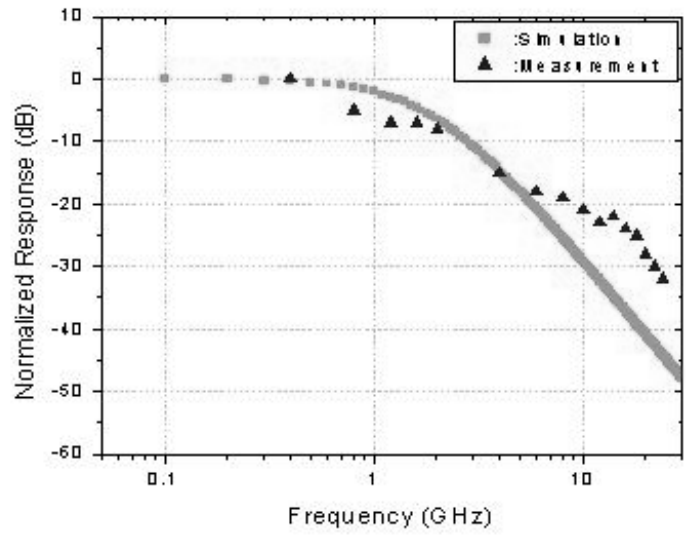


Figure 6.7 2HD simulation and measurement results

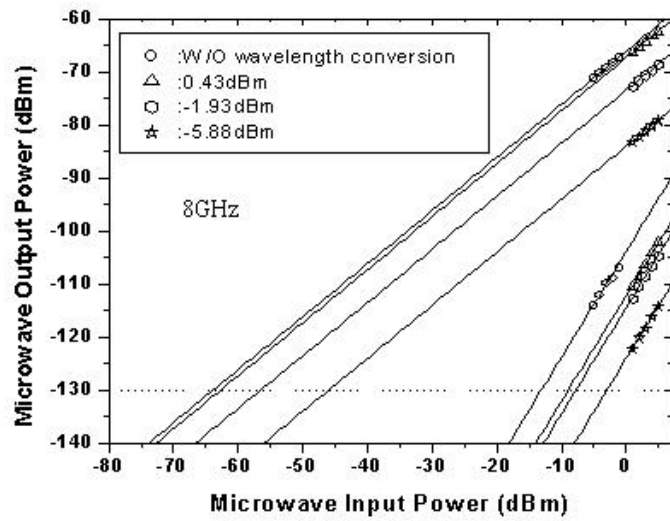


Figure 6.8(a) 2<sup>nd</sup> harmonic distortion free dynamic range measurements

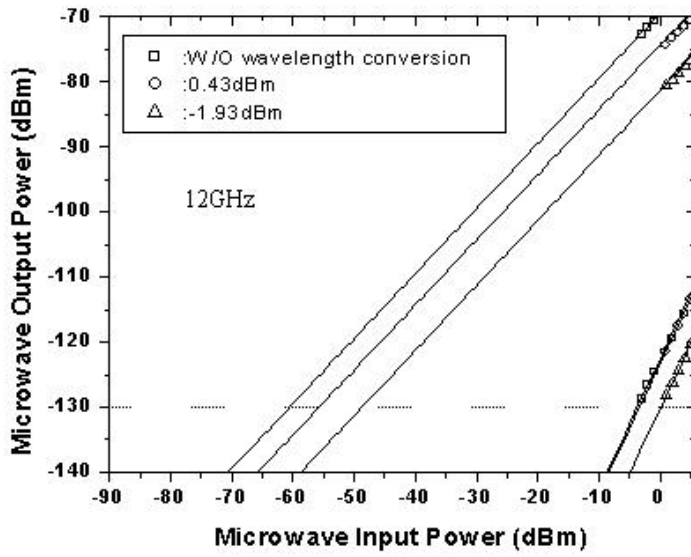


Figure 6.8(b) 2<sup>nd</sup> harmonic distortion free dynamic range measurements

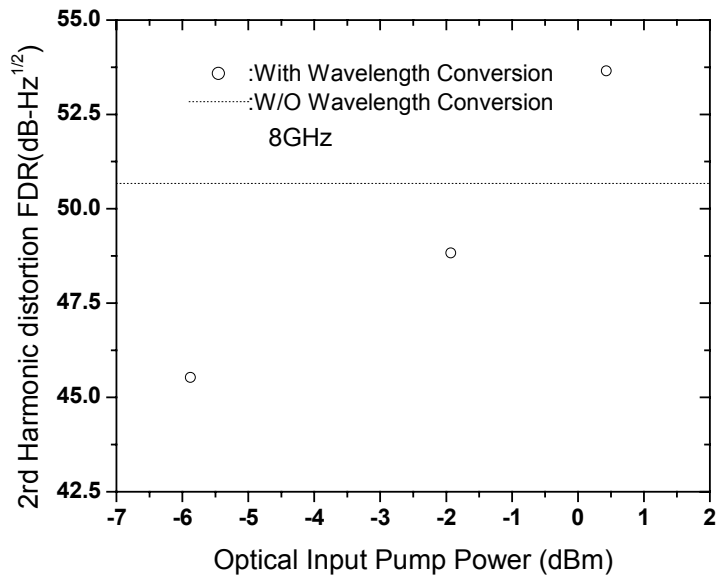


Figure 6.9(a) 2<sup>nd</sup> harmonic distortion free dynamic range vs. input optical pump power

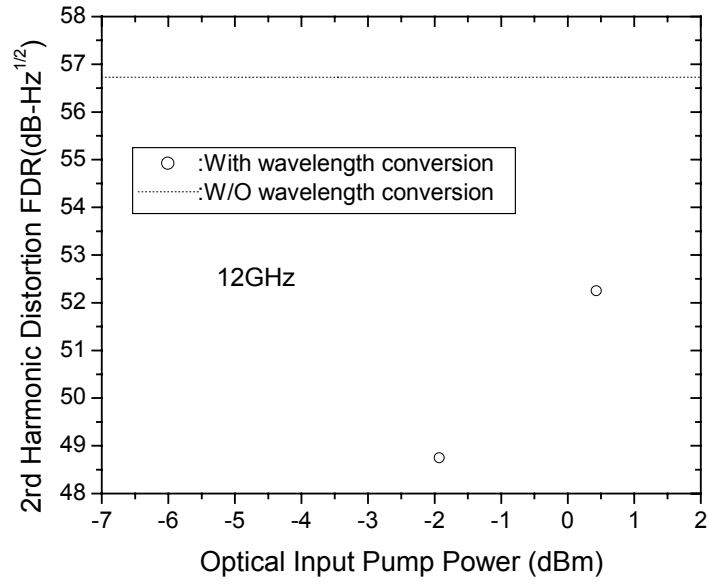


Figure 6.9(b) 2<sup>nd</sup> harmonic distortion free dynamic range vs. input optical pump power

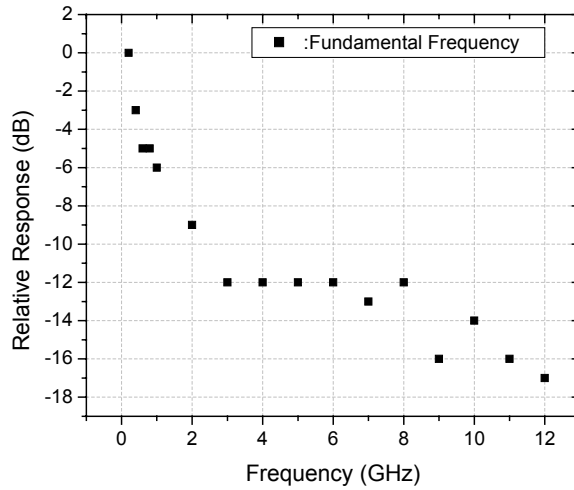


Fig. 6.10(a) Response measurement of optical modulator for the fundamental frequency

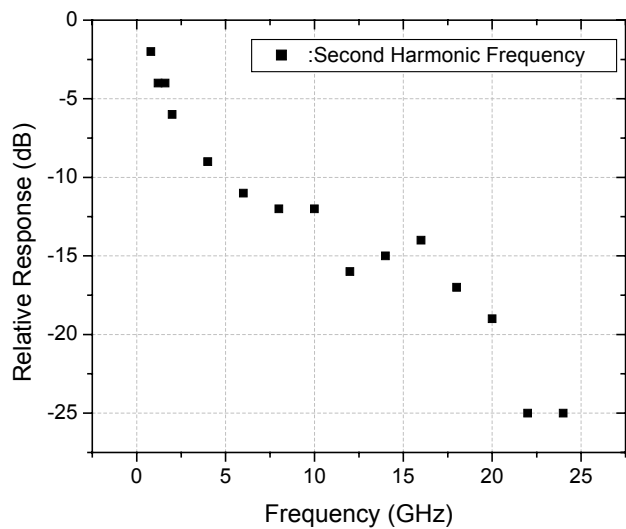


Fig. 6.10(b) Response measurement of optical modulator for the second harmonic frequency

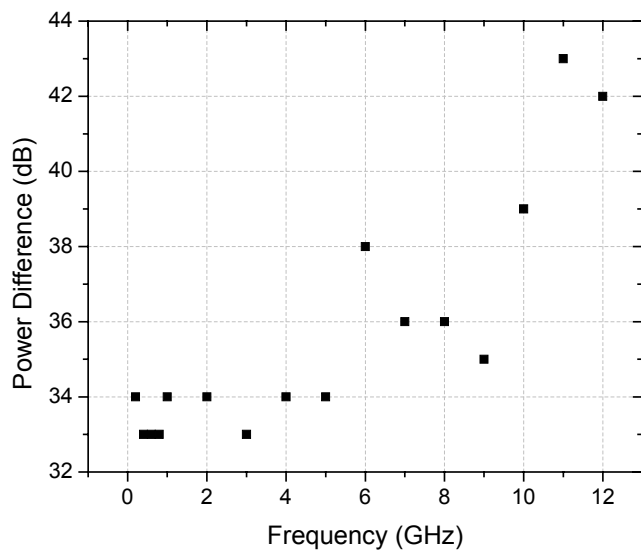


Fig. 6.10(c) Power difference between the fundamental frequency and the corresponding second harmonic frequency

## 6.6 Noise figure (NF) analysis

Noise figure is defined as the ratio between the amplifier input and output electrically equivalent SNR,

$$NF = \frac{(SNR)_{in}}{(SNR)_{out}} \quad (6.18)$$

For wavelength conversion, noise figure is used to represent two meanings: first: how much ASE noise generated within SOA is added to the desired optical signal, second: the signal conversion efficiency. There are four different noise terms in a photonics system with optical amplifiers. The first one is the shot noise,  $N_{shot}$ , which comes from the random generation of carriers within photo detector. The second noise is from the beating noise between the signal and the spontaneous emission,  $N_{s-sp}$ . Another noise is the beating noise between the spontaneous emission and the spontaneous emission,  $N_{sp-sp}$ . The thermal (or Johnson) noise,  $N_T$ , is the fourth noise term that comes from the output load (resistor). For a real system, the shot noise and the beating noise between the signal and the spontaneous emission will dominant the other two. So we will only consider the two dominant terms in the following analysis.

Following the similar steps in [16,17], the incident optical field at  $\lambda_1$  is taken as  $E(t) = E[1 + m \cos(\omega_m t)] \cos(\omega t) = \text{Re}(V(t))$  and  $V(t) = E[1 + m \cos(\omega_m t)] e^{j\omega t}$ .

The number of carriers generated will be proportional to  $\frac{1}{2} V(t) V^*(t)$ . The instantaneous current  $i(t)$  can be calculated from the generated carrier number. The signal power at  $\lambda_1$  is proportional to the mean-square of the AC part of  $i(t)$  and it is determined to be

$$S_{in} = \overline{i^2(t)} = 2\left(\frac{m_1 P_1 e \eta}{h \nu}\right)^2 \quad (6.19)$$

The noise term consists of only the shot noise term.

$$N_{in} = 2e^2 \frac{P_1}{h \nu} \Delta f \quad (6.20)$$

So the  $(SNR)_{in}$  can be written as following

$$(SNR)_{in} = \frac{S_{in}}{N_{in}} = \frac{m_1^2 P_1}{2h \nu \Delta f} \quad (6.21)$$

To calculate the output SNR, we need to calculate the electrical signal power generated by the probe beam at  $\lambda_2$ .

$$S_{in} = \overline{i^2(t)} = 2\left(\frac{m_2 G P_2 e \eta}{h \nu}\right)^2 \quad (6.22)$$

The noise term carried by the probe beam consists of two terms: shot noise and beating noise between the signal and spontaneous noise.

$$N_{out} = 2e^2 \frac{G P_2}{h \nu_2} \Delta f + 4e^2 G(G-1) \frac{P_2}{h \nu_2} n_{sp} \Delta f \quad (6.23)$$

So the  $(SNR)_{out}$  can be got as following

$$(SNR)_{out} = \frac{S_{out}}{N_{out}} = \frac{2\left(\frac{m_2 G P_2 e \eta}{h \nu_2}\right)^2}{4e^2 G(G-1) \frac{P_2}{h \nu_2} n_{sp} \Delta f + 2e^2 \Delta f \frac{G P_2}{h \nu_2}} \quad (6.24)$$

The noise figure can be finally written as

$$\begin{aligned}
NF &= \frac{(SNR)_{in}}{(SNR)_{out}} = \left( \frac{m_1 P_1}{v_1} \frac{v_2}{m_2 P_2} \right)^2 \frac{4e^2 (G-1) \frac{P_2}{h v_2} n_{sp} \Delta f + 2e^2 \Delta f \frac{G P_2}{h v_2}}{2e^2 \frac{P_1}{h v_1} \Delta f G} \\
&= \left( \frac{m_1^2 P_1 v_2}{m_2^2 P_2 v_1} \right) \left[ \frac{2(G-1)n_{sp} + 1}{G} \right] \\
&= \left( \frac{m_1^2 P_1 v_2}{m_2^2 P_2 v_1} \right) \left[ 2\left(1 - \frac{1}{G}\right)n_{sp} + \frac{1}{G} \right]
\end{aligned} \tag{6.25}$$

From equation (6.25) we can see that there are several parameters that could affect the value of NF: modulation depth of the input signal at  $\lambda_1$  and the output signal at  $\lambda_2$ , gain  $G$  of the amplifier, inversion factor  $n_{sp}$ , and the two frequencies  $v_1$  and  $v_2$ . The frequencies  $v_1$  and  $v_2$  can be negligible since the difference between them is very small. The modulation depth  $m_1^2 P_1$  of the input signal at  $\lambda_1$  and the modulation depth  $m_2^2 P_2$  of the output signal at  $\lambda_2$  can be derived from the equation (6.11). The  $m_2^2 P_2$  has the same form as the equation (6.15)

$$m_2^2 P_2 = \Delta P_2(\omega_2) = - \frac{G(G-1)\Delta P_{10}(\omega_{1,2})\overline{P_{20}}}{-j\omega_{1,2} + \frac{1}{\tau_{eff}} + \frac{P_{10}G}{P_{sat}\tau_{eff}} + \frac{P_{20}G}{P_{sat}\tau_{eff}}} \frac{1}{P_{sat}\tau_{eff}} \tag{6.26}$$

$m_1^2 P_1$  can be derived as following

$$m_1^2 P_1 = \Delta P_1(\omega_2) = G\Delta P_{10} - \frac{G(G-1)\Delta P_{10}(\omega_{1,2})\overline{P_{20}}}{-j\omega_{1,2} + \frac{1}{\tau_{eff}} + \frac{P_{10}G}{P_{sat}\tau_{eff}} + \frac{P_{20}G}{P_{sat}\tau_{eff}}} \frac{1}{P_{sat}\tau_{eff}}$$

For a realistic case,  $m_1^2 P_1 = m_2^2 P_2$ ,  $n_{sp} = 1$ , and  $G \gg 1$ , noise figure has a value of 2, etc. 3dB. Link noise figures approaching this limit have been demonstrated with a number of 4.2dB [17]. However, in general photoics link the noise figures are typically about 15~30dB. The measured results NF vs. bias current are shown in Figure 6.11. It can be

seen that higher bias current will improve the NF. It is to understand considering the gain increasing with bias current.

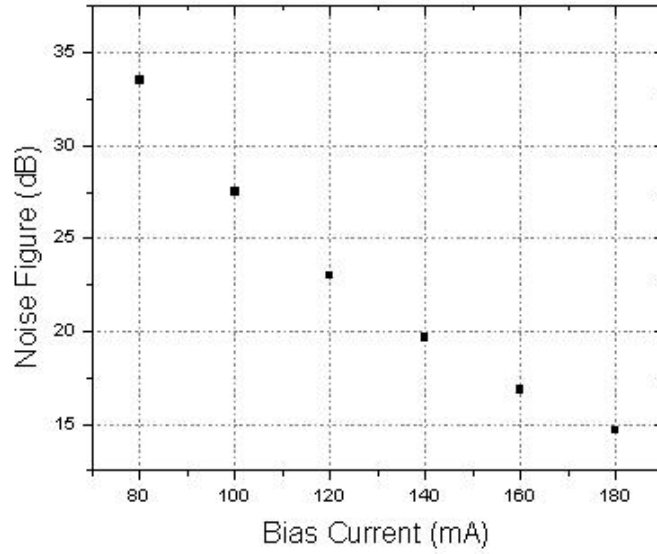


Figure 6.11 NF vs. bias current

Figure 6.12 shows NF vs. input pump power measurement results. When the power of the input pump signal is increased, NF will degrade which is due to the increased gain saturation of SOA.

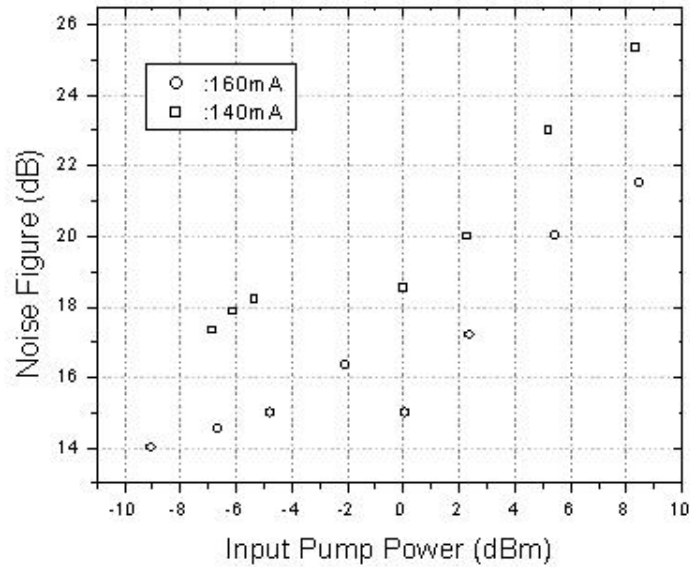


Figure 6.12 NF vs. input pump power

Based on the above measurements of frequency response, distortion performance and noise figure performance, and considering the power budget of the whole system, the input optical pump power at  $\lambda_1$  was chosen at  $\sim 2\text{dBm}$  which will give a balance among the received electrical power of conversion beam, distortion and noise figure. The input probe power is also chosen at  $\sim 3\text{dBm}$  to satisfy the power budget of the system.

## 6.7 Summary

In this chapter we present the analytic solutions for cross-gain-modulation based wavelength conversion. The frequency response, distortion performance and noise figure performance are analyzed and measured. The final optimized parameters for the whole system are also presented.

## 6.8 Reference

- 1: S. Okamoto and K. Sato, Optical path cross-connect systems for photonic transport networks, Proc. IEEE Global Telecommun. Conf., Nov. 474, 1993.
- 2: F. Derr, M. N. Huber, G. Kettler, and N. Thorweihe, Key issues of an optical FDM transport network, Proc. OFC'95, San Diego, CA, Feb., 1995.
- 3: C. A. Brackett, A. S. Acampora, J. Schweitzer, G. Tangonan, M. T. Smith, W. Lennon, K. C. Wang, R. H. Hobbs, Ascalable multiwavelength multihop optical network: A proposal for research on all-optical networks, J. Lightwave technol., 11,736, 1993.
- 4: N. Wauters and P. Demester, Wavelength requirements and survivability in WDM cross-connected networks, Proc. ECOC'94, 2, 589, 1994.
- 5:K. Sato, Transport network evolution with optical paths, Proc. ECOC'94, 2, 919, 1994.
- 6:K. Sato, S. Okamoto, and H. Hadama, Network performance and integrity enhancement with optical path layer technologies, J. Select. Areas Commun., 12, 159, 1994.
- 7:T. Durhuus, B. Fernier, P. Garabedian, F. Leblond, J. L. Lafragette, B. Mikkelsen, C. G. Joergensen, and K. E. Stubkjaer, High speed all-optical gating using two-section semiconductor optical amplifier structure, CLEO'92, 1992.
- 8:T. Durhuus, C. Joergensen, B. Mikkelsen, R. J. S. Pedersen, and K. E. Stubkjaer, All optical wavelength conversion by SOA's in a Mach-Zehnder configuration, IEEE Photonics Technol. Lett., 6, 53, 1994.
- 9:M. C. Tatham, 20nm optical wavelength conversion using nondegenerate four wave mixing, IEEE Photonics Technol. Lett., 5, 1303,1993.
- 10:K. Inoue, Polarization insensitive wavelength conversion using fiber four wave mixing with two orthogonal pumps at different frequencies, OFC'94, 1994.

- 11:Y. Suzuki and H. Toba, Recent research and development of all optical wavelength conversion devices, 1, 1, 2003.
- 12:K. Y. Lau, A. Yariv, Intermodulation distortion in a directly modulated semiconductor injection laser, 45, 1034, 1984.
- 13:D. Marcenac, and A. Mecozzi, Switches and frequency converters based on cross-gain modulation in semiconductor optical amplifiers, 9, 749, 1997.
- 14:J. Capmany, E. Peral, and D. Pastor, Formular for two-carrier intermodulation distortion in wavelength converted subcarrier multiplexed signals via cross gain modulation, 12, 278, 2000.
- 15:W. S. C. Chang, RF photonic technology in optical fiber links, Cambridge University Press, 2002.
- 16:Yariv, Optoelectronics, 4nd,, Saunders College Publishing, 1991
- 17:A. J. Seeds, Optical transmission of microwaves, Rev. Radio Sci., Oxford, U. K.: Oxford University Press, 325, 1996.
- 18:A. J. Seeds, Microwave photonics, IEEE Trans. Microwave Theory and Techniques, 50, 877, 2002.

## Chapter 7

# Phased Array Antenna System: Development and Measurement

This chapter describes the developed linear 1-dimension and 2-dimension phased array antenna system for X-band.

### 7.1 1D X-band Phased array antenna system

The system structure of the developed linear 4-element phased array antenna is given in Figure 7.1. A tunable laser (Santec MLS-2100) was intensity modulated by an SDL 10Gb/s intensity external modulator, in which the microwave signal was injected from a network analyzer (HP8510C). An Erbium-doped fiber amplifier (EDFA) was used to compensate the loss of the modulator (~9dB). The amplified optical signal passed through a 1x4 optical power splitter. After the splitter, the optical signals were injected into the four true-time-delay modules, respectively. After appropriate time delay, the four optical signals were converted to the corresponding electrical signals within four photo detectors. Four electrical amplifiers were used to amplify the electrical signals after the photo detectors. The four amplified electrical signals were fed to four X-band phased-array antenna elements. A standard horn antenna is used to receive the radiation signal from the transmitting side. The horn antenna is connected to a HP microwave spectrum analyzer (8563E) that can measure the power of the received signal. The radiation pattern of the phased array antenna system can be analyzed using the measured received signal

power. The true-time delay between any two modules can be derived from the measured phase difference vs. microwave frequency using the network analyzer.

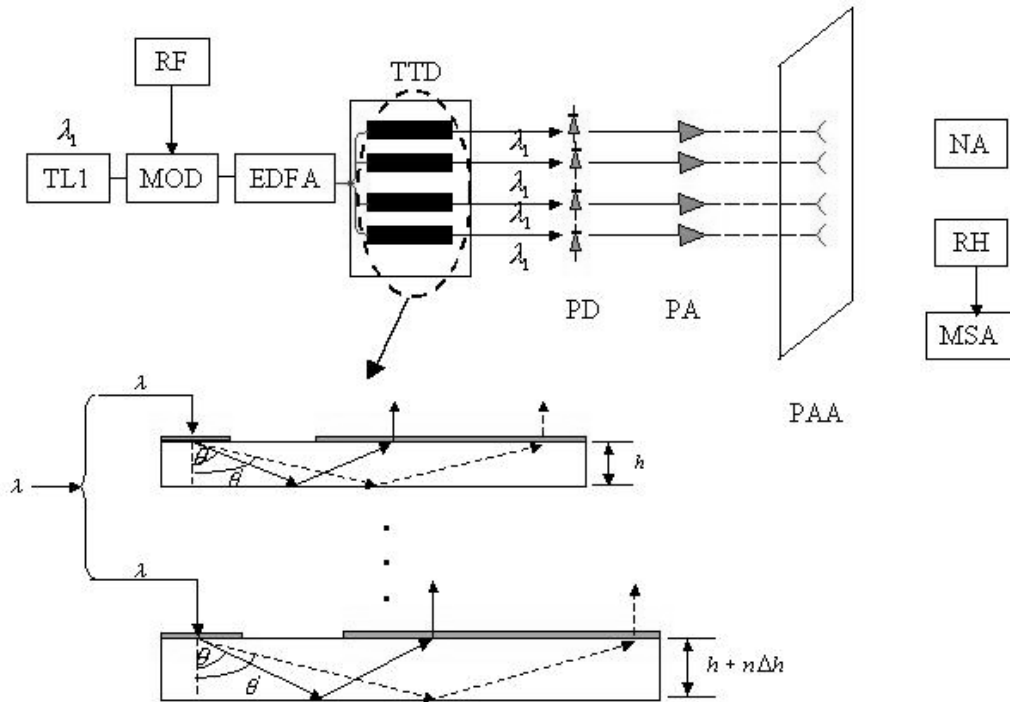
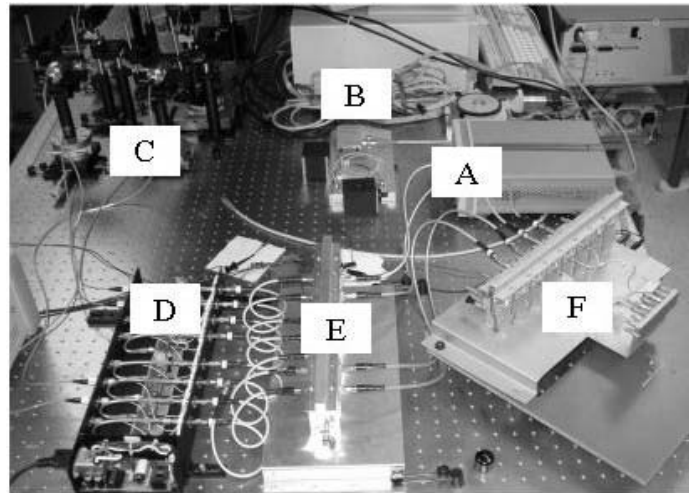


Figure 7.1 Schematic of the system experiment setup. Inset is the true-time delay formation structure. TL: tunable laser, MOD: modulator, EDFA: Erbium-doped fiber amplifier, TTD: true-time delay modules, PD: photo detector, PA: post amplifier, PAA: phased array antenna, NA: network analyzer, RH: receiving horn antenna, MSA: microwave spectrum analyzer.

Figure 7.2 is a photo of the developed linear 4-element phased array antenna system. This 4-element phased array antenna system was designed for microwave X-band (8-12.5GHz) or higher frequencies. Figure 7.3 shows the antenna array with standard patch elements and the receiving horn used in the experiment. The element spacing is 1.3cm that is less than the half wavelength of its radiation wavelength in order to avoid

grating lobes (will see in the next paragraph). Figure 7.4(a) shows the reflection coefficient  $S_{11}$  characteristics of four antenna elements. Figure 7.4(b) is the measured results of corresponding SWR. It can be seen from SWR that these antenna elements work very good at about 9GHz and 10GHz. From here it also can be seen the 1.3cm element spacing is shorter than the half wavelength at 9GHz(1.61cm) or 10GHz(1.5cm), which is free from the grating lobes phenomenon.



A: Laser	D: Photodetectors
B: Modulator	E: Amplifiers
C: Delay modules	F: Antenna head

Figure 7.2 Linear 4-element phased array antenna system photo

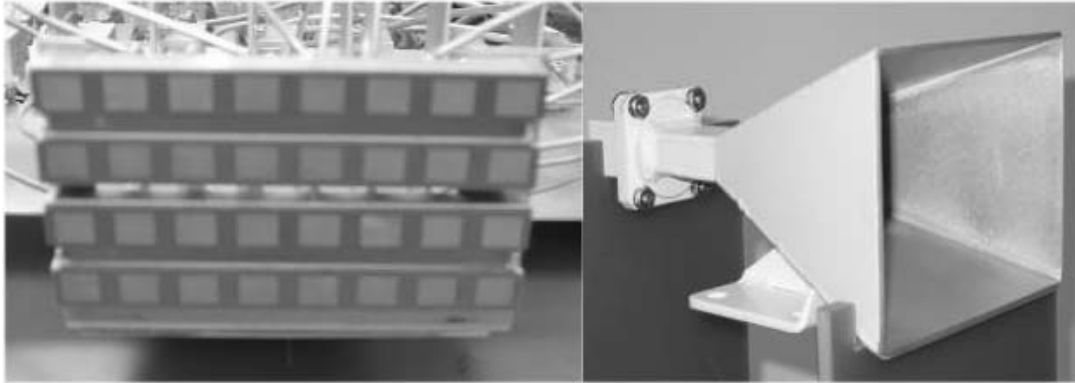


Figure 7.3 Picture of patch antenna array and the receiving horn

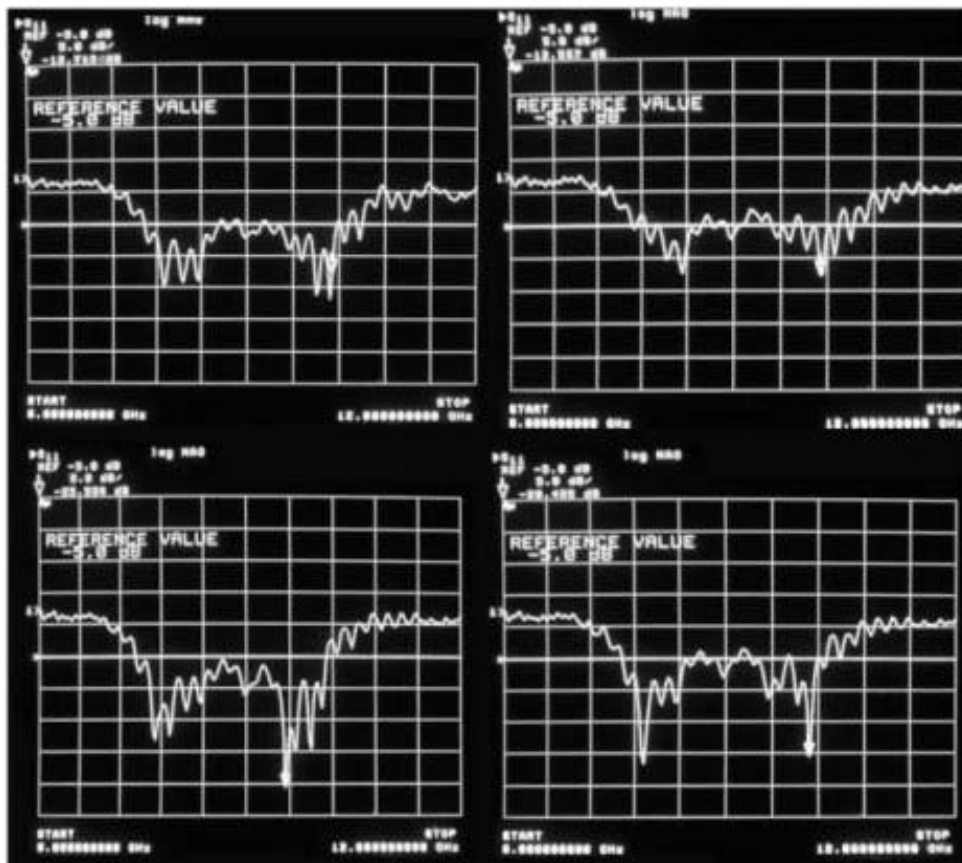


Figure 7.4(a) Measured reflection coefficient  $S_{11}$  of four antenna elements (scale 5dB/)

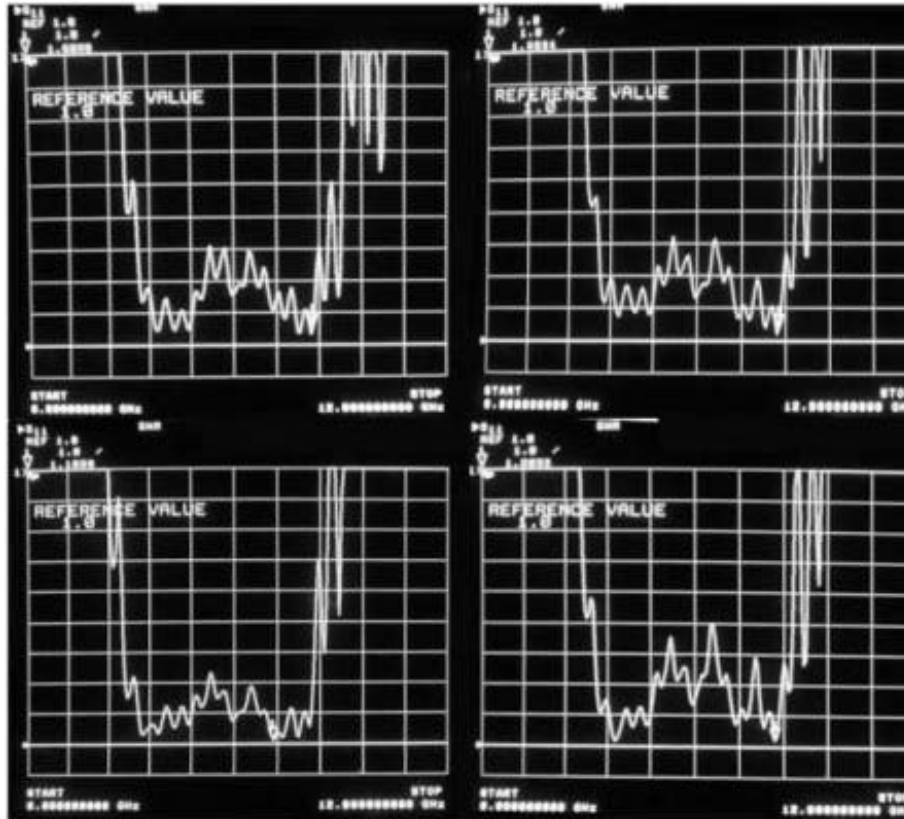


Figure 7.4(b) Measured SWR of four antenna elements (scale 1dB/ )

The structure and the size of the receiving horn is shown in Figure 7.5(a) and Table 7.1. The gain measurement is shown in Figure 7.5(b).

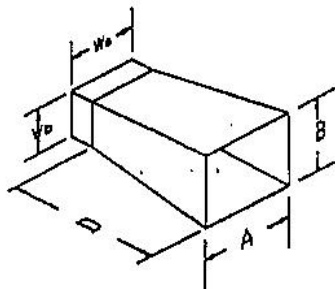


Figure 7.5(a) Structure of the receiving standard gain horn

Dimensions (inch)	
A	4.0
B	3.0
$w_a$	0.9
$w_b$	0.4
D	4.5

Table 7.1 Size parameters for the receiving gain horn

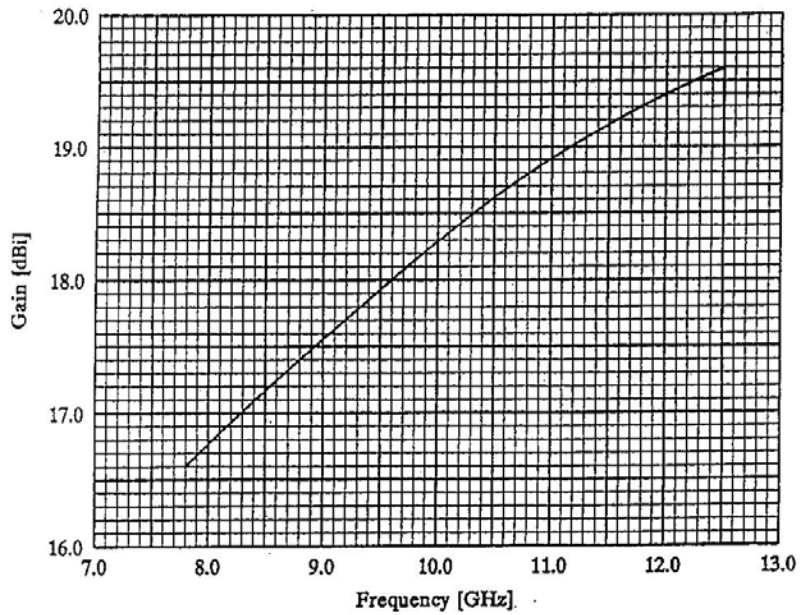


Figure 7.5(b) Measured gain of standard gain horn

Both the amplitude and the phase of each individual delay element will affect the final radiation pattern. Maintaining a uniform optical power across the four branches is important to get a good radiation pattern. The loss measurement of the four devices

with different thickness was shown in Figure 7.6. Ideally, we want the four curves matches with each other exactly. Unfortunately, the power non-uniformity of the four devices is still observed from the measurements. Beside this problem, the measured results for each device are not smooth and some ripples exist. We believe one of the reasons to explain the two problems is the index of the photo polymer material is not homogeneously distributed. If the index is not homogeneously distributed, it will perturb the recorded grating within the material and eventually perturb the diffraction efficiency of the devices. Other possible reasons should be traced to the recording process. Some recording noises due to the multiple-reflections exist within the recording prism which is difficult to get ride of completely. Such multiple-reflections will affect the recorded grating performance. We are still working on how to make the power uniformity as best as we can. Beside the factors from the devices, difference in quantum efficiency for the photo detectors still exists. Considering these factors, the power of the electrical signals after photo detectors can be adjusted by gain-tunable photo detectors. This tunable-gain is achieved by changing the bias of the photo detectors. Figure 7.7 shows the output power from the four photo detectors with sweeping frequency from 8 to 12GHz measured by network analyzer. The optical wavelength is 1537nm in the system. The initial phase uniformity was achieved by using the electrical phase trimmers. The measured phase difference vs. modulation frequency curves at different wavelengths was shown in Figure 7.8. The time delay between the delay devices can be derived from the slope of each curve. The wavelength at 1537nm was chosen as a reference for zero time delay. By tuning wavelength from 1537nm to 1547nm, the different time delay can be achieved

from 0ps to 17ps. The linear phase difference vs. frequency curve verifies the wide bandwidth capability of the system.

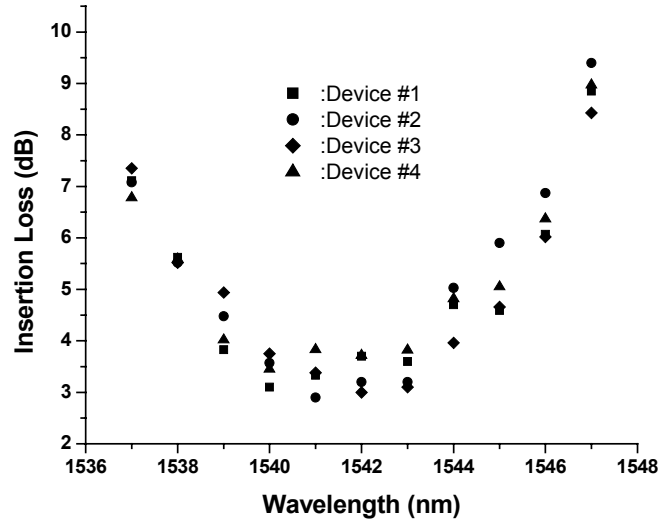


Figure 7.6 Insertion loss measurement

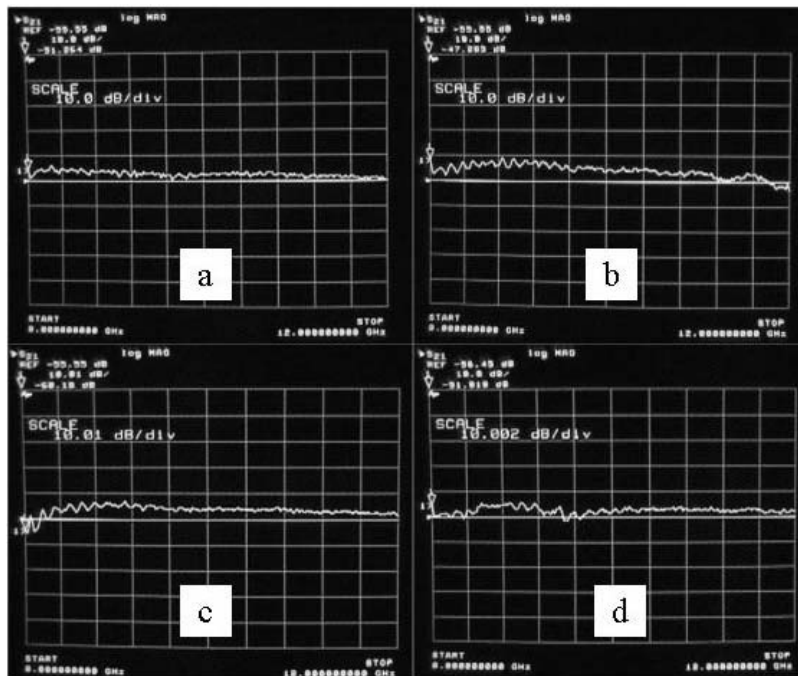


Figure 7.7 Measured  $S_{12}$  after photo detectors (scale 10dB/)

The radiation patterns of four elements were measured at two different frequencies to verify the wide bandwidth of the wavelength-controlled phased-array antenna system. The measured results are shown in Figure 7.9(a) and (b). Figure 7.9(a) corresponds to the measurement at  $\lambda = 1537nm$  with zero time delay between the delay modules. Figure 7.9(b) corresponds to the measurement at  $\lambda = 1547nm$  with a scanning angle of  $23^\circ$ . For each wavelength, the patterns were measured at two different frequency points, 9GHz and 10GHz. As expected, the measurement shows negligible beam squint effect in the developed system.

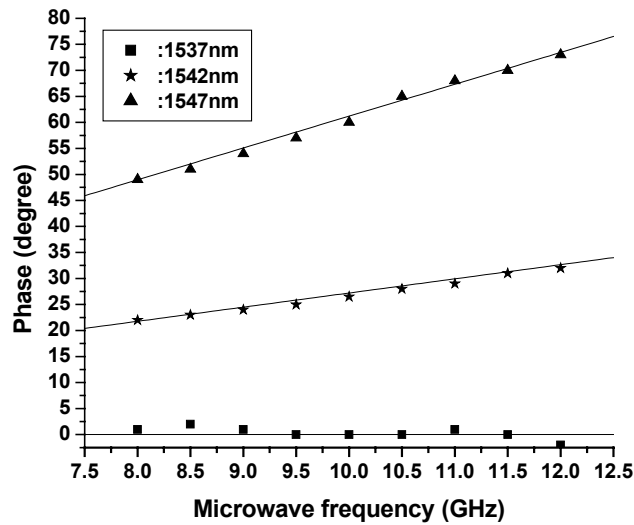


Figure 7.8 Measured phase difference vs. frequency

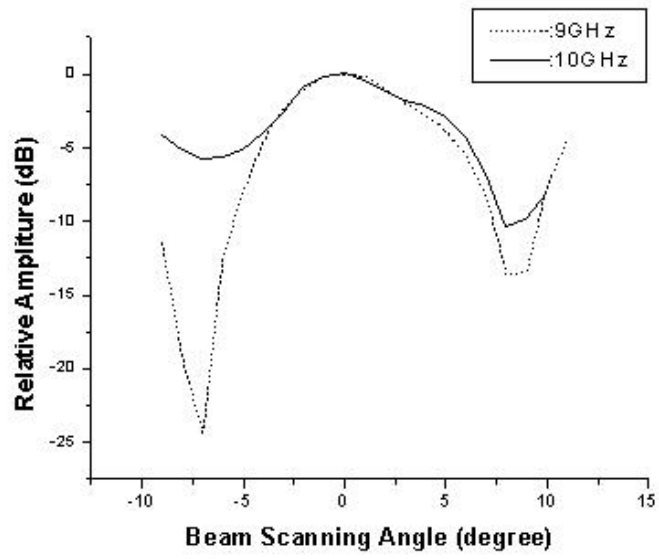


Figure 7.9 (a) Measured 4-element linear array radiation pattern

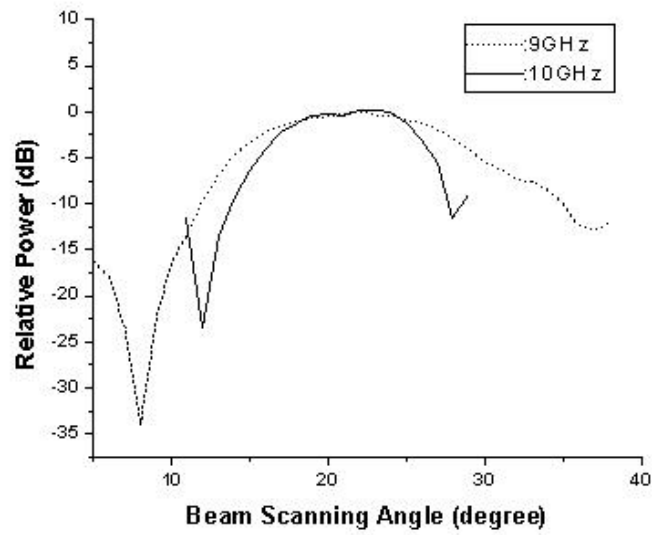


Figure 7.9 (b) Measured 4-element linear array radiation pattern

## 7.2 2D X-band Phased array antenna system

The schematic illustration of the developed 2-dimension phased array antenna is already shown in Figure 3.2. To develop this proposed 2D phased array antenna system, one key issue is that whether or not wavelength conversion will scramble the time delay information. To verify this, we measured the time delay before wavelength conversion and the time delay after wavelength conversion. The measurement results are shown in Fig. 7.10. From the measure results shown in Fig. 7.10, we could see that time delay will be increased by  $\sim 2\text{ps}$  after wavelength conversion for each individual element, which is due to the dispersive nature of SOA. However, the relative time delay is still kept unchanged. So from this measurement, it is safe to use wavelength conversion for true-time delay based phased array antenna system.

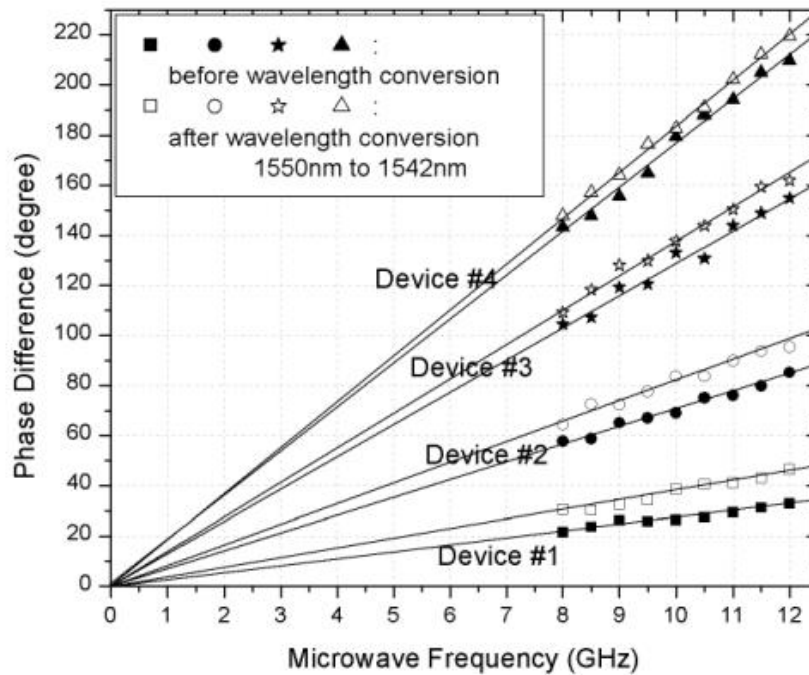


Fig. 7.10 Time delay measurements before and after wavelength conversion

Then we developed a real 4x4 2D X-band phased array antenna system based on holographic-grating true-time delay devices. We measured the radiation pattern of this system and the measurement results are shown in Fig. 11(a), (b). In measuring Fig. 7.11(a), we used a different set of time delay devices. Time delay is larger than what we discussed in the chapter 4. The parameters are listed in the following: the thinnest device is 1mm and the thickness difference is 2mm. The diffraction angle is still  $80^{\circ}$ . The devices use retro-reflection structure which can double the time delay than that from the device structure discussed in chapter 4.

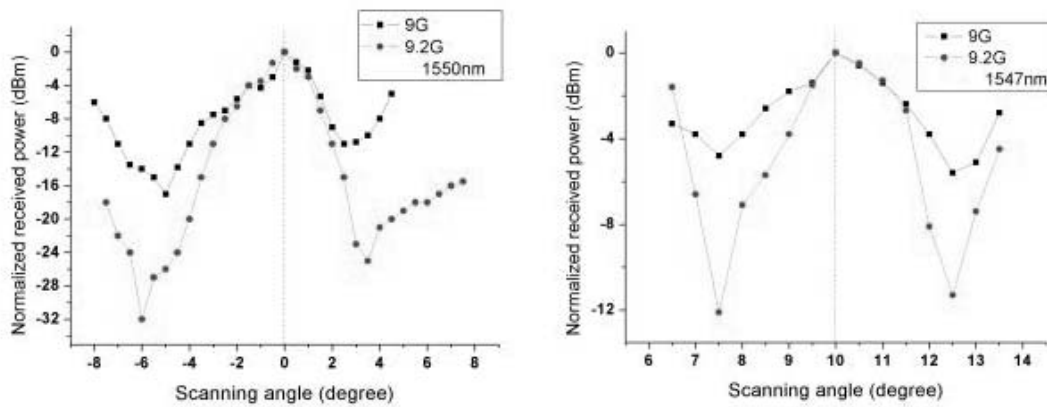


Fig. 7.11(a) Radiation pattern in the horizontal direction

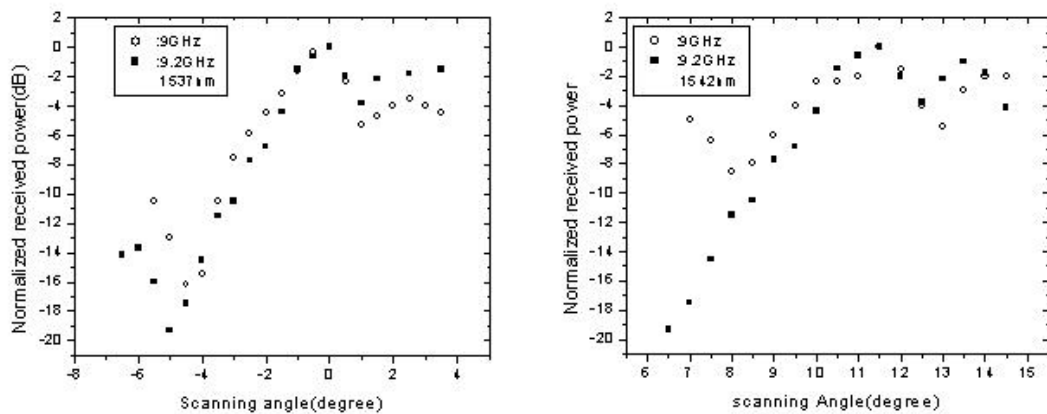
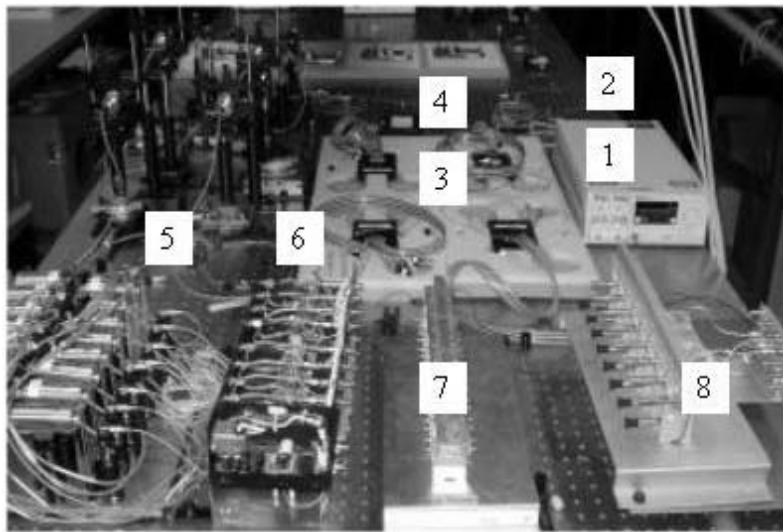


Fig. 7.11(b) Radiation pattern in the vertical direction

From the measurements in Fig. 7.11(a), wavelength is tuned from 1550nm to 1547nm which corresponds a beam scanning angle from  $0^{\circ}$  to  $10^{\circ}$ . In Fig. 7.11(b), wavelength is tuned from 1537nm to 1542nm which corresponds a beam scanning angle from  $0^{\circ}$  to  $11.7^{\circ}$ . Figure 7.12 is a photo of developed 2-dimension X-band phased array antenna system.



- |              |                  |
|--------------|------------------|
| 1: Laser     | 5: TTD           |
| 2: Modulator | 6: Photodetector |
| 3: EDFA      | 7: Amplifier     |
| 4: SOA       | 8: Antenna       |

Figure 7.12 Photo of the developed 4x4 2D X-band phased array antenna system

## 7.2 Summary

In this chapter we presented performance of the developed 4-element linear phased array antenna system. The radiation patterns of the systems were measured and show the negligible beam squint effect.

## Chapter 8

### Summary

In this research project, three major contributions were made:

1): proposed and developed continuous tunable holographic-grating based optical true-time delay devices. A dispersion-enhanced holographic-grating structure was developed to get continuous tunable time delay from the devices.

2): developed and demonstrated a 4-element linear X-band phased array antenna system using fabricated true-time delay devices. The radiation patterns at different wavelength and different frequencies were measured. The measurement results verified the beam steering angle of the phased array antenna system was steered by the optical wavelength. Furthermore, beam squint phenomenon was not observed in the measurements.

3): developed and demonstrated a 4x4 X-band phased array antenna system in combination of wavelength conversion for the first time. Wavelength conversion is based on cross-gain modulation in semiconductor optical amplifiers. The radiation patterns at the horizontal and vertical directions were measured at different wavelengths and different microwave frequencies. Again, measurement showed the beam steering angle was steered by the optical wavelength, and beam squint was not observed in the measurements.

## References

### Chapter 2

- 1: W. Ng, A. A. Walston, G. L. Tangonan, J. J. Lee, I. L. Newberg, and N. Bernstein, The first demonstration of an optically steered microwave phased array antenna using true-time-delay, *IEEE Journal of Lightwave Technology*, 9, 1124, 1991.
- 2: D. Dolfi, J. P. Huignard, and M. Baril, Optically controlled true-time delays for phased array antenna, *SPIE*, 1102, 152, 1989.
- 3: D. Dolfi, F. Michel-Gabriel, S. Bann, and J. P. Huignard, Two-dimensional optical architecture for time-delay beam forming in a phased-array antenna, *Optics Letters*, 16, 255, 1991.
- 4: D. Dolfi, P. Joffre, J. Antoine, J.-P. Huignard, D. Philippet, and P. Granger, Experimental demonstration of a phased-array antenna optically controlled with phased and time delays, *Applied Optics*, 35, 5293, 1996.
- 5: N. A. Riza, Transmit/receive time-delay beam-forming optical architecture for phased-array antennas, *Applied Optics*, 30, 4594, 1991.
- 6: N. A. Riza, Liquid crystal-based optical time delay control system for wideband phased arrays, *SPIE*, 1790, 171, 1992.
- 7: A. M. Levine, Use of fiber optic frequency and phase determining element in radar, *Proceedings of the 33<sup>rd</sup> Annual Symposium on Frequency Control*, IEEE, 436, 1979.
- 8: P. M. Freitag and S. R. Forrest, A coherent optically controlled phased array antenna system, *IEEE Microwave and Guide Wave Letters*, 3, 292, 1993.

- 9:L. Xu, R. Taylor, and S. R. Forrest, True-time delay phased array antenna feed system based on optical heterodyne techniques, *IEEE Photonics Technology Letters*, 8, 160, 1996.
- 10:D. K. T. Tong and M. C. Wu, A novel multiwavelength optically controlled phased array antenna with a programmable dispersion matrix, *IEEE Photonics Technology Letters*, 8, 812, 1996.
- 11:P. Goutzoulis and D. K. Davies, Hardware-compressive 2-D fiber-optic delay line architecture for time steering of phased-array antennas, *Applied Optics*, 29, 5353, 1990.
- 12:P. Goutzoulis and D. K. Davies, All-optical hardware-compressive wavelength multiplexed fiber optic architecture for true-time delay steering of 2-D phased array antenna, *SPIE*, 1703, 604, 1992.
- 13:P. Goutzoulis, D. K. Davies, J. Zomp, P. Hrycak, and A. Johnson, Development and field demonstration of a hardware-compressive fiber-optic true-time delay steering system for phased array antennas, *Applied Optics*, 33, 8173, 1994.
- 14:Z. Fu and R. T. Chen, High packing density optical true-time delay lines for phased array antenna applications, *Recent Research Developments Series*, 1, Dec. 1998.
- 15:Y. H. Chen, R. T. Chen, A fully packaged true time delay modules for a K-band phased array antenna demonstration, *IEEE Photonics Technology Letter*, 14, 1175, 2002.
- 16:S. Yegnanarayanan, P. D. Trinh, and B. Jalali, Recirculating photonic filter: a wavelength-selective time delay for phased array antennas and wavelength code division multiple access, *Optics Letter*, 21, 10, 1996.
- 17:W. D. Jemison and P. R. Herczfeld, Acousto-optically controlled true-time delay, *IEEE Microwave and Guided Wave Letters*, 3, 72, 1993.

- 18:L. H. Gesell, R. E. Feinleib, J. L. Lafuse, and T. M. Turpin, Acousto-optic control of time delays for array beam steering, SPIE, 2155, 194, 1994.
- 19:E. N. Toughlian and H. Zmuda, A photonic variable RF delay line for phased array antennas, Journal of Lightwave Technology, 8, 1824, 1990.
- 20:E. H. Monsay, K. C. Baldwin, and M. J. Caucuitto, Photonic true time delay for high-frequency phased array systems, IEEE Photonics Technology Letters, 6, 118, 1994.
- 21:R. A. Soref, Optical dispersion technique for time-delay beam steering, Applied Optics, 31, 7395, 1992.
- 22:S. T. Johns, D. A. Norton, C. W. Keefer, R. Erdmann, and R. A. Soref, Variable time delay of microwave signals using high dispersion fibre, Electronics Letters, 29, 555, 1993.
- 23:R. D. Esman, M. Y. Frankel, J. L. Dexter, L. Goldberg, M. G. Parent, D. Stilwell, and D. G. Cooper, Fiber-optic prism true time-delay antenna feed, IEEE Photonics Technology Letters, 5, 1347, 1993.
- 24:J. Broeng, D. Mogilevstev, S. E. Barkou, and A. Bjarklev, Photonic crystal fibers: a new class of optical waveguides, Opt. Fiber Technol., 5, 305, 1999.
- 25:T. A. Birks, D. Mogilevtsev, J. C. Knight, and P. S. J. Russell, Dispersion compensation using single material fibers, IEEE Photonics Technology Letter, 11, 674, 1999.
- 26:T. D. Engeness, M. Ibanescu, S. G. Johnson, O. Weisberg, M. Skorobogatiy, S. Jacobs, and Y. Fink, "Dispersion tailoring and compensation by modal interactions in OmniGuide fibers," Opt. Express 11 (10), 1175-1198, 2003.

27:J. D. Joannopoulos, R. D. Meade, and J. N. Winn, Photonic crystal: modeling the flow of light, Princeton, NJ: Princeton Univ. Press, 1995.

28:J. L. Cruz, B. Ortega, M. V. Andres, B. Gimeno, D. Pastor, J. Capmany, and L. Dong, Chirped fiber gratings for phased array antenna, Electronics Letters, 33, 545, 1997.

29:J. L. Corral, J. Marti, S. Regidor, J. M. Fuster, R. Laming, and M. J. Cole, Continuously variable true time-delay optical feeder for phased-array antenna employing chirped fiber gratings, IEEE Trans. Microwave and Tech., 45, 1531, 1997.

### Chapter 3

1:G. Kim, X. Han, R. Chen, A method for rebroadcasting signals in an optical backplane bus system, IEEE Journal of Lightwave Technology, 19, 959, 2001.

2:Y. Chen and R. Chen, A fully packaged true time delay module for a K-band phased array antenna system demonstration, IEEE Photonics Technology Letter, 14, 1175, 2002.

3:Z. Fu, C. Zhou, R. Chen, Waveguide-hologram-based wavelength-multiplexed pseudoanalog true-time-delay module for wideband phased-array antenna, Applied Optics, 38, 3053, 1999.

4:Z. Shi, Y. Jiang, H. Brie, F. Zhao, Y. Chen, R. Chen, Continuously delay-time tunable-waveguide hologram module for X-band phased array antenna, IEEE Photonics Technology Letter, 15, 972, 2003.

5:Brookner, Practical phased array antenna systems, Artech House, Boston, 1991.

6: W. S. C. Chang, RF photonic technology in optical fiber links, Cambridge University Press, 2002.

## Chapter 4

1:M. G. Moharam and T. K. Gaylord, Rigorous coupled-wave analysis of planar-grating diffraction, *Journal of the Optical Society of America*, 71, 811, 1981.

2:H. Kogelnik, Coupled wave theory for thick hologram gratings, *Bell Syst. Tech. J.*, 48, 2909, 1969.

3:Yevick and L. Thlen, Analysis of gratings by the beam-propagation method, *Journal of the Optical Society of America*, 72, 1084, 1982.

4:R. Petit, ed., *Electromagnetic theory of gratings*, Springer-Verlag, Berlin, 1980.

5:M. G. Moharam and T. K. Gaylord, Diffraction analysis of dielectric surface-relief gratings, *Journal of the Optical Society of America*, 72, 1385, 1982.

6:T. Tamir, H. C. Wang, and A. A. Oliner, Wave propagation in sinusoidally stratified dielectric media, *IEEE Transactions on Microwave Theory and Techniques*, 12, 323, 1964.

7:B. Lichtenberg and N. C. Gallagher, Numerical modeling of diffractive devices using the finite element method, *Optical Engineering*, 33, 3518, 1994.

8:M. G. Moharam and T. K. Gaylord, Rigorous coupled-wave analysis of grating diffraction E-mode polarization and losses, *Journal of the Optical Society of America*, 73, 451, 1983.

9:J. Goodman, *Introduction of Fourier Optics*, Second Edition, McGraw-Hill, Inc., New York, NY (1996).

10:J. Liu, Z. Fu, and R. T. Chen, Polarization sensitivity of photopolymer-based volume holograms for one-to-many surface normal optical interconnects, *Optical Engineering*, 37, 660, 1998.

11:C. Zhou, Z. Fu, M. Dobinovsky, J. I and R. T. Chen, Dispersion enhanced wavelength division multiplexing, SPIE, 3005, 144, 1997.

12:Gicherl Kim, Xuliang Han, and Ray T. Chen, "A method for rebroadcasting signals in an optical backplane bus system," IEEE Journal of Lightwave Technology, vol. 19, no. 7, pp. 959-965, July 2001.

13:A. M. Weber, W. K. Smothers, T. J. Trout, and D. J. Mickish, Hologram recording in DuPont's new photopolymer materials, SPIE, 1212, 14, 1990.

14:W. J. Gambogi, W. A. Gerstadt, S. R. Mackara, and A. M. Weber, Holographic transmission elements using improved photopolymer films, SPIE, 1555, 256, 1991.

15:R. T. Chen, S. Tang, M. M. Li, D. Gerald, and S. Natarajan, 1-to-12 surface normal three-dimensional optical interconnects, Applied Physics Letters, 63, 1883, 1993.

## Chapter 5

1:T. Durhuus, B. Mikkelsen, C. Joergensen, S. Lykke Danielsen and K. E. Stubkjaer, All optical wavelength conversion by semiconductor optical amplifiers, J. Lightwave Technol., 14, 942, 1996.

2:S. Diez, C. Schmidt, R. Ludwig, H. G. Weber, K. Obermann, S. Kindt, I. Koltchanov, and K. Pertermann, Four-wave mixing in semiconductor optical amplifiers for reuquency conversion and fast optical switching, IEEE J. Sel. Topics in Quantum Electron., 3, 1131, 1997.

3:F. Kalman, L. G. Kazovsky and J. W. Goodman, Space division switches based on semiconductor optical amplifiers, IEEE Photon. Technol. Lett., 4, 1048, 1992.

- 4:A. Ehrhardt, M. Eiselt, G. Grossopf, L. Kuller, R. Ludwig, W. Pieper, R. Schnabel, and H. G. Weber, Semiconductor optical amplifiers as optical switching gate, *J. Lightwave Technol.*, 11, 1287, 1993.
- 5:K. Vahala, R. Paiella and G. Hunziker, Ultrafast WDM logic, *IEEE J. Sel. Top. In Quantum Electron.*, 3, 698, 1997.
- 6:M. Gustavsson, A. Karlsson and L. Thylen, Travelling wave semiconductor laser amplifier detectors, *J. Lightwave Technol.*, 8, 610, 1990.
- 7:D. Zhou, K. Kang, I. Glesk, and P. R. Prucnal, An analysis of signal-to-noise ratio and design parameters of a terahertz optical asymmetric demultiplexer, *J. Lightwave Technol.*, 17, 298, 1999.
- 8:D. R. Zimmerman, L. H. Spiekman, Amplifiers for the masses: EDFA, EDWA, and SOA amplest for metro and access, *J. Lightwave Technol.*, 22, 63, 2004
- 9:M. N. Islam, Raman amplifiers for telecommunications, *IEEE J. Sel. Topics in Quantum Electron.*, 8, 548, 2002
- 10:E. U. Rafailov, P. Loza-Alvarez, W. Sibbett, G. S. Sokolovskii, D. A. Livshits, A. E. Zhukov, and V. M. Ustinov, Amplification of femtosecond pulses over by 18dB in a quantum-dot semiconductor optical amplifier, *IEEE Photonics Technol. Lett.*, 15, 1023, 2003.
- 11:P. Borri, S. Schneider, W. Langbein, U. Woggon, A. E. Zhukov, V. M. Ustinov, N. N. Ledentsov, Z. I. Alferov, D. Ouyang, and D. Bimber, Ultrafast carrier dynamics and dephasing in InAs quantum-dot amplifiers emitting near 1.3-micro-wavelength at room temperature, *Appl. Phys. Lett.*, 79, 2633, 2001.
- 12:From the JDSU SOA catalog which can be downloaded from [www.jdsu.com](http://www.jdsu.com)

- 13: M. Magari, M. Okamoto, and Y. Noguchi, 1.55μm polarization-insensitive high-gain tensile-strained-barrier MQW optical amplifier, *IEEE Photonic Technol. Lett.*, 3, 998, 1991.
- 14: M. Joma, H. Horikawa, C. Q. Xu, K. Yamada, Y. Katoh, and T. Kamijoh, Polarization insensitive semiconductor optical amplifiers with tensile strained InGaAsP/InGaAsP multiple quantum well structure, *Appl. Phys. Lett.*, 62, 121, 1993.
- 15: A. Godefroy, Al Le Corre, F. Clerot, S. Salaun, S. Loualiche, J. C. Simon, L. Henry, C. Vaudry, J. c. Keromnes, G. Joulie, and P. Lamouler, 1.55μm polarization-insensitive optical amplifier with strain-balanced superlattice active layer, *IEEE photonic Technol. Lett.*, 7, 473, 1995.
- 16: L. Gillner, E. Goobar, L. Thylen, and M. Gustavsson, Semiconductor laser amplifier optimization: an analytical and experimental study, *IEEE J. of Quantum Electron.*, 25, 1822, 1989.
- 17: M. J. Connelly, Wideband semiconductor optical amplifier steady-state numerical model, *IEEE J. of Quantum Electron.*, 37, 439, 2001.
- 18: I. D. Henning, M. J. Adams, and J. V. Collins, Performance predictions from a new optical amplifier model, *IEEE J. of Quantum Electron.*, 21, 609, 1985.
- 19: J. Wang, H. Olesen, and K. E. Stubkjaer, Recombination, gain and bandwidth characteristics of 1.3μm semiconductor laser amplifiers, *J. of lightwave Technol.*, 5, 184, 1987.
- 20: M. J. Adams, J. V. Collins, and I. D. Henning, Analysis of semiconductor laser optical amplifiers, *IEE Proceedings*, 132, 58, 1985.

## Chapter 6

- 1: S. Okamoto and K. Sato, Optical path cross-connect systems for photonic transport networks, Proc. IEEE Global Telecommun. Conf., Nov. 474, 1993.
- 2: F. Derr, M. N. Huber, G. Kettler, and N. Thorweihe, Key issues of an optical FDM transport network, Proc. OFC'95, San Diego, CA, Feb., 1995.
- 3: C. A. Brackett, A. S. Acampora, J. Schweitzer, G. Tangonan, M. T. Smith, W. Lennon, K. C. Wang, R. H. Hobbs, Ascalable multiwavelength multihop optical network: A proposal for research on all-optical networks, J. Lightwave technol., 11,736, 1993.
- 4: N. Wauters and P. Demester, Wavelength requirements and survivability in WDM cross-connected networks, Proc. ECOC'94, 2, 589, 1994.
- 5:K. Sato, Transport network evolution with optical paths, Proc. ECOC'94, 2, 919, 1994.
- 6:K. Sato, S. Okamoto, and H. Hadama, Network performance and integrity enhancement with optical path layer technologies, J. Select. Areas Commun., 12, 159, 1994.
- 7:T. Durhuus, B. Fernier, P. Garabedian, F. Leblond, J. L. Lafrayette, B. Mikkelsen, C. G. Joergensen, and K. E. Stubkjaer, High speed all-optical gating using two-section semiconductor optical amplifier structure, CLEO'92, 1992.
- 8:T. Durhuus, C. Joergensen, B. Mikkelsen, R. J. S. Pedersen, and K. E. Stubkjaer, All optical wavelength conversion by SOA's in a Mach-Zehnder configuration, IEEE Photonics Technol. Lett., 6, 53, 1994.
- 9:M. C. Tatham, 20nm optical wavelength conversion using nondegenerate four wave mixing, IEEE Photonics Technol. Lett., 5, 1303,1993.
- 10:K. Inoue, Polarization insensitive wavelength conversion using fiber four wave mixing with two orthogonal pumps at different frequencies, OFC'94, 1994.

- 11:Y. Suzuki and H. Toba, Recent research and development of all optical wavelength conversion devices, 1, 1, 2003.
- 12:K. Y. Lau, A. Yariv, Intermodulation distortion in a directly modulated semiconductor injection laser, 45, 1034, 1984.
- 13:D. Marcenac, and A. Mecozzi, Switches and frequency converters based on cross-gain modulation in semiconductor optical amplifiers, 9, 749, 1997.
- 14:J. Capmany, E. Peral, and D. Pastor, Formular for two-carrier intermodulation distortion in wavelength converted subcarrier multiplexed signals via cross gain modulation, 12, 278, 2000.
- 15:W. S. C. Chang, RF photonic technology in optical fiber links, Cambridge University Press, 2002.
- 16:Yariv, Optoelectronics, 4nd,, Saunders College Publishing, 1991
- 17:A. J. Seeds, Optical transmission of microwaves, Rev. Radio Sci., Oxford, U. K.: Oxford University Press, 325, 1996.
- 18:A. J. Seeds, Microwave photonics, IEEE Trans. Microwave Theory and Techniques, 50, 877, 2002.

## Vita

Zhong Shi was born in Shandong Province of China on 1972, son of Shoutan Shi and Ailian Xu. He entered Shandong University in Jinan, Shandong Province, in 1990. He completed his bachelor's studies with a major of Optics in 1994 and then entered the Graduate School of Beijing University of Posts and Telecommunications in Beijing. He had been an engineer in China after receiving the master's degree in Electrical Engineering in the summer of 1997. In the fall 1999, he was admitted by graduate school of Rensselaer Polytechnic Institute. Later he transferred to the University of Texas at Austin to study in Electrical and Computer Engineering Department.

Permanent Address:           #301, Builing 23  
                                      PanJiaYuan, ChaoYang District  
                                      Beijing, China 100021  
                                      The People's Republic of China

This dissertation was typed by the author.